PE&RS

October 2022 Volume 88, Number 10

Photogrammetric Engineering & Remote Sensing

The official journal for imaging and geospatial information science and technology

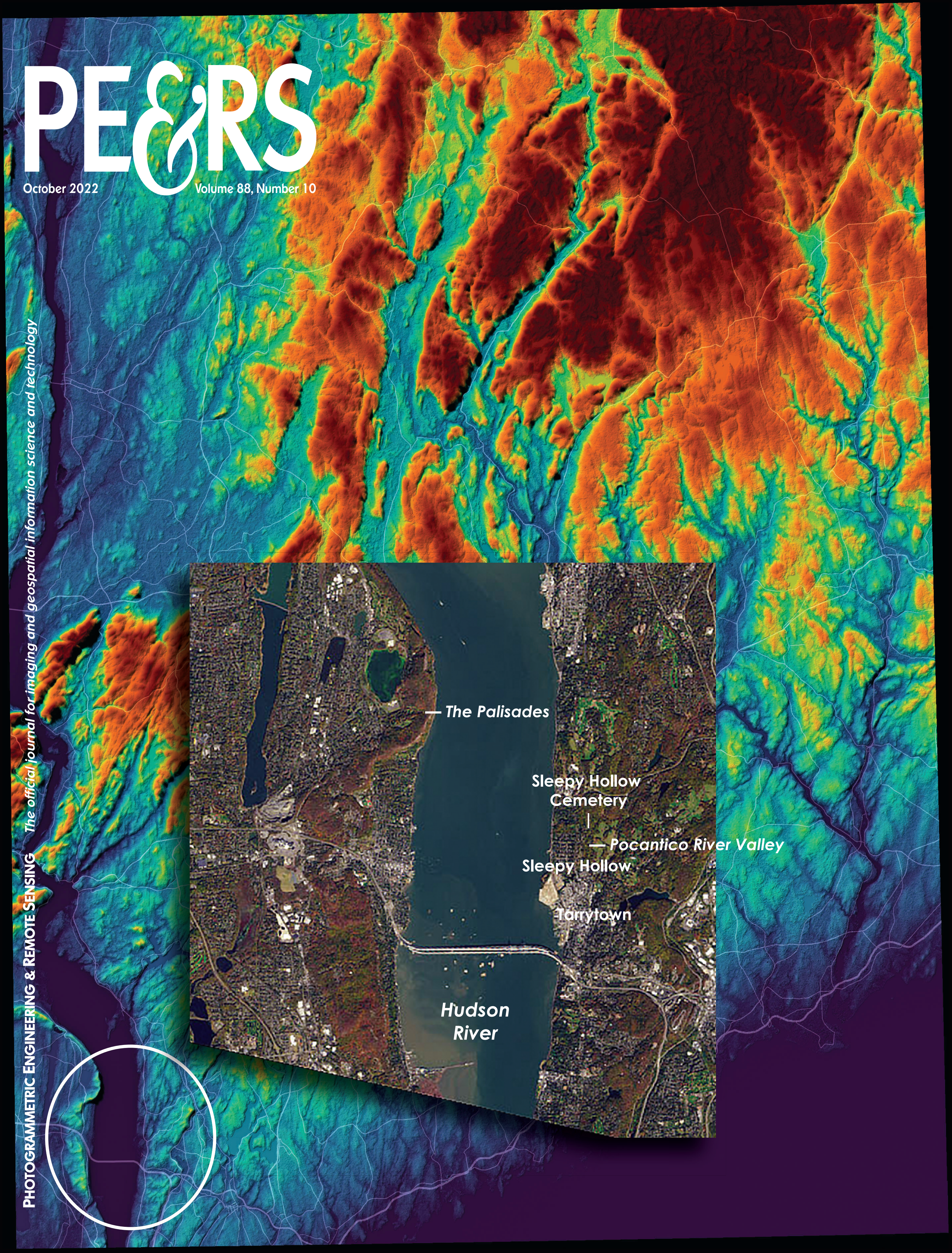

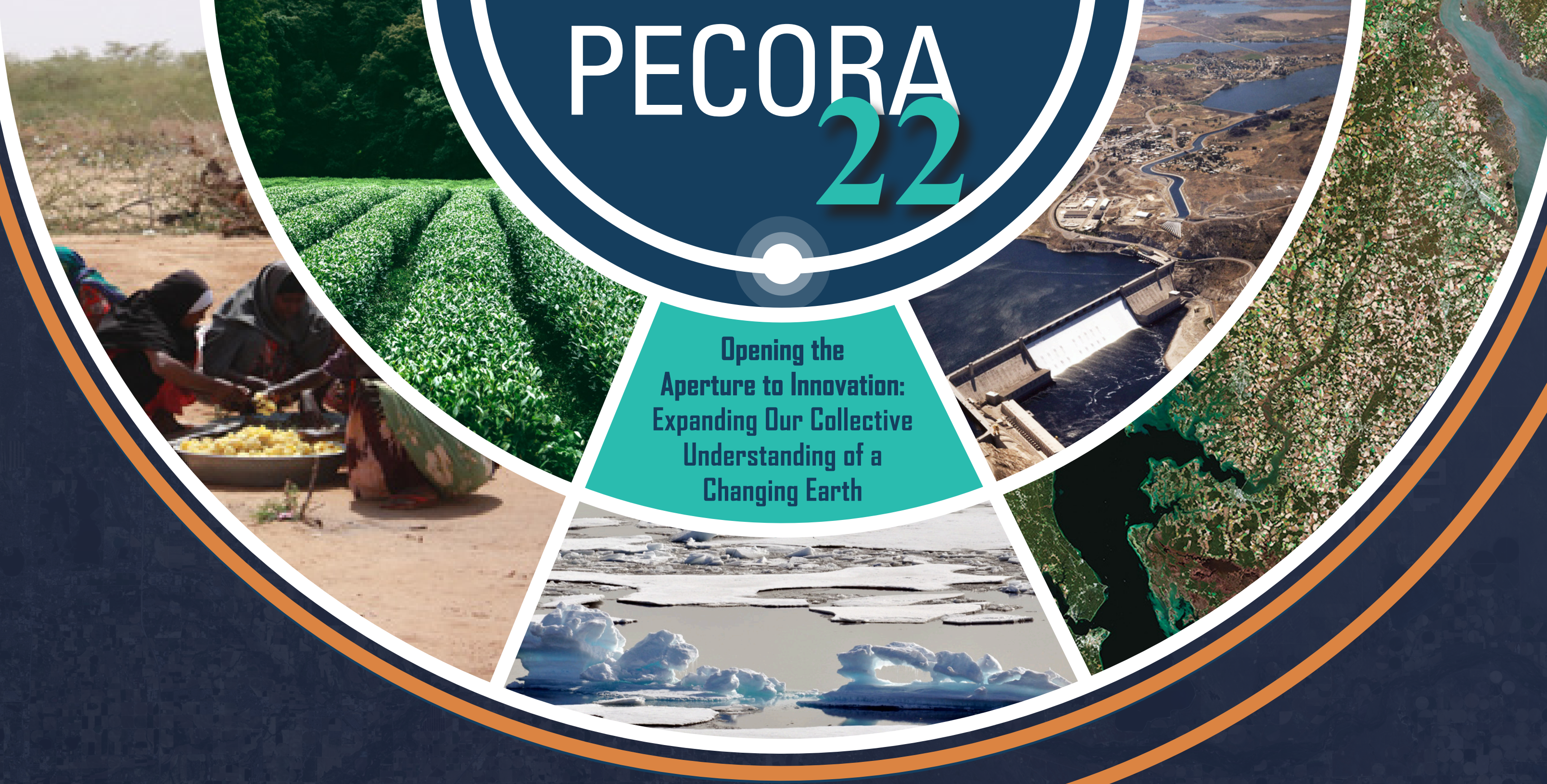

William T. Pecora Remote Sensing Symposium

OCTOBER 24 — 27, 2022 Denver, Colorado, USA

The premier symposium focusing on all aspects of Earth observations, spanning scientific discoveries to operational applications, sensors, and decisions. Pecora 22 embraces both innovation and discovery while Landsat data improves our ability to understand and better manage the resources of our Earth's surface.

Celebrating 50 YEARS Landsat 1972-2022

2022 marks the 50th anniversary of the launch of the first Landsat satellite.

Join us as we celebrate 50 years of accomplishments, innovations, and discoveries— all with an eye on the future.

For more information on the conference, program line-up, and to register, visit Pecora22.org.

ANNOUNCEMENTS

NV5 Geospatial announced the debut of its ARIS II Rover. The upgraded robotic electric substation monitoring system comes after five years of in-field implementation and testing. The rover meets the industry's most exacting standards for ruggedness and reliability, enabling it to function in harsh environmental conditions and over various terrains commonly found at distribution and transmission substations. The remotely controlled wheeled rover offers a modular design custom-fitted with advanced thermal sensors, imaging, and audio/video technology that allows utilities to protect assets and limit liability while speeding reaction time.

"Geographic and personnel limitations, combined with aging infrastructure, present significant challenges for utility companies when it comes to maintaining their substations," said Ian Birdie, vice president of Innovation for NV5 Geospatial. "With our extensive experience in these substation environments, NV5 Geospatial has customized the ARIS II Rover for the unique needs of utilities. We built our next-generation robot on a rugged platform that can exist remotely and deliver the information and insights utilities need to maintain their networks proactively. On-time information allows quick response to equipment anomalies, weather events, and intrusions before they have an impact."

The ARIS II rover supports a variety of applications, including event check-ups, situational awareness, health monitoring, work audits, inventory management, emergency response and security, offering:

- Industry-leading military standards (MIL-STD) and ingress protection ratings, resulting in a weatherproof design that can withstand and work reliably in harsh environments, and 36-degree climbing ability for difficult terrain.
- Pre-configured payload of sensors and equipment that supports thermal imaging, video and two-way audio communication capabilities, as well as GPS with real-time kinematics (RTK) that supports accurate mapping of drives within a substation.
- Modular design for flexibility in sensor and camera positioning and simplified maintenance on or off site, with the ability to carry up to 110 outs of equipment.
- Up to six hours of battery life or two miles of driving and a recharge garage included when the rover is not in use.
- Easy installation and movement to different substation locations with a pallet-ready Rover and housing.
- Secure web portal that offers controls and management tools to support real-time inspection/driving, feedback and measurement from onboard sensors, and the ability to review and measure thermal conditions and high-resolution photos.

This combination of features enables the ARIS II Rover to assess conditions in substations. Thermal imaging captures temperature deltas against assets to help utilities determine when equipment needs to be evaluated and replaced. Onboard cameras can visually detect corrosion and asset damage, and are able to read gauges from up to 50 feet away.

To learn more about the ARIS II Rover or to schedule a demonstration, contact NV5G-Sales@nv5.com.

Trimble announced today its commitment to reduce greenhouse gas emissions in line with the ambitious goals of the Paris Agreement and a net-zero future to keep global temperature increase to 1.5°C. Trimble received approval of its emissions reduction targets by the Science Based Targets initiative (SBTi), a coalition of the CDP, the United Nations Global Compact, World Resources Institute and the World Wide Fund for Nature, joining a growing number of companies taking urgent action on climate change.

"Taking decisive climate action is essential to protect our planet and communities for future generations. It also demonstrates Trimble's commitment to our purpose—to transform the way the world works as well as transform the way "we" work," said Rob Painter, president and CEO, Trimble.

"For decades, Trimble solutions have contributed to reducing greenhouse gas emissions and combating climate change," continued Painter. "The nature of Trimble's technologies, which connect the physical and digital worlds, provides efficiencies and promotes sustainability in our end markets such as construction, agriculture, forestry, utilities and transportation. Our leadership team is committed to further reducing our carbon footprint as well as continuing to develop solutions that enable our customers to reduce their climate impacts—it is an important lever in our Connect and Scale strategy. Trimble is dedicated to do its part to help protect and build a better world."

Trimble's science-based targets accelerate decarbonization across its value chain, and include the following commitments:

- Reduce absolute scope 1 and 2 greenhouse gas emissions 50 percent by 2030 from a 2019 base year
- Achieve 100 percent annual sourcing of renewable electricity by 2025
- Reduce absolute scope 3 greenhouse gas emissions from fuel and energy related activities, business travel and upstream transportation and distribution 50 percent by 2030 from a 2019 base year
- Commit to partner with 70 percent of its suppliers by emissions covering purchased goods and services and capital goods to set science-based targets by 2026.

This decade is considered the decisive decade for climate change. As part of answering this urgent call to action, Trimble has joined forces with other companies and climate leaders in the Business Ambition for 1.5°C campaign, the We Mean Business Coalition and the Race to Zero Campaign.

"Setting ambitious yet achievable climate targets are part of our commitment to reducing Trimble's carbon footprint," said Leah Lambertson, senior vice president and head of Sustainability, Trimble. "Embedding our climate action goals into Trimble's operational choices will help ensure that our decision making and growth plans are consistent with our low-carbon vision. Today's commitments are important steps in our journey to delivering growth in a responsible and sustainable way to achieve a net-zero future."

Trimble also announced the release of its 2021 Sustainability Report. Built around the company's mission of transforming the way the world works, the report features how Trimble is helping to create a better future for our planet and the communities we serve.

The report summarizes its initiatives and performance across Environmental, Social and Governance (ESG) topics, highlighting the company's sustainability approach; end-user industry solutions; community philanthropy through its Trimble Foundation Fund; employee engagement and development as well as Diversity, Equity and Inclusion (DEI) initiatives; and governance.

URISA is pleased to announce the results of its 2022 URISA Board of Directors' election. Tom Fisher will serve in the position of President-Elect and Josiah Burkett, Bernadette deLeon, and Matt Gerike will serve as Directors. They will all begin their three-year terms at the conclusion of GIS-Pro 2022 in Boise.

Tom will serve as President-Elect for one year and his term as President will begin at the conclusion of GIS-Pro 2023.

"This is a great honor to lead the URISA organization and to represent the members for three more years through the Presidential track. URISA has accomplished a lot over the past sixty years with steady leadership and member volunteerism. I plan to continue the tradition of excellence set by the trailblazers before me and leave a legacy of servant leadership for upcoming geospatial professionals to aspire to. Thank you again for your confidence and trust to lead URISA. I look forward to seeing everyone in Boise, Idaho this fall and, in the chapters, and committees of this amazing URISA organization."

Newly-elected URISA Directors include:

- Josiah Burkett, Geographic Information Systems Analyst /Geospatial Team Lead, GeoTechVision, Kingston, Jamaica
- Bernadette de Leon, GISP, Director of School of Public Health Bloomington IT Services
  Indiana University, Bloomington, Indiana
- Matthew J. Gerike, PhD, GISP, Geospatial Program Manager, Virginia Geographic Information Network (VGIN), Virginia Department of Emergency Management (VDEM), Richmond, Virginia

Ashley Hitt was elected by the membership as President-Elect last year and will begin her term as President of URISA at the conclusion of GIS-Pro 2022. Brent Jones will become Immediate Past-President at that time.

At the close of GIS-Pro 2022, the terms of service for these URISA Board members will conclude and we thank them all, in advance, for their amazing dedication and service to URISA:

- Immediate Past President—Kevin Mickey, GISP, The Polis Center-IUPUI, Indianapolis, Indiana
- Board Secretary—Susan Kamei, USC Spatial Sciences Institute - Los Angeles, California
- Tom Fisher, GISP, AICP, Cuyahoga County - Cleveland, Ohio
- John Nolte, GISP, Denver Water - Denver, Colorado

CALENDAR

- 23-27 October, **Pecora 22**, Denver, Colorado. For more information, visit https://pecora22.org/.
- 31 October - 4 November, **URISA GIS Leadership Academy,** Santa Rosa, California. For more information, visit www.urisa.org/education-events/urisa-gis-leadership-academy/.
- 2-4 November, **AutoCarto 2022— Ethics in Mapping: Integrity, Inclusion, and Empathy**, Redlands, California. For more information, visit https://cartogis.org/autocarto/autocarto-2022/.

PE&RS

PHOTOGRAMMETRIC ENGINEERING & REMOTE SENSING

The official journal for imaging and geospatial information science and technology

October 2022 Volume 88 Number 10

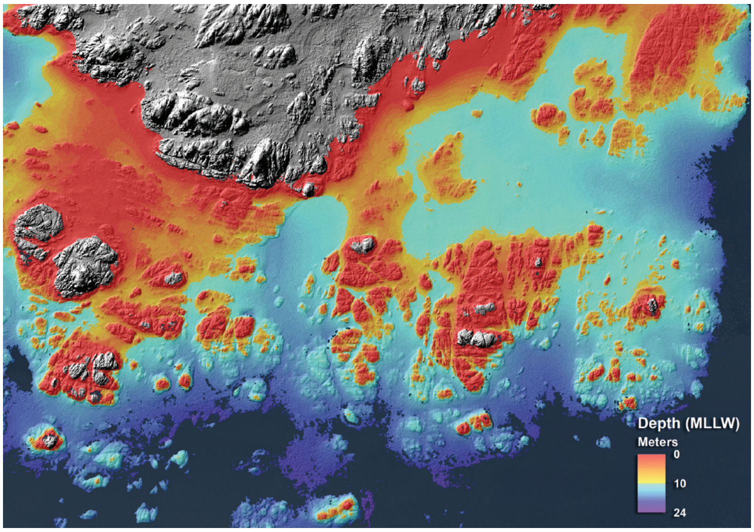

COLUMNS

ANNOUNCEMENTS

DEPARTMENTS

See the Cover Description on Page 616

COVER DESCRIPTION

In 1798, with a yellow fever epidemic raging in New York City, fifteen-year-old Washington Irving was sent north to stay with a family friend in the lower Hudson River Valley in the hope that fresh air and open space would help him elude the deadly virus. He ended up in Tarrytown, a small town about 25 miles (40 kilometers) north of Manhattan on the eastern side of the river.

Irving delighted in exploring the verdant, rocky landscapes north of Tarrytown, particularly an area later named Sleepy Hollow. He found the forests and streams there to be perfect for wandering, daydreaming, and fishing. He later settled there, and many of the landscapes he had explored as a teen became nostalgic backdrops for his short stories.

One of his most famous—The Legend of Sleepy Hollow—is set in the area highlighted in the cover image. The image is composed from elevation data from the Shuttle Radar Topography Mission (SRTM). It is false-color to emphasize the topography; red areas are the highest elevations, and blue areas are closer to sea level. The Operational Land Imager (OLI) on Landsat 8 acquired a natural-color image (below) of the same area on October 27, 2017.

Much of the rock beneath this landscape is Fordham gneiss, an ancient bedrock that formed more than one billion years ago under the intense heat and pressure of colliding land masses. The smashing and suturing of continents that produced a supercontinent called Rodinia was followed by countless cycles of erosion, mountain building, and the ebb and flow of ice ages. Over time, these and other geologic processes formed the worn, hilly landscapes that are found today around Sleepy Hollow.

According to Irving's tale, the forests and swamps of this uneven, corrugated terrain are where a headless horseman—perhaps a Hessian soldier killed during the Revolutionary War—is said to roam at night looking for his missing head. The Sleepy Hollow Cemetery and Old Dutch Church, landmarks that feature prominently in the story, sit on a small ridge near the center of the image.

The Pocantico River, what Irving calls that "wizard stream," flows through a valley that appears as a dark, thin line in the elevation map. In the story's climax, the Headless Horseman chases the protagonist across a wooden bridge over the river. To the east, in the Pocantico Hills, lies Raven Rock, a large glacial erratic transported and deposited by melting ice in a glen haunted by the ghost of a woman who perished there. The cliff on the western side of the river, part of the Palisades, formed roughly 200 million years ago when a sheet of rising magma was trapped between layers of sedimentary rock as a different supercontinent was breaking apart.

Irving died and was buried in the Sleepy Hollow Cemetery in 1859, but his words about Sleepy Hollow live on. They still resonate, especially on Halloween, when the town celebrates its literary history with a festival each year. "The place still continues under the sway of some witching power, that holds a spell over the minds of the good people, causing them to walk in a continual reverie," Irving wrote in the opening of The Legend of Sleepy Hollow. "The whole neighborhood abounds with local tales, haunted spots, and twilight superstitions; stars shoot and meteors glare oftener across the valley than in any other part of the country, and the nightmare, with her whole ninefold, seems to make it the favorite scene of her gambols."

Visit, https://landsat.visibleearth.nasa.gov/view.php?id=149022 to see both images in full size.

NASA Earth Observatory images by Joshua Stevens. using topographic data from the Shuttle Radar Topography Mission (SRTM) and Landsat data from the U.S. Geological Survey. Story by Adam Voiland.

asprs
THE IMAGING & GEOSPATIAL INFORMATION SOCIETY

PHOTOGRAMMETRIC ENGINEERING & REMOTE SENSING

Journal Staff

Publisher ASPRS
Editor-In-Chief Alper Yilmaz
Director of Publications Rae Kelley
Electronic Publications Manager/Graphic Artist Matthew Austin

Photogrammetric Engineering & Remote Sensing is the official journal of the American Society for Photogrammetry and Remote Sensing. It is devoted to the exchange of ideas and information about the applications of photogrammetry, remote sensing, and geographic information systems. The technical activities of the Society are conducted through the following Technical Divisions: Geographic Information Systems, Photogrammetric Applications, Lidar, Primary Data Acquisition, Professional Practice, Remote Sensing Applications, and Unmanned Autonomous Systems Division. Additional information on the functioning of the Technical Divisions and the Society can be found in the Yearbook issue of *PE&RS*.

Correspondence relating to all business and editorial matters pertaining to this and other Society publications should be directed to the American Society for Photogrammetry and Remote Sensing, 8550 United Plaza Boulevard, Suite 1001, Baton Rouge, LA 70809, including inquiries, memberships, subscriptions, changes in address, manuscripts for publication, advertising, back issues, and publications. The telephone number of the Society Headquarters is 301-493-0290; the fax number is 225-408-4422; web address is www.asprs.org.

PE&RS. *PE&RS* (ISSN0099-1112) is published monthly by the American Society for Photogrammetry and Remote Sensing, 425 Barlow Place, Suite 210, Bethesda, Maryland 20814-2144. Periodicals postage paid at Bethesda, Maryland and at additional mailing offices.

SUBSCRIPTION. For the 2022 subscription year, ASPRS is offering two options to our *PE&RS* subscribers — an e-Subscription and the print edition. e-Subscribers can add printed copies to their subscriptions for a small additional charge. Print and Electronic subscriptions are on a calendar-year basis that runs from January through December. We recommend that customers who choose print and e-Subscription with print renew on a calendar-year basis.

The rate for a Print subscription for the USA is $1105.00 USD, for Canadian* is $1164.00 USD, and for Non-USA is $1235.00 USD.

The rate for e-Subscription (digital) Site License for the USA and Non-USA is $1040.00 USD and for Canadian* is $1089.00 USD.

The rate for e-Subscription (digital) plus Print for the USA is $1405.00 USD, for Canadian* is $1464.00 USD, and for Non-USA is $1435.00 USD.

*Note: e-Subscription, Print subscription, and e-Subscription plus Print for Canada includes 5% of the total amount for Canada's Goods and Services Tax (GST #135123065). **PLEASE NOTE: All Subscription Agencies receive a 20.00 USD discount.**

POSTMASTER. Send address changes to *PE&RS*, ASPRS Headquarters, 8550 United Plaza Boulevard, Suite 1001, Baton Rouge, LA 70809. CDN CPM #(40020812).

MEMBERSHIP. Membership is open to any person actively engaged in the practice of photogrammetry, photointerpretation, remote sensing and geographic information systems; or who by means of education or profession is interested in the application or development of these arts and sciences. Membership is for one year, with renewal based on the anniversary date of the month joined. Membership Dues include a 12-month electronic subscription to *PE&RS*. To receive a print copy of *PE&RS* there is an additional postage fee of $60.00 USD for U.S. shipping; $65.00 USD for Canadian shipping; or $75.00 USD for international shipping per year. Annual Individual Member dues for members residing in the U.S. and Other Foreign Members are $150.00 USD and $158.00 USD for Canadians. Annual Student Member dues for members residing in the U.S. are $50.00 USD; $53.00 USD for Canadian; and $60.00 USD for Other Foreign Members. A tax of 5% for Canada's Goods and Service Tax (GST #135123065) is applied to all members residing in Canada.

FEATURE

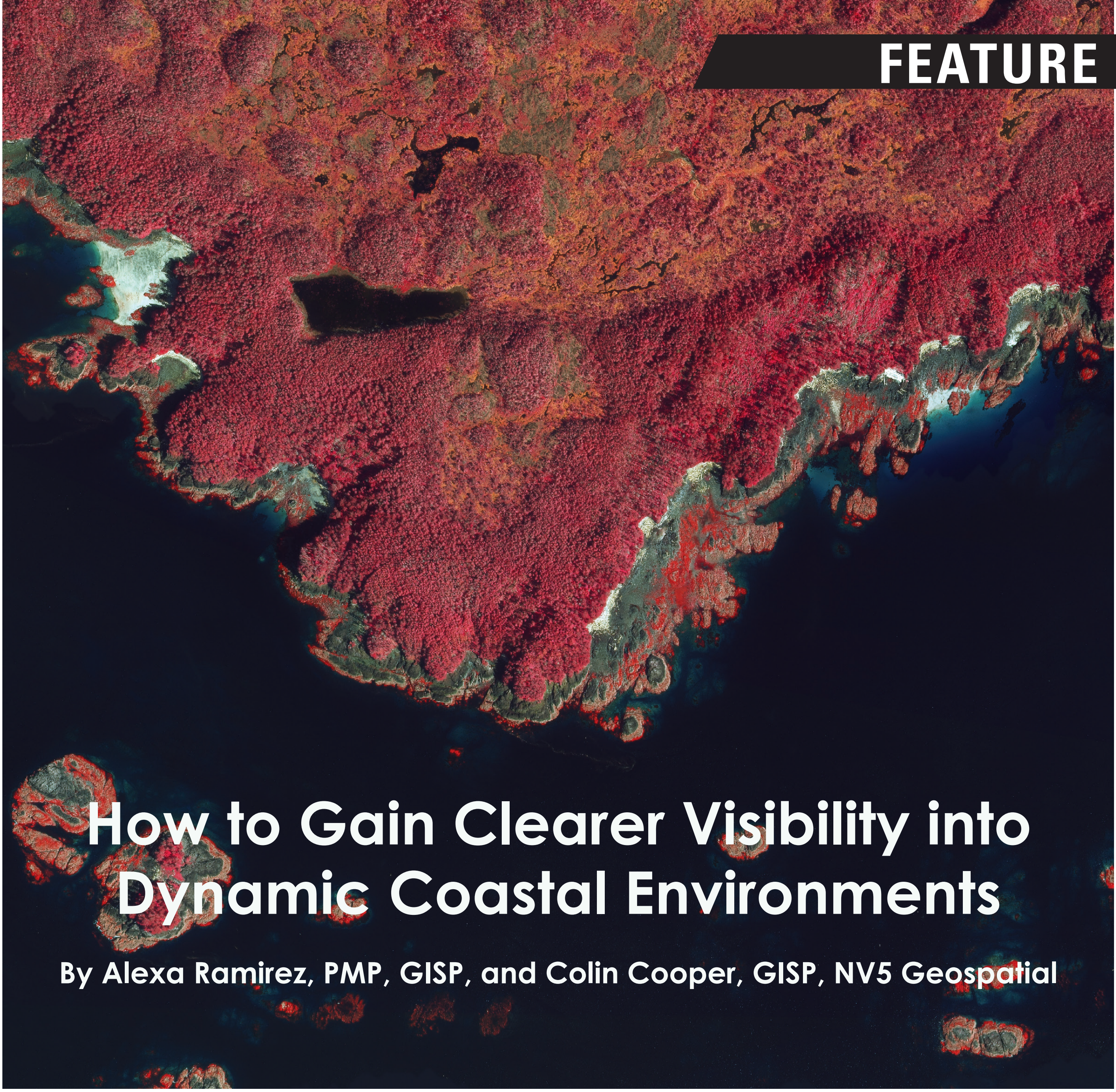

How to Gain Clearer Visibility into Dynamic Coastal Environments

By Alexa Ramirez, PMP, GISP, and Colin Cooper, GISP, NV5 Geospatial

Mapping rugged coastlines is dangerous work. Rocky shores, underwater hazards, volatile weather, and changing turbidity create perilous conditions. These conditions make it difficult to collect accurate, detailed data through conventional means, including boats equipped with sonar and ground survey instruments.

Advances in technology are changing the dynamics. Using a state-of-the-art combination of advanced remote sensing and imaging technologies, NV5 Geospatial is yielding more accurate data and delivering insights on dynamic coastal landscapes.

Figure 1 (above). Color infrared image of the southern end of Duke Island. Duke Island is part of the Alexander Archipelago in southeastern Alaska. Image is created from 4 band imagery collected with the Vexcel UltraCam Eagle M3 camera.

A History of Innovation

NV5 Geospatial is no stranger to challenging geospatial projects. Throughout our company's 90+ year history, we have been at the center of many of the nation's most interesting and demanding projects.

NV5 Geospatial and its predecessor companies documented the construction of the Golden Gate Bridge in the '30s and mapped the Colorado River in the Grand Canyon, flying more than 3000 feet below the rim in many locations. We performed the first ever comprehensive mapping of Ameri-

Photogrammetric Engineering & Remote Sensing
Vol. 88, No. 10, October 2022, pp. 617-619.
0099-1112/22/617-619

doi: 10.14358/PERS.88.10.617

can Samoa's five islands and two atolls and monitored the eruption of Kilauea in Hawaii and its impact on the local population and environment. In addition, we conducted the largest hyperspectral project on record, providing accurate locations of all ash trees in and around electric grid assets and documenting risk from the emerald ash borer.

The secret to NV5 Geospatial's success on projects of this scale is our constant innovation, seeking a diversity of cutting-edge geospatial technologies and solutions that deliver more and better data. In just the past decade, we have become well known for our expertise in ship-based bathymetric surveys and topobathymetric lidar.

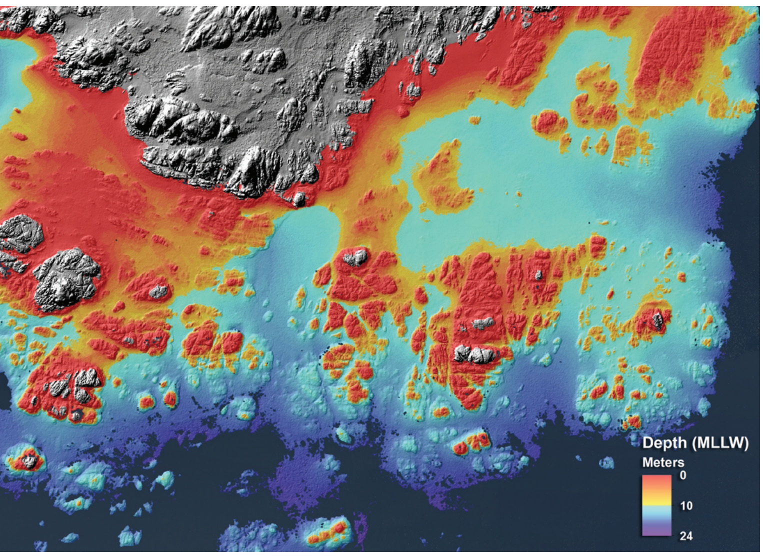

Figure 2. Hillshade model of the topobathymetric lidar generated DEM colored by depth to highlight areas shallower than 10 meters. Submerged rocks and a steeply rising coastline make this area dangerous and difficult to map with survey vessels.

Alaska Topobathymetric Project Breaks New Ground

The Alaska Coastal Mapping Strategy was spearheaded by the 2019 Presidential Memorandum on Ocean Mapping of the United States Exclusive Economic Zone and the Shoreline and Nearshore of Alaska, which brought together the National Oceanic and Atmospheric Administration (NOAA), the State of Alaska, and the Alaska Coastal Mapping Executive Committee. The long-term vision was to create seamless coastal mapping data across the state of Alaska by 2030, with short-term goals of prioritized topobathymetric lidar mapping campaigns that build a strong connection between land and sea.

NV5 Geospatial's contribution to this initiative began with mapping the coastal waters of the Revillagigedo Channel in Alaska for NOAA's National Geodetic Survey (NGS) Remote Sensing Division (RSD) Coastal Mapping Program (CMP). NOAA, and its partners at the State of Alaska and the Alaska Coastal Mapping Executive Committee, brought in NV5 Geospatial to leverage our unique array of sensors and processes. The project required planning and executing an 846-square-mile aerial acquisition, which began in June 2021, and was conducted as weather permitted. We also deployed buoys throughout the survey area to monitor water turbidity and performed limited ground surveys.

The Coastal Mapping Program requires the collection of airborne topographic/bathymetric lidar and digital camera imagery data to enable accurate and consistent measurement of the national shoreline. This supports increasing efficiency and safety of NOAA's hydrographic surveying operations and is critical for updating nautical charts, managing coastal resources, and defining U.S. territorial limits.

Conditions in and around the Revillagigedo Channel make it extremely difficult and hazardous to operate large survey vessels in nearshore areas. There is a short operational window for data collection due to environmental constraints in addition to shoals and rocky outcrops that must be avoided. This is mitigated by collecting topobathymetric lidar in the dangerous, hard-to-reach areas where the rocky shoreline meets the open water. The lidar data allows sonar vessels to stay further offshore where they can collect data safely and efficiently.

A Closer Look at the Remote Sensing Technology

NV5 Geospatial's topobathymetric program relies on multiple lidar systems. When planning projects, we take into careful consideration how sensor selection, site characteristics, survey approach, acquisition specifications and processing methodology will impact results and data quality.

In Alaska, we deployed Leica Chiroptera 4X and Hawkeye 4X topobathymetric lidar sensors for mapping submerged lands, a Riegl VQ1560ii near-infrared (NIR) topographic lidar sensor for mapping adjacent lands, and a Vexcel UltraCam Eagle M3 camera for four-band imagery acquisition - all installed in a fixed-wing aircraft. The Chiroptera/HawkEye 4x combines shallow- and deep-water laser channels that produce high-resolution and accurate data necessary for detecting submerged features. It has an integrated NIR channel for capturing seamless data at the land water interface. Southeast Alaska is characterized by mountainous terrain, fjords, and boxed canyons that can pose safety and efficiency problems for capturing the nearshore land with low altitude topobathymetric sensors. Adding the Riegl VQ1560ii supported decoupling of inland and nearshore areas, which allowed increased flight windows crucial to maximizing productivity on limited good weather days.

To support the aerial work, we needed to collect ground truthing data across the study area, which was rugged and remote. To achieve necessary coverage, we had to rely on a boat to access areas to survey. We were able to conduct real-time kinematic (RTK) GPS surveys to collect non-vegetated and vegetated vertical accuracy check points, as well as the necessary control points for both lidar and imagery processing. A boat was also used to deploy buoys equipped with Xylem EXO2 turbidity sondes to provide real-time monitoring of conditions across the area. In addition, two docks were set up with turbidity monitoring stations.

Once acquired, NV5 Geospatial calibrated and processed lidar data using commercial and proprietary software to meet the national mapping program specifications. The Leica Lidar Survey Studio was used to extract points from the bathymetric waveform data, as well as define the water surface, which it uses to correct the placement of points for refracting into the water column. Additional processing steps were used to seam-

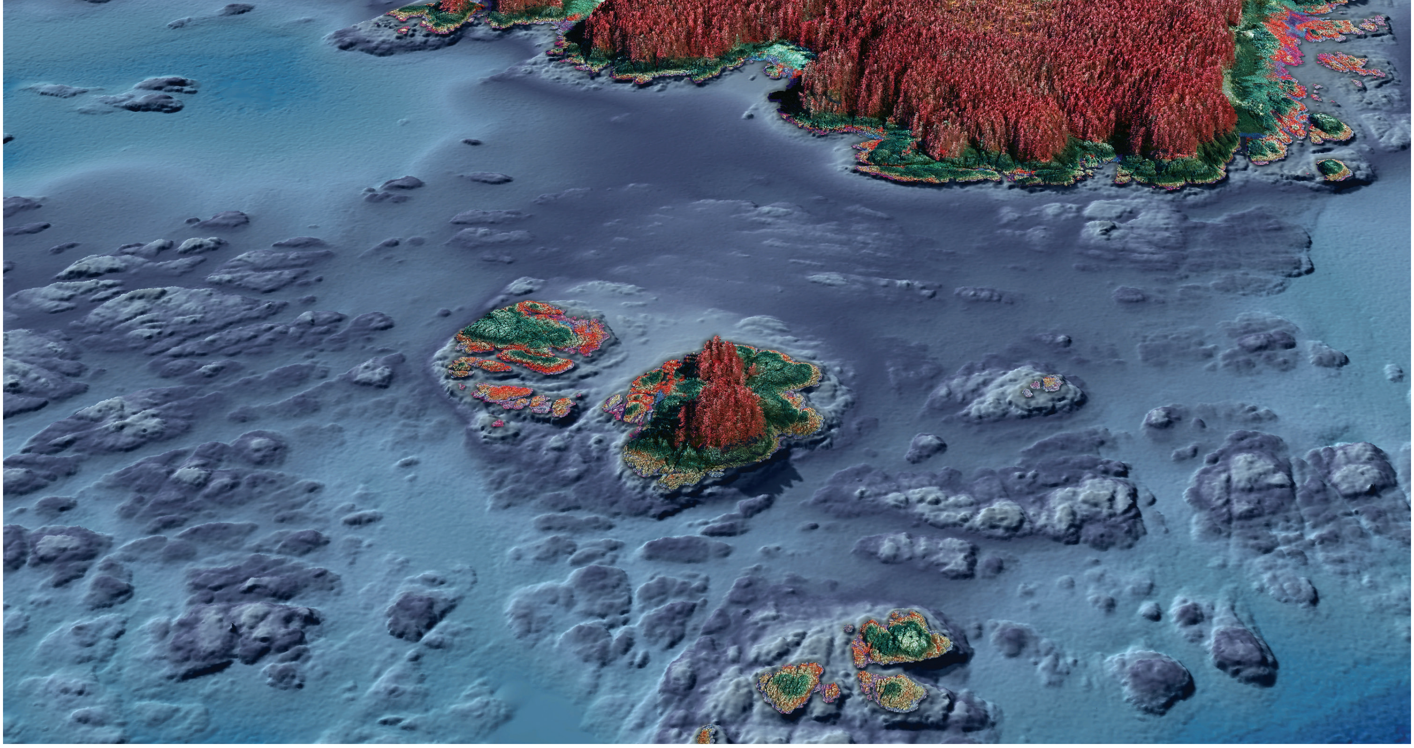

Figure 3. 3D visualization of the topobathymetric DEM colored by depth with the above ground lidar point cloud colored by color infrared imagery. The topobathymetric lidar reveals a rugged terrain under water with kelp beds that pose risk for marine traffic.

lessly combine the collected topographic data from the Riegl VQ1560ii sensor with coastal shore data collected from the Chiroptera 4x's topographic NIR channel. A detailed cutline was developed between the datasets, which favored hard permanent surfaces with no to little change, mitigating artifacts in the final developed elevation models.

The average bathymetric laser penetration throughout the study area was approximately 12 meters, with maximum depths reaching down to greater than 25 meters in clearer waters. The resulting submerged topography highlighted areas of rocky outcrops, shoals, and pervasive kelp beds.

Figure 4. GPS survey set-up to collect a hard surface check point used in verifying the lidar elevation data's vertical accuracy. Ground survey operations to support this project were largely accessible only by boat.

Results Benefit A Wide Array of Applications

While this project was conducted for NOAA's coastal mapping program, the data collected will be far reaching in support of a variety of important applications when made available to other federal, state, local, and tribal government agencies; the private sector; not-for-profit, and the public.

For example, topobathymetric data can provide insights that:

- Support maritime trade and transportation
- Inform wave and wind energy site selection
- Contribute to coastal resiliency efforts, such as modeling sea level change, storm surge, coastal flooding, and pollution trajectories
- Help analyze and monitor the environment and critical habitats
- Assist in developing land and marine GIS base layers

Overall, the topobathymetric lidar collected for NOAA's CMP demonstrates the strength of the technology for mapping logistically and environmentally challenging environments. The implications for supporting larger mapping efforts, such as the Alaska Coastal Mapping Initiative, cannot be understated. With careful sequencing and planning, a symbiotic relationship is formed where technologies complement each other to increase data coverage in an efficient and safe way.

If you'd like to learn more about NV5 Geospatial's work in Alaska or its topobathymetric capabilities, visit nv5geospatial.com.

About the Authors

Alexa Ramirez is an eGIS Program Manager for NV5 Geospatial. She is certified as a PMP and GISP and holds a Master of Science in Geological Oceanography from the University of South Florida. She has considerable experience managing some of the firm's largest and most complex projects.

Colin Cooper, GISP is a Technical Domain Expert for NV5 Geospatial in the fields of topographic and bathymetric lidar. He holds a Master of Science in Geography from Oregon State University.

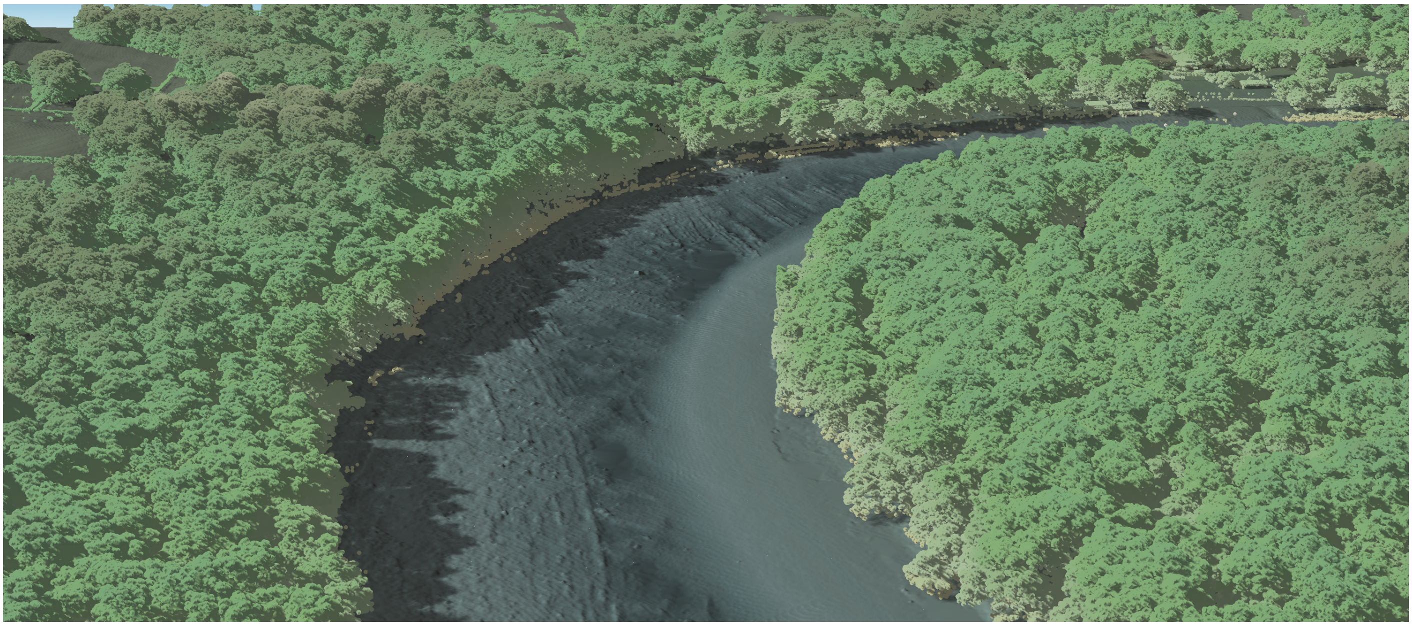

Dewberry is a leading, market-facing firm with a proven history of providing professional services to public- and private-sector clients. Established in 1956 and headquartered in Fairfax, Virginia, Dewberry's professionals are dedicated to solving clients' most complex challenges and transforming their communities. The firm harnesses the power of geospatial science to offer complete end-to-end remote sensing and mapping services starting with state-of-the-art airborne lidar sensors to automated processing, surveying, web/mobile GIS, and advanced data analytics. Dewberry creates, analyzes, and builds geospatial data and tools, to help clients integrate, share, and simplify the use of information allowing for more effective and efficient decision making.

Dewberry's geospatial and technology services team includes more than 250 professionals who create, analyze, and build tools to share geospatial data, and help clients integrate these tools into their daily lives. By fusing multiple data sets together for more efficient data mining, Dewberry provides clients with easy-to-use tools that simplify the use of information to allow for more effective and efficient decision making.

Dewberry recently purchased two airborne lidar sensors – the RIEGL VQ-1560 IIS topographic airborne lidar sensor and the Teledyne CZMIL SuperNova, a powerful topobathymetric mapping sensor. This investment allows Dewberry to expand its mapping capabilities with current clients, keep the entire acquisition lifecycle in-house, and monitor the quality of its products. The firm is excited to empower their clients with access to the most innovative technology to meet their topographic/lidar needs, delivering hi-definition lidar datasets quickly and efficiently.

Dewberry has also implemented two initiatives to facilitate client communication and data processing efficiency. The firm is using Esri-powered, client-facing dashboards combined with quick-look technology, allowing clients to view data acquisition in near real-time and be an active partner in remote sensing activities. The second initiative focuses on improved feature extraction efficiency through automation. Dewberry's IT-team built custom multi-threaded, extended-memory computers dedicated for artificial intelligence (AI)/machine learning (ML) processing. These computers are used for feature extraction and automated classification of lidar data. This AI/ML workflow increases efficiency and decreases delivery time of geospatial products to clients.

The firm's solid performance processes in geospatial technologies and corporate IT services led to it being appraised at Level 3 of the CMMI Institute's Capability Maturity Model Integration (CMMI) in Services and Development Models. In 2021, Dewberry received industry-wide recognition, including five awards from Esri, the American Society for Photogrammetry and Remote Sensing (ASPRS), the Management Association for Private Photogrammetric Surveyors (MAPPS), and the Grand Award and the Pinnacle Award from the American Council of Engineering Companies (ACEC).

Dewberry works seamlessly to provide geospatial mapping and technology services (GTS) across various market segments. With more than 48 years of GTS experience, the firm is dedicated to understanding and applying the latest tools, trends, and technologies. Dewberry employs the latest GIS software and database platforms, including the full suite of ESRI products. The firm's products and services include application, web, and cloud-based development; system integration; database design mapping; data fusion; and mobile solutions. To learn more, visit www.dewberry.com.

Dewberry
Amar Nayegandhi
1000 North Ashley Drive, Suite 801, Tampa, FL 33602-3718
813.421.8642 I www.dewberry.com
anayegandhi@dewberry.com

Dewberry®

GIS Tips & Tricks

Al Karlin, Ph.D. CMS-L, GISP

Need a Custom USGS Topo Map? Here is How to Make it Yourself!

Introduction

The United States Geological Survey (USGS) has over 140 years of experience in providing high-quality topographic maps in the US. In 1879, the USGS began to map the Nation's topography. This mapping was done at different levels of detail, to support various land use and other purposes. As the years passed, the USGS produced new map versions of each area. These maps were published at several scales, the most popular being the 1:24,000 scale which displayed 7.5-minute quadrangle published between 1947 – 1992.

In 2011, as a goal of the Historic Topographic Map Collection (HTMC), the USGS constructed a digital repository of USGS 1:250,000 scale and larger maps printed between 1884 and 2006. There are currently over 178,000 maps in this historic collection in addition to the current digital US Topo series. Both the HTMC and the US Topo series are available as GeoPDFs through The National Map (https://www.usgs.gov/programs/national-geospatial-program/national-map) and the USGS Store (https://store.usgs.gov/).

But … what if you need a topographic map for a small area, or a map for a specific app and do not want to download an entire 7.5-minute USGS quadrangle? Well… the USGS has a solution called "topoBuilder".

Making a Custom Topo Map

"topoBuilder" is a USGS on-demand topo map application that can be accessed through The National Map or directly at: https://topobuilder.nationalmap.gov . The topoBuilder app permits the end-user to make your own topographic map, centered on your specified coordinates, in multiple formats, using the best available National Map data. The following steps demonstrate how to make a custom topo map for an area near Tallahassee, Florida starting at The National Map.

Step 1

From "The National Map" web-viewer, select the topoBuilder app (upper right on banner)

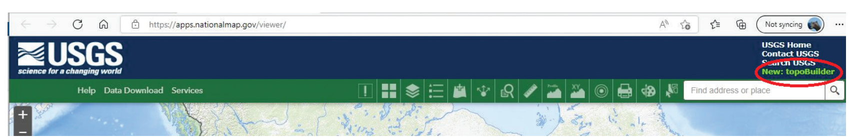

Figure 1. The topoBuilder (green) icon on the U.S. National Map.

Step 2

That will get you to the topoBuilder app and selecting "Create an OnDemand Topo" will get you to the topoBuilder app. (You may need to read and then close any notifications.)

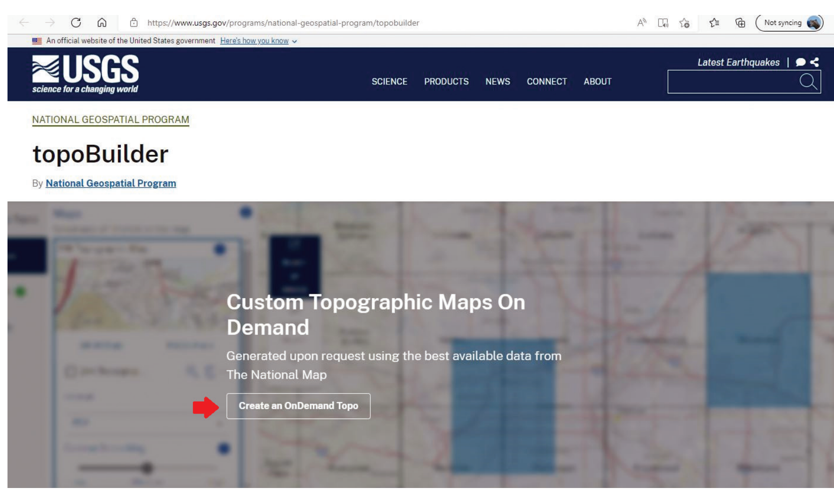

Figure 2. The topoBuilder introductory screen.

Photogrammetric Engineering & Remote Sensing
Vol. 88, No. 10, October 2022, pp. 621-624.
0099-1112/22/621-624

doi: 10.14358/PERS.88.10.624

STEP 3

On the topoBuilder app, select the map type by clicking on the map-type you want to make (in this case there is only the 7.5-minute topo) and click "NEXT" on the bottom center:

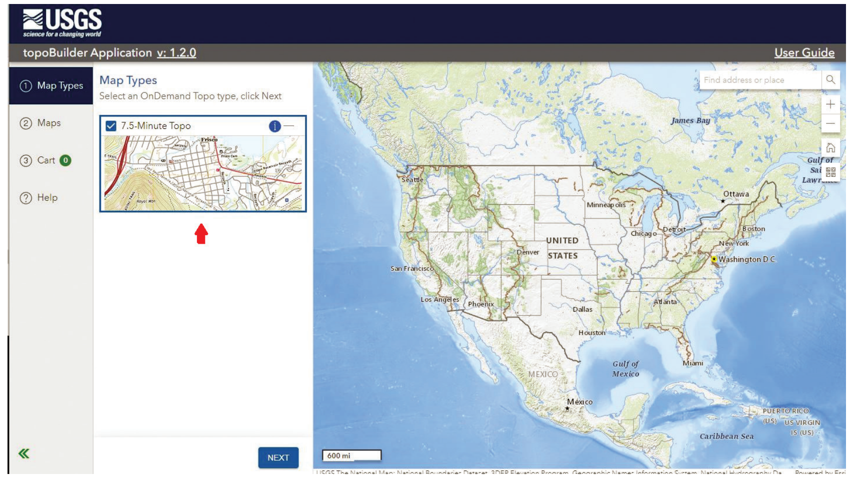

Figure 3. The topoBuilder interactive map interface.

STEP 4

Click on the "Custom Select" and using the mouse wheel, ZOOM-in to your area of interest. When you zoom-in, you will see a blue-shaded box that you can use to select a 7-minute quad area. Position the box centered on your area of interest and click the mouse (left-click) to select that area. In this case, I selected an area around Tallahassee, Florida that is centered on four x 7.5-minute quadrangles.

At this point, you can also choose your export options (PDF is the default, but you can use the dropdown to choose TIF) and choose the amount of Contour Smoothing (default is Medium) by sliding the slider.

Clicking "ADD" will put the map into your cart and go to the next step.

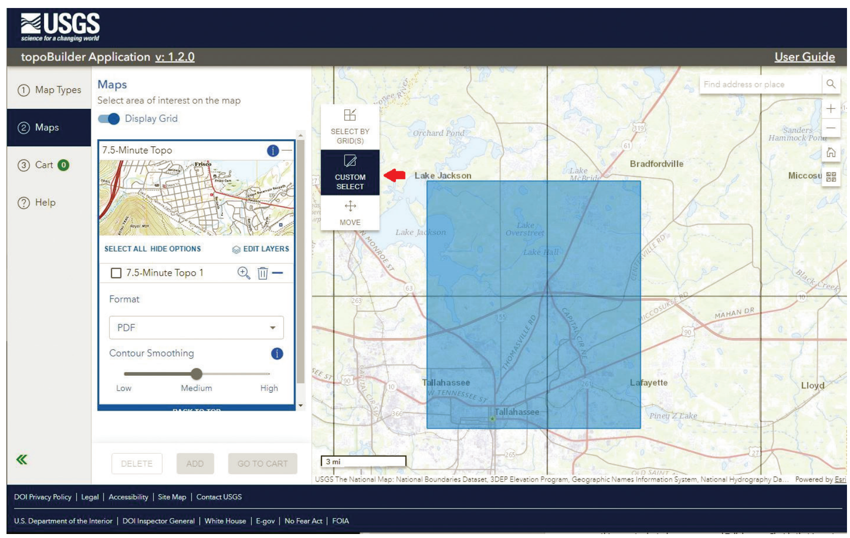

Figure 4. Selecting a custom area of interest on the topoBuilder map interface.

STEP 5

Selecting the EDIT MAPS option will let you review your choices and then pressing SAVE will save your map

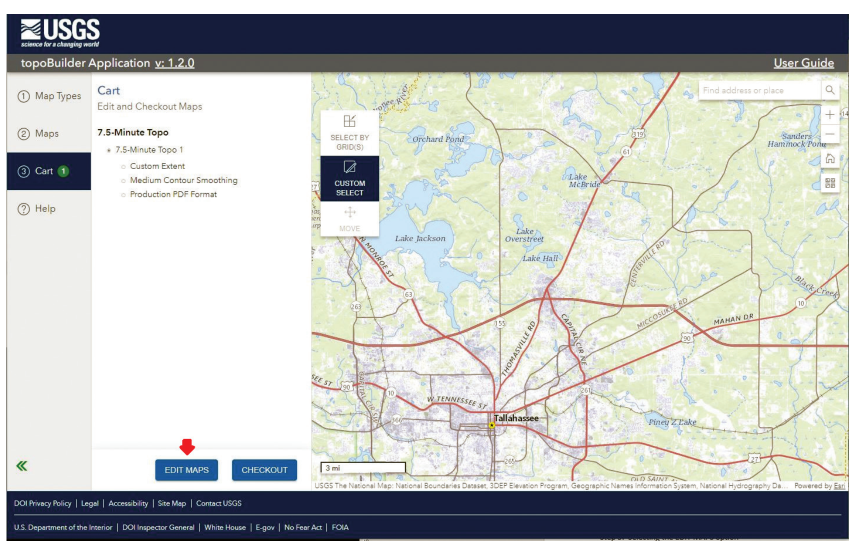

Figure 5. The Cart resulting from a custom area of interest from topoBuilder.

Step 6

Use the CHECKOUT button to finalize your order and get to the Check Out screen where you will enter your e-mail address and press CHECKOUT (again):

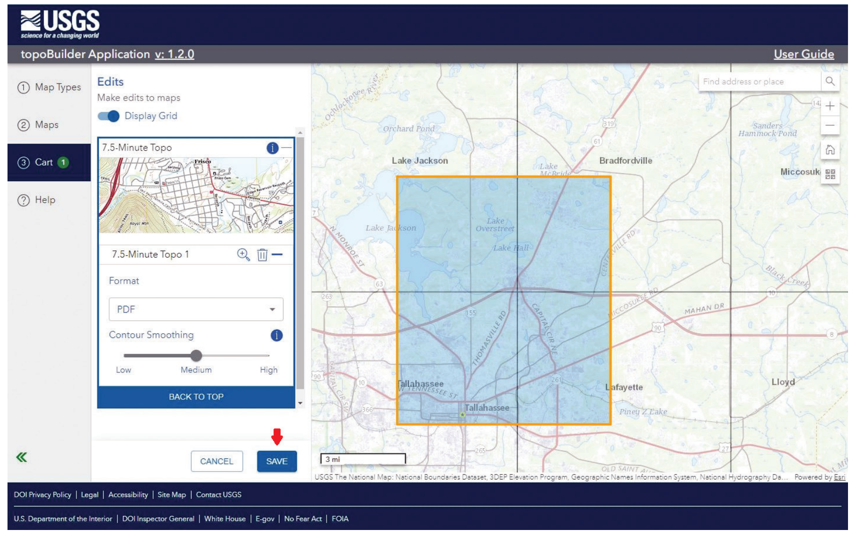

Figure 6. The confirmation and checkout screen from topoBuilder.

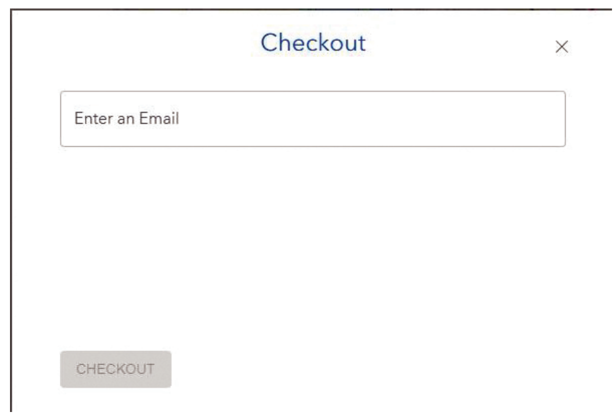

Figure 7. The Checkout Screen from topoBuilder. You need to enter your e-mail address to be used for sending the link to your quadmap. Once your e-mail address is entered, press “CHECKOUT” to complete.

The app will process your request, and after a short time, will return:

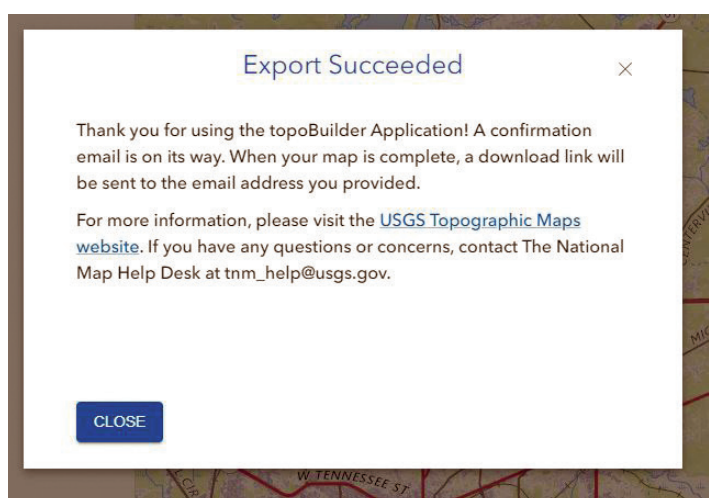

Figure 8. The Export Succeeded screen topoBuilder generates when your map has been successfully generated.

You can CLOSE this notice and you will receive an e-mail message that your map is being processed. When your map is ready, you will receive another e-mail with a link and download instructions.

Here is my finished map. Notice that there are no collars around the four 7.5-minute quadrangles that comprise my map and you can see the specific area (red rectangle) on the map collar,

Additional help is available at: https://www.usgs.gov/programs/national-geospatial-program/topobuilder and tnm_help@usgs.gov. Special thanks to Alexandra “Xan” Fredericks (AFredericks@USGSgov). Xan is the USGS National Map Liaison to Florida, Puerto Rico and the US Virgin Islands and demonstrated the topoBuilder application during the Spring 2022 Fl-ASPRS/UF Lidar Workshop. She is also a past president of the Florida Region – ASPRS.

Send your questions, comments, and tips to GISTT@ASPRS.org.

Al Karlin, Ph.D., CMS-L, GISP is with Dewberry’s Geospatial and Technology Services group in Tampa, FL. As a senior geospatial scientist, Al works with all aspects of Lidar, remote sensing, photogrammetry, and GIS-related projects. He also teaches beginning map making at the University of Tampa.

Figure 9. The final topoBuilder map for the area of interest. Note (1) the area of interest is shown in the red box on the map collar, and (2) that the collars of the four USGS quadmaps have been removed to make a single mosaic.

Surdex Corporation: Your Strategic Geospatial Resource

Surdex Corporation is a full-service photogrammetric mapping firm in St. Louis, Missouri, that has served public and private sectors for over 65 years. Our focus is to consistently deliver premium quality geospatial products. Our extensive acquisitaon and processing resources provide a significant production capacity, ensuring we have the ability to meet your schedule without compromising quality. Our experience, communications and production procedures ensure every project is given a custom design and executed in a manner that will meet all project specifications – *first time right, on time.*

Our services include:

- Aerial imagery and lidar acquisition
- Lidar processing
- Digital orthoimagery production
- Planimetric mapping
- Topographic mapping
- Disaster mapping

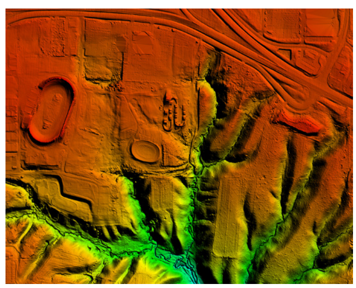

We serve a wide range of both public and private sector clients:

- Municipal, county, state and federal government entities (including DOTs)
- Surveyors
- Engineering and construction firms
- Energy firms (oil and gas, solar, and wind)

Surdex's aircraft, supported by in-house maintenance personnel, and sensors are key to successfully completing numerous simultaneous projects across the country. Our acquisition assets include:

- A fleet of 10 Cessna aircraft
- 9 digital image sensors – 5 Leica ADS100s and 4 DMC-Is
- 3 lidar sensors – 2 Galaxy T2000s and 1 Galaxy Prime

We maintain a staff of approximately 100 employees including many with degrees in mapping or engineering fields. Our staff includes 8 ASPRS Certified Photogrammetrists, 1 ASPRS CMS-Lidar, 1 ASPRS CMT-GIS, 1 GISP certification, 2 Registered Land Surveyors and 1 Project Management Professional (PMP) certification. This depth of skilled professionals enables us to carefully design a custom plan for each project, to avoid issues and to mitigate them if they do occur.

In addition to completing numerous county/municipal government projects annually, Surdex is a prime contractor on several national multi-year programs such as the USDA PINE and the USGS GPSC4 program, and we have an IDIQ contract with the US Army Corps of Engineers for Surveying and Mapping. We also have a GSA contract for Earth Observation Solutions and numerous state DOT contracts.

Surdex routinely undertakes projects ranging in size from a single development site to an entire state. Our production capacity and project management enable us to manage numerous concurrent projects – and to deliver a quality product that meets each project's specifications and schedule. We institute redundant quality control processes and inspections at every major production phase, assuring that no work proceeds to the next step until it is validated against project standards. Consequently, Surdex's products live up to our clients' expectations for quality and accuracy.

If receiving a quality product in a timely manner is important to you, call Surdex to see how we can help.

Surdex Corporation
520 Spirit of St. Louis Boulevard
Chesterfield, MO 63005
(636) 368-4400 I www.surdex.com

SURDEX CORPORATION

STAND OUT FROM THE REST

EARN ASPRS CERTIFICATION

ASPRS congratulates these recently Certified and Re-certified individuals:

RECERTIFIED PHOTOGRAMMETRIST

Charles E. Meyers, Certification #R1329CP
Effective May 23, 2022, expires May 23, 2027

Bryan O'Malley, Certification #R1326CP
Effective May 2, 2022, expires May 2, 2027

Edward Rodrigue, Certification #R968CP
Effective April 3, 2022, expires April 3, 2027

Jason Dolf, Certification #R1488CP
Effective April 19, 2021, expires April 19, 2026

Matthew Doty, Certification #R1580CP
Effective March 16, 2020, expires March 16, 2025

Craig Fry, Certification #R1336CP
Effective October 7, 2022, expires 7, 2027

RECERTIFIED LIDAR TECHNOLOGIST

Matthew Doty, Certification #R043LT
Effective May 13, 2022, expires May 13, 2025

RECERTIFIED MAPPING SCIENTIST GIS/LIS

William M. Stiteler, Certification #R190GS
Effective April 11, 2022, expires April 11, 2027

RECERTIFIED REMOTE SENSING TECHNOLIGIST

Kevin F. May, Certification #R202RST
Effective March 12, 2021, expires March 12, 2024

RECERTIFIED MAPPING SCIENTIST – REMOTE SENSING

William M. Stiteler, Certification #R154RS
Effective April 4, 2022, expires April 4, 2027

CERTIFIED MAPPING SCIENTIST GIS/LIS

Wesley Street, Certification #GS268
Effective July 13, 2022, expires July 13, 2027

Hurmain Ariffin, Certification #GS312
Effective July 29, 2022, Expires July 29, 2027

ASPRS Certification validates your professional practice and experience. It differentiates you from others in the profession. For more information on the ASPRS Certification program: contact **certification@asprs.org**, visit **https://www.asprs.org/general/asprs-certification-program.html.**

Ad Index

Dewberry	www.dewberry.com	620
Surdex Corporation	www.surdex.com	625

Grids & Datums

GRENADA

BY Clifford J. Mugnier, CP, CMS, FASPRS

The Grids & Datums column has completed an exploration of every country on the Earth. For those who did not get to enjoy this world tour the first time, *PE&RS* is reprinting prior articles from the column. This month's article on Grenada was originally printed in 2005 but contains updates to their coordinate system since then.

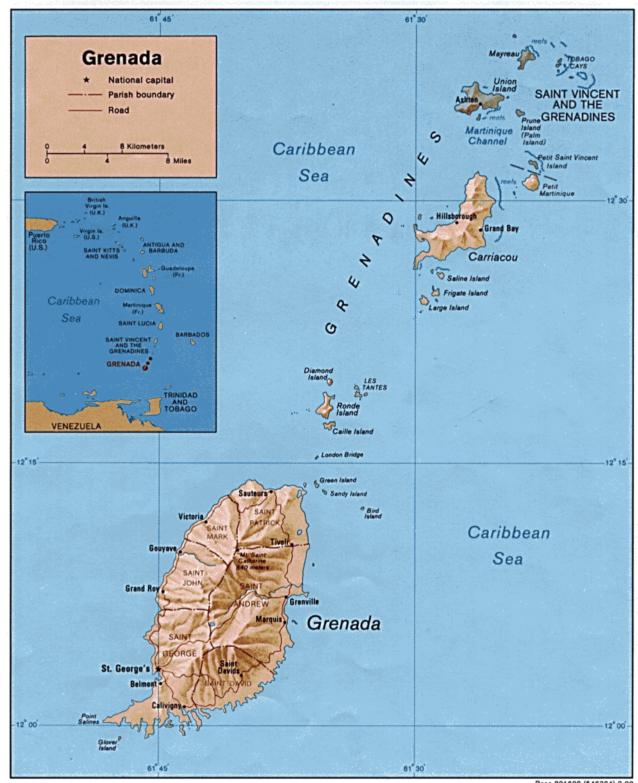

Discovered by Christopher Columbus in 1498 on his third voyage, the island was not settled until 1609 when the English attempted to establish tobacco plantations. Native Carïb Indians made numerous raids on the English settlers and convinced them to abandon the island. In 1650, the governor of Martinique purchased Grenada from the Carïbs, and resettled the island with about 200 French citizens. After a year of subsequent raids by the Carïbs, a contingent of French soldiers was sent to Grenada to secure the island. The Carïbs were routed at Sauteurs Bay, but rather than surrender, the entire Carïb population leaped to their deaths from the island cliffs. Thanks to *Lonely Planet* 2004: "The French then set about establishing plantations of indigo, tobacco, coffee, cocoa and sugar, which were worked by African slaves. Grenada remained under French control until captured by the British in 1762.

Over the next two decades it teetered between the two colonial powers until it was ceded to the Brits in 1783. It remained under British rule until independence, though animosity lingered between the British colonialists and the minority French settlers, with violence erupting periodically. In 1877, Grenada became a Crown Colony. In 1967, Grenada became an associate state within the British Commonwealth. Grenada and the neighboring Grenadine Islands of Carriacou and Petit Martinique adopted a constitution in 1973 and became an independent nation in 1974."

Dubbed the "Spice Island" because of its impressive production of nutmeg, mace, cinnamon, ginger, and cloves, Grenada has a rugged mountainous interior of rainforests and waterfalls and an indented coastline with protected bays and secluded beaches. Grenada is comprised of the islands of Grenada, Carriacou, and Petit Martinique. Located just north of Trinidad and Tobago (*PE&RS*, November 2000), and just south of St. Vincent (*PE&RS*, February 2004), the area of Grenada (340 km^2), is twice the size of Washington, D.C. With a coastline of 121 km, the terrain is volcanic in origin with central mountains. The lowest point is the Caribbean Sea, and the highest point is Mount Saint Catherine (840 m).

The British Directorate of Colonial Surveys (DCS) flew the first aerial photography of Grenada in 1951. The original geodetic surveys of the island were performed by DCS in 1953, and the origin point is the astronomical station GS 8,

Photogrammetric Engineering & Remote Sensing
Vol. 88, No. 10, October 2022, pp. 627-628.
0099-1112/22/627-628

doi: 10.14358/PERS.88.10.627

Santa Maria (at the Santa Maria Hotel yard), where: Φ_o = 12º 02´ 36.56˝ N and Λ_o = 61º 45´ 12.495˝ West of Greenwich. The defining azimuth to G5 North Extension is α_o = 207º 30´ 46.55˝ East of North, and scale is defined by the length from G1 West Base (Grand Anse Rum Distillery Hill) to G2 East Base (SE of the Grand Anse Rum Distillery chimneys) of 1991.394 meters. The height of Santa Maria (H_o) = 160.24 feet, determined by leveling from the Colony bench mark at St. Georges Harbor which is 3.17 feet above mean sea level. The ellipsoid of reference is the Clarke 1880 where: a = 6,378,249.145 m, $^1/_f$ = 293.465. The grid system used for Grenada is the BWI Transverse Mercator Grid where the central meridian, λ_o = 62° W, the latitude of origin φ_o = equator, the scale factor at the latitude of origin m_o = 0.9995, False Easting = 400 km, and False Northing = nil. The formulae are the Gauss-Krüger, but for such a small span of latitude and longitude that includes all three islands; the distinction in this case is irrelevant. As is common with the BWI Grid usage, the grid is used as an "atlas index" numbering system for the popular tourist maps, and is not numbered with coordinate values but with an alphanumeric system for facile use to locate tourist interest points. The grid is easy to recover if one is familiar with the standard BWI grid conventions, but the defining parameters are unfortunately obscure to many.

"In Grenada, four Navy A-7 Corsair aircraft strafed a U.S. Army command post, inflicting 17 American casualties (Doton, *Acquisition Quarterly Review*, 1996). That tragedy highlighted the Services' failure to establish a common positional picture. Each Service brought its own maps and map systems to the fight. The ground forces were unable to accurately describe a point on the ground to the supporting pilots. Air, ground, and sea Services planned and operated using separate maps referenced to three distinctly different coordinate systems. Accustomed to large-scale maps depicting terrain in familiar grids, Army units deploying from Fort Bragg used maps constructed by the Army's 100th Engineer Company (Cartographic), from a tourist map with an arbitrary grid overlay. Despite pictures of palm trees in the margins, the map was excellent. Constructed by British military engineers, the base map included highly accurate survey data replete with topographic contours. The American Army engineers merely added black grid lines for ground troops to use as a grid reference system. While this worked well for the Army, coordinates from the gridded overlay were useless to any combatant without a copy of the modified tourist map. Some historians link the strafing of the U.S. Army command post to this lack of a common positional picture.

"Ground units experienced difficulty in orienting themselves and in directing supporting gunfire and airstrikes. [This] inadvertent airstrike…has been blamed partly on this chart confusion problem" (Rivard, *DTIC* 1985). The failure to create a common reference for planning highlighted the Services' utter lack of attention to planning the joint fight. The 'tourist map' debacle merited considerable media attention, providing further grist for 1986 Goldwater-Nichols Act proponents." (Gruetzmacher, Holtery, and Putney , Joint Forces Staff College Joint and Combined Staff Officer School, #02-02, 2002). A GPS survey by the U.S. National Geodetic Survey (NGS) occupied the station GS 15, Fort Frederick in 1996. I computed a singlepoint datum shift relation from Grenada 1953 Datum to WGS 84 Datum as: ΔX = +72 m, ΔY = +213 m, and ΔZ = +93 m. Thanks to Dennis McCleary of NGA for validation that the Santa Maria "astro" position was the same as the geodetic position I received from Dave Doyle of NGS.

UNAVCO installs COCONet cGPS site CN46 in Carriacou, Grenada

Determining how the Caribbean plate moves with respect to the neighboring North America and South America plates has been a major challenge. Geologic plate motion models using seafloor magnetic anomaly rates, transform fault azimuths, and slip vectors are challenging due to sparse data. The only rates come from the Cayman Spreading Center, and seismicity at the eastern boundary is low due to slow convergence. Moreover, the boundary geometry is still unclear, since the Caribbean plate's north and south boundaries are complex deformation zones.

GPS data continue to provide key clues to the Caribbean region's geologic faults. GPS stations are currently being installed as part of the Continuously Operating Caribbean GPS Observational Network (COCONet), strengthening the indispensible collection of data belonging to a region that faces many atmospheric and geologic natural hazards.

While most people in the Caribbean were enjoying their time off for Easter weekend, UNAVCO engineers Jacob Sklar and Michael Fend were installing COCONet GPS site CN46 on Carriacou Island, Grenada April 16 - 24, 2014. Carriacou Island, not to be confused with Curacao, is a two-hour ferry ride north of Grenada. UNAVCO worked closely with Terence Walters of Grenada's National Disaster Management Agency (NaDMA) and Stephen George from the University of the West Indies Seismic Research Centre (UWI). CN46 is co-located with UWI's seismic vault; GPS, meteorological, and seismic data are all being transmitted via a satellite connection. Collaborating with UWI will allow both UNAVCO and UWI personnel to monitor the health of the site.

https://www.unavco.org/highlights/2014/carriacou.html.

This column was previously published in *PE&RS*.

ASPRS ESTES TEACHING EXCELLENCE AWARD: CALL FOR NOMINATIONS

We are seeking nominations for the American Society for Photogrammetry and Remote Sensing (ASPRS).

Estes Teaching award. The Estes Memorial Teaching Award is named in honor of Professor John E. ("Jack") Estes, teacher, mentor, scientist, and friend of ASPRS. The Estes award recognizes individual contributions to higher education in remote sensing and geographic information systems technology with a particular focus on teaching excellence. The Award consists of a presentation plaque and a cash award of $3000 and is presented by ASPRS through the ASPRS Foundation.

Nominations should present evidence for superior teaching, which includes course, curricular and program development, testimonials from supervisors and former students, teaching awards and demonstrated student success.

The nomination materials should include:

i. Letter of nomination.
ii. A Curriculum Vitae.
iii. Evidence highlighting achievement in teaching excellence.
iv. Two letters of recommendation highlighting teaching excellence.

Eligibility to receive the Award is not restricted to members of ASPRS. The Award is made to an individual (or two or more collaborating individuals, provide each played a major role in the achievement) who best meets the criteria established. The Award is not made to companies, agencies, bureaus, schools, or associations; however, their personnel are eligible as individuals to receive the Award.

Please email the nomination materials as a single PDF file to awards@asprs.org. Nominations are due by 15 November, 2022

NEW ASPRS MEMBERS

ASPRS would like to welcome the following new members!

Claudia Elisa Aviles Toledo
John Burgin
Tim Burkholder
Carlos Andres Castillo
Christopher R. Dolly
Nima Esmaeilzadeh
Emily D. Graham, GISP
Kyle Ince
Suraj K C
Jekope Kalinisei
Holly Knox
Michael James Lalla
Vanessa Self Miller
Maria Oreshkina
Julie Patterson
Megan R. Perron
Karoll Quijano
Kjell Ryerson
Joseph Sandy Samberg
Gustavo Serrato
Prof. Daniel Sousa
Dr. Christopher Gayle Tate

FOR MORE INFORMATION ON ASPRS MEMBERSHIP, VISIT
HTTP://WWW.ASPRS.ORG/JOIN-NOW

Call for *PE&RS* Special Issue Submissions

Innovative Methods for Geospatial Data using Remote Sensing and GIS

Internationally comparable data is a global need for managing resources, monitoring current trends and taking actions for sustainable living. Even though there has been a significant progress on geospatial data availability, extensive data gaps are still a major problem for general assessment and supervise the progress through the years. According to United Nations 2022 The Sustainable Development Goals Report, while health and energy sectors have the highest data available, limited data available for climate action.

The COVID-19 crisis has also shown that there are innovative data collection methods utilizing information and computer technologies. However, only 5% of the countries have benefit from remote sensing technologies to measure the impact of COVID-19. Additionally, novel approaches such as artificial intelligence should be used in conjunction with assessments to make sure they are put to use for critical situations.

The recent developments in remote sensing, geographic information systems and ICT have provided a wide accessibility to create geospatial data for various purposes. The proposed special issue focuses on *"Innovative Methods for Geospatial Data using Remote Sensing and GIS" for wide range of applications. This special issue aims to bring researchers to share knowledge and their expertise about innovative methods to contribute to fill data gaps around the world for a better future.*

The proposed special issue aims to contributes ASPRS's key mission on 'Simplify and promote the use of image-based geospatial technologies for the end-user', 'Promote collaboration between end users and geospatial experts to match data and technology to applications and solutions' and 'promote the transfer of geospatial data and information technology to developing nations' by providing innovative methods to create geospatial data using remote sensing and geographic information systems utilizing state-of-the-art developments and solutions.

Deadline for Manuscript Submission—July 1, 2023

Submit your Manuscript to http://asprs-pers.edmgr.com

Guest Editors

Dr. Tolga Bakirman, bakirman@yildiz.edu.tr , *Yildiz Technical University, Department of Geomatic Engineering*, Davutpasa Campus, 34220 Esenler-Istanbul/Turkey

Dr. George Arampatzis, garampatzis@pem.tuc.gr, *Technical University Crete, School of Production Engineering & Management*, 73100 Chania – Crete/Greece

A Novel Residual Attitude Estimation Approach Using Georeferenced Satellite Imagery

Bhaskar Dubey and B. Kartikeyan

Abstract

This article presents an efficient novel approach estimating residual attitude based on geometrically corrected (GEO) satellite images. A technique is presented that uses orbital plane geometry to compute the rotation angle as a function of geographic latitude between GEO image space and radiometrically corrected (RAD) image space. First, a nonlinear forward model is established that translates the residual errors in roll, pitch, and yaw to scan errors and pixel errors in GEO image space. Subsequently, the inverse problem is solved using Newton's method of nonlinear optimization for estimating residual roll, pitch, and yaw. We demonstrate our results on data products of the high-resolution Indian satellites Cartosat-2E and Cartosat-2F. Further, the superiority of the proposed method is established by comparing it with multiple existing methods in the literature. The R^2 measures of goodness of fit for roll, pitch, and yaw estimation based on RAD and GEO products using the proposed method are 0.65, 0.99, and 0.65, respectively; using the existing method, they are 0.074, 0.005, and 0.50.

Introduction

Attitude measurement of a satellite is carried out by the onboard sensors, namely gyroscopes, magnetometers, and star sensors, which are part of the satellite's attitude and orbit control system. Vast literature is available on precise real-time satellite attitude determination and calibration (see, e.g., Grassi 1997; Crassidis *et al.* 2007; Soken *et al.* 2014; Pan *et al.* 2016; Yang *et al.* 2021; and the references therein). Often, there exists residual error in attitude estimation, which is compensated via ground-based calibration with the help of precise ground control points (GCPs; Davison 1986; Radhadevi *et al.* 2011; Chen *et al.* 2017).

The problem of estimating residual attitude of a remote sensing satellite is one of the fundamental interests in accurate georeferencing and geometric calibration (Ford and Zanelli 1985; Tommaselli and Tozzi 1996; Srivastava and Alurkar 1997). Georeferencing is carried out using a physical sensor model that relies on the knowledge of orbit and orientation parameters, both exterior and interior, and digital elevation models (DEMs; Westin 1992; Jiang *et al.* 2022). The geometric rectification can also be carried out through other methods—for instance, rational function model–based methods (Xiong and Zhang 2009; Shen *et al.* 2017; Dubey *et al.* 2019) and equivalent geometric sensor model–based methods (Cao *et al.* 2019). Often, system level geometrically corrected (GEO) products (basic GEO products based on system knowledge alone) have high location errors for various reasons, namely orbit and attitude errors, micro-vibrations of the platform, terrain undulations, and errors in interior orientation parameters. In recent Indian Remote Sensing (IRS) missions, the system-level location error is on the order of 100 to 200 m (Srinivasan *et al.* 2008). A major part of this error is attributed to error in the measurement of satellite attitude by the onboard sensors. Thus, the precise estimation of residual attitude is very important for improving system-level location accuracy, and also for generating more accurate final products. A rigorous in-flight geometric calibration, which also involves compensation for residual attitude biases, is carried out in order to improve the geometric accuracies and overall system-level location errors (Leprince *et al.* 2007; Radhadevi and Solanki 2008; Zhang *et al.* 2014; Wang *et al.* 2017).

In the literature, residual attitude estimation has been explored by various authors in various ways (e.g., Mahapatra *et al.* 2004; Pulsule *et al.* 2008; Weser *et al.* 2008; Dubey and Kartikeyan 2018). Wahba (1965) aimed to find a best-approximating residual orthogonal matrix to minimize the location errors at a few conspicuous points. Mahapatra *et al.* (2004) forged discussions for computing residual attitude based on Taylor-series linearization of the collinearity equations. We (Dubey and Kartikeya 2018) recently established an improved approach for estimating residual attitude based on radiometrically corrected (RAD) products, wherein we directly model the effect of residual roll, pitch, and yaw in terms of scan errors and pixel errors at a few GCPs in RAD image space. Due to this, that approach becomes advantageous in many situations over other methods, especially when a user does not have orbit, attitude, and sensor-model parameters to perform full-fledged geometric calibration for estimating residual attitude biases. The approach is also highly suitable to a data quality evaluation system where the end products are validated for quality norms, namely location errors, targeting errors, internal distortion, and residual attitude, and necessary feedback is provided to concerned data-product generation and mission operations teams.

In this article, our aim is to extend those previous results to GEO products, as these are level 2 products which are frequently demanded by geospatial data users. The image space in GEO products is often rotated with a certain angle based on satellite heading angle and imaging area latitude with respect to the RAD image space, apart from different scales and other terrain-related local distortions. Due to these shortcomings, our previous procedure (Dubey and Kartikeyan(2018), which is valid only for RAD (level 1) products, cannot be applied for residual attitude estimation with GEO products. In this approach, first a conversion of image coordinates from GEO to RAD space is desired, which essentially requires a rotation matrix. The rotation matrix as a function of latitude is derived using the orbital plane geometry and analysis of the ground trace of the satellite. Subsequently, the forward and inverse models are developed for estimating residual attitude using GEO products.

The organization of the paper is as follows: in the next section, we briefly review the results for residual attitude estimation using RAD products that are extended in this article. The following section presents a methodology for estimating residual attitude using GEO products, including a method for estimating rotation angle that is required to conform the GEO image space to the RAD image space. In the section after that, experimental results using Cartosat-2S GEO data products are presented, as are several comparisons with existing results (Pulsule *et al.* 2008; Dubey and Kartikeyan 2018). Finally, we conclude the article.

Review of Residual Attitude Estimation Based on RAD Products

We previously explained in detail the process of residual attitude estimation based on radiometrically corrected products (Dubey and

Bhaskar Dubey and B. Kartikeyan are with the Image Analysis and Quality Evaluation Division of the Signal and Image Processing Group, Space Applications Centre, Indian Space Research Organisation, Ahmedabad, India (bhaskard@sac.isro.gov.in).

Contributed by Hongyan Zhang, December 1, 2021 (sent for review April 8, 2022; reviewed by Mohammed Ahmed Aldelgawy, Zhaojin Li).

Photogrammetric Engineering & Remote Sensing
Vol. 88, No. 10, October 2022, pp. 631–641.
0099-1112/22/631–641

doi: 10.14358/PERS.21-00095R2

Kartikeyan 2018); however, this method cannot be directly applied to GEO images. This is mainly because GEO images do not have the same orientation as RAD images and often are rotated by some angle with respect to RAD images. Contrary to RAD images, GEO images are not in the imaging plane of the satellite. The scan and pixel directions in a GEO image do not represent truth in along- and across-track directions. Thus, our forward model (Dubey and Kartikeyan 2018) describing the effect of residual attitude on the along- and across-track directions does not hold in GEO image space. This necessitates the development of a forward model that can establish a relationship between GEO image scan pixels and residual attitude.

We briefly discuss our previous model for residual attitude estimation using RAD products in order to provide necessary background. We omit the proofs and present only the highlights.

Residual Roll Effect

Let r be the onboard measured roll value and δr the error in measurement of roll. Due to this error, the true location P will be shifted to Q (see Figure 1) in the across-track direction toward the east for near-polar descending satellites. Let P correspond to pixel p and Q to pixel p' in the image. Let s be the scan-line number corresponding to points P and Q. Based on the geometry of Figure 1, we have the following equation:

$$p' = p + \frac{H\delta \mathrm{r}}{d_{\mathrm{p}}} \tag{1}$$

where d_{p} denotes the pixel dimension in meters in the across-track direction and $H=|OP|$ is the altitude of the satellite. This equation can be expressed using a transformation $\mathcal{F}_r:\mathbb{R}^2 \rightarrow \mathbb{R}^2$ defined as

$$\mathcal{F}_r\left(s,p\right) = \left(s, p + \mu_p\delta \mathrm{r}\right) \tag{2}$$

where $\mu_p = H/d_{\mathrm{p}}$ and μ_p is considered the inverse of the instantaneous ground field of view in the across-track direction. It is clear that Equation 1 holds good for the nadir or near-nadir looking satellite. Further, we established previously (Dubey and Kartikeyan 2018) that it will also hold good when the satellite is imaging under higher roll tilt—that is, when r is significantly different from zero.

Residual Pitch Effect

Let δp be the error in pitch measurement by the onboard sensors. Due to this error, the true location will be shifted in the along-track direction (toward the south for a near-polar descending satellite if δp is positive). The geometry for residual pitch effect is the same as for residual roll effect, except that the shift takes place in the scan direction (along-track) instead of the pixel direction (across-track).

Let s and s′ be the scan-numbers corresponding to pitch values of p and $p + \delta p$. Following the same steps as with the residual roll, we get the following equation:

$$s' = s + \frac{H\delta p}{d_s} \tag{3}$$

where d_s is the pixel dimension in meters in the along-track direction. This equation can also be expressed using a transformation $\mathcal{F}_p:\mathbb{R}^2 \rightarrow \mathbb{R}^2$ defined as

$$\mathcal{F}\,(s,p) = (s + \mu_s\delta \mathrm{p}, p) \tag{4}$$

where $\mu_s = H/d_{\mathrm{s}}$

Residual Yaw Effect

Let O_r with coordinates (s_0, p_0) be the origin of the reference frame and O with coordinates (s, p_0) be the origin of rotation (see Figure 2), where p_0 is the center pixel of the detector array and s_0 and s are, respectively, the initial and current scan number. Let $\delta\gamma$ be the residual error in yaw measurement (in Figure 3, $\delta\gamma$ is negatively oriented). The

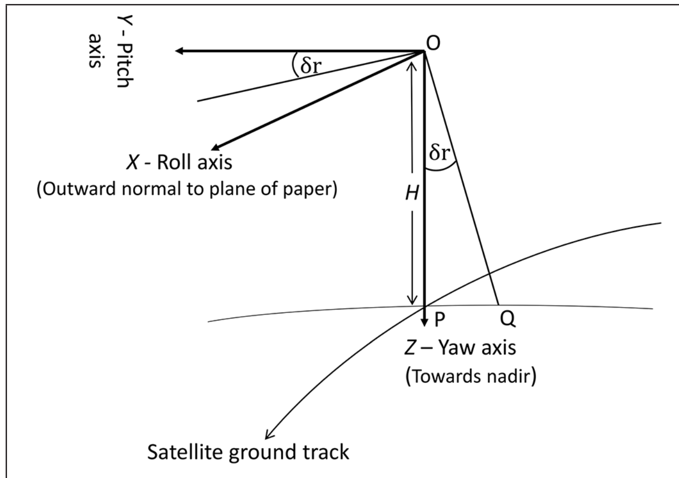

Figure 1. Residual roll effect.

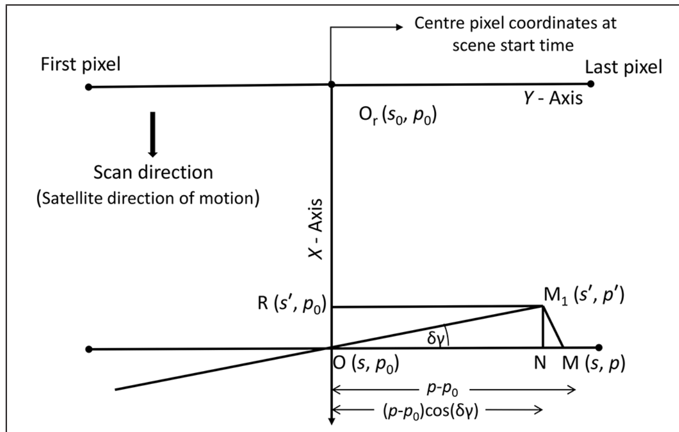

Figure 2. Residual yaw effect.

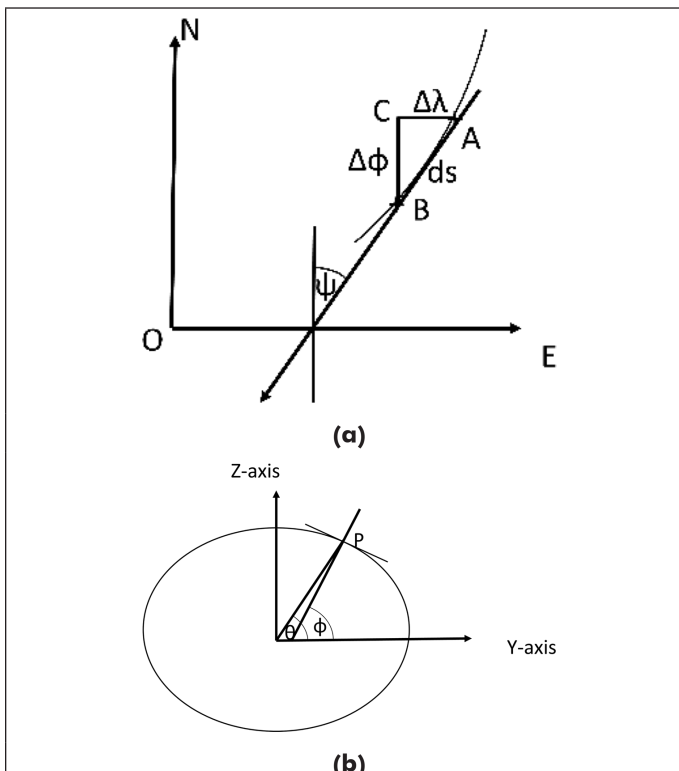

Figure 3. Geometry of radiometrically and geometrically corrected images: (a) Rotation angle. (b) Maximum latitude.

point M, whose coordinates are (s, p), is transformed to the point M_1 with coordinates (s', p') due to the residual yaw error $\delta\gamma$. This transformation $\mathcal{F}_y:\mathbb{R}^2 \to \mathbb{R}^2$ is expressed by the following equation:

$$\mathcal{F}_y = (s,p) = (s + (p - p_0)\sin(\delta\gamma), p_0 + (p - p_0)\cos(\delta\gamma)) \tag{5}$$

Combined Effect of Residual Roll, Pitch, and Yaw

The total effect of residual roll δr, residual pitch δp, and residual yaw $\delta\gamma$ on a pixel with image coordinates (s, p) acting in a sequence in which yaw follows roll and pitch is modeled by a function $\mathbb{F}(F_1, F_2):\mathbb{R}^2 \to \mathbb{R}^2$, where F_1 and F_2 are component functions of $\mathbb{F}$ from $\mathbb{R}^2$ to $\mathbb{R}$, defined as

$$\mathbb{F}(s,p) = \mathcal{F}_y \mathcal{F}_p \mathcal{F}_r (s,p) \tag{6}$$

where $\mathcal{F}_r$, $\mathcal{F}_p$, and $\mathcal{F}_y$ are the mappings from $\mathbb{R}^2$ to $\mathbb{R}$ defined by Equations 2, 4, and 5, respectively. Since a pixel (s, p) is shifted to (s', p') due to the residual errors in attitude, the following equation holds:

$$\mathbb{F}(s,p) + (\eta^S(s,p), \eta^P(s,p)) = (s',p') \tag{7}$$

where $\eta^s(s, p)$ and $\eta^p(s, p)$ are the modeling errors in scan and pixel, respectively. In expanded form, Equation 7 can be written as follows:

$$\begin{bmatrix} s' \\ p' \end{bmatrix} = \begin{bmatrix} 1 & \sin(\delta\gamma) \\ 0 & \cos(\delta\gamma) \end{bmatrix} \begin{bmatrix} s + \mu_s \delta \mathrm{p} \\ p + \mu_p \delta \mathrm{r} \end{bmatrix} + \begin{bmatrix} -p_0 \sin(\delta\gamma) \\ p_0 - p_0 \cos(\delta\gamma) \end{bmatrix} + \begin{bmatrix} \eta^{\mathrm{s}}(s,p) \\ \eta^{\mathrm{p}}(s,p) \end{bmatrix} \tag{8}$$

Without loss of generality, we assume $\mu_s = \mu_p \triangleq \mu$ throughout the rest of the article.

Residual Attitude Estimation Using GEO Products

In this section, we formulate the mathematical model and establish the procedure for the problem of estimating residual attitude using GEO products (level 2 products). These products are obtained from RAD products after applying the ground-to-image mapping over a map projected area followed by resampling of RAD space. Because of this, the RAD and GEO image spaces are not identical even if the resolution is kept the same in both. Therefore, a proper translation and rotation is required on a GEO image for conformation to RAD image geometry. It is often convenient to center the origin of the GEO image before performing rotation.

The residual attitude estimation procedure using GEO products comprises two steps: estimation of the rotation angle required to conform the GEO image to the RAD image and development of the forward and inverse models. Translation is required for centering the origin of the GEO image.

In the next subsection, the procedure for estimating the required rotation angle is provided, and in the subsection after that, the necessary steps are provided for estimating residual attitude using GEO products and model equations are derived.

Estimation of Rotation Angle

The rotation angle essentially depends on the orbit inclination and varies with latitude. Although the rotation angle changes continuously with latitude, nevertheless in practical scenarios where the along-track scene length is not very high, it can be assumed constant throughout the scene (Anuta 1973)). For instance, for a scene with an along-track length of 20 km (~0.2° variation in latitude), the change in the rotation angle is not significant (see Figure 4d). Thus, the rotation angle corresponding to scene-center coordinates is considered for the transformation from GEO to RAD space. Now we shall formulate a method to compute the required rotation angle.

The Earth-centered, Earth-fixed coordinates in terms of latitude ϕ and longitude λ on the Earth's ellipsoid are described by the following equations:

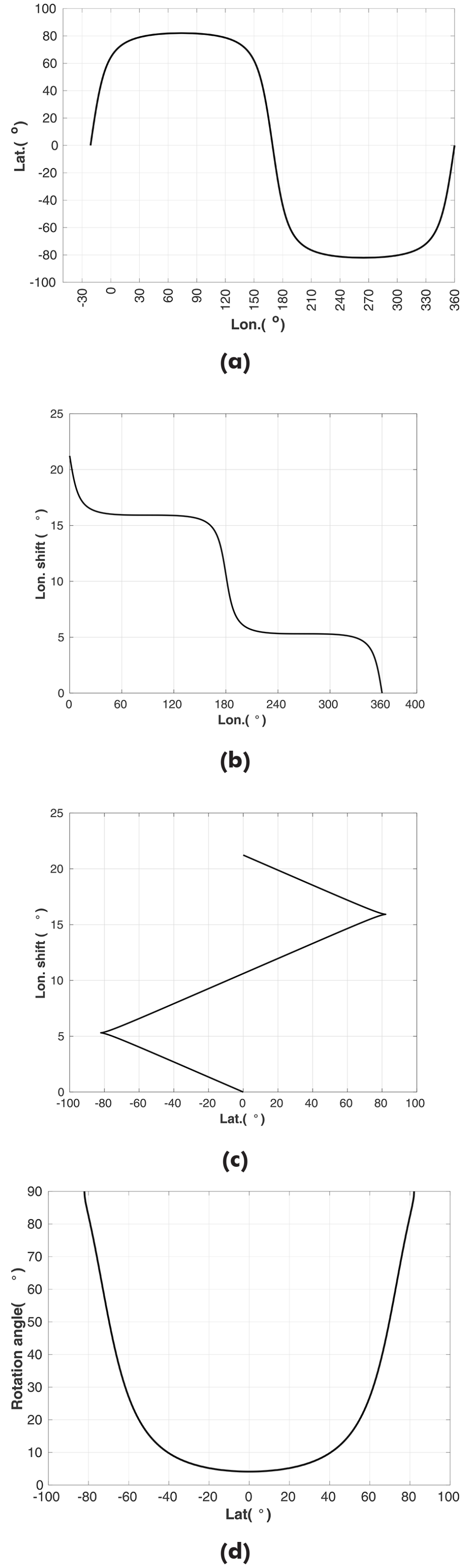

Figure 4. (a) Orbital ground trace considering Earth's rotation. (b) Longitude-shift variation with longitude. (c) Longitude-shift variation with latitude. (d) Rotation-angle variation with latitude.

$$x = \frac{a^2}{r_0}\cos(\phi)\cos(\lambda) \quad (9)$$

$$y = \frac{a^2}{r_0}\cos(\phi)\sin(\lambda) \quad (10)$$

$$z = \frac{b^2}{r_0}\sin(\phi) \quad (11)$$

where r_0 is given by

$$r_0 = \sqrt{a^2\cos^2\phi + b^2\sin^2\phi}$$

in which a and b are the semi-major and semi-minor axis of the Earth. Further, let θ be the inclination of the orbital plane with respect to the equatorial plane, and let ω be the right ascension of ascending node. Then the equation of the orbital plane in the Earth-centered inertial frame will be given by

$$z = -x\sin(\omega)\tan(\theta) + y\cos(\omega)\tan(\theta)$$

Therefore, the ground trace of the satellite orbit, assuming the Earth is stationary, is the intersection of the Earth surface with the orbital plane. Thus, the ground trace trajectory, under a fixed-Earth assumption, is described by

$$\frac{b^2}{r_0}\sin(\phi) = \frac{a^2}{r_0}\cos(\phi)\sin(\lambda-\omega)\tan(\theta) \quad (12)$$

or, equivalently,

$$\tan(\phi) = \frac{a^2}{b^2}\sin(\lambda-\omega)\tan(\theta) \quad (13)$$

Since in a real scenario the Earth is rotating with constant angular velocity, Equation 13 has to be modified to compensate for that rotation. We shall now provide those mathematical formulations.

Compensation for Earth's Rotation

When the Earth's rotation motion is considered, Equation 13 is no longer valid—that is, at any given latitude ϕ, the longitude λ will be shifted by an amount δ_{λ_ϕ}, which is to be determined. Thus, for a rotating Earth, the following relation will hold good for $0 \le \phi \le \phi_{\max}$:

$$\lambda = \omega + \sin^{-1}\left(\frac{b^2}{a^2}\tan(\phi)\cot(\theta)\right) - \delta_{\lambda_\phi} \quad (14)$$

where $\phi_{\max}$ is the maximum latitude that can be attained for the given inclination θ of the orbit; we defer its computation to the next subsection. Without loss of generality, it can be assumed that initially at time $t = 0$, the satellite is crossing the equator—that is, δ_{λ_ϕ} is 0 when ϕ is 0. Under this assumption, we shall compute δ_{λ_ϕ}; it can be done similarly for the other cases. Further, the ground-track velocity of the satellite is nearly constant due to the near-circular orbit. Now, the change in longitude at a latitude ϕ due to Earth's rotation can be obtained by multiplying the Earth's rotation rate by the time of flight from 0 to ϕ. Let δ_{t_ϕ} be the time of flight from 0 to ϕ; then we have

$$\delta_{\lambda_\phi} = \left(\frac{\pi}{43{,}200}\right)\delta_{t_\phi} \quad (15)$$

Here, δ_{t_ϕ} is given by

$$\delta_{t_\phi} = \frac{1}{v_g}\int_0^\phi \frac{ds}{d\phi}d\phi \quad (16)$$

where v_g denotes the average ground-track velocity of the satellite. The integral in this equation denotes the arclength on the ground traversed by the satellite during its motion from 0 to ϕ. The term $d_s/d\phi$ can be expressed as

$$\frac{ds}{d\phi} = \sqrt{\left(\frac{dx}{d\phi}\right)^2 + \left(\frac{dy}{d\phi}\right)^2 + \left(\frac{dz}{d\phi}\right)^2}$$

The functions $x(\phi)$, $y(\phi)$, and $z(\phi)$ can be obtained by combining Equations 9, 10, and 11 with Equation 13. For the special case when $\omega = 0$, they can be expressed as follows:

$$x(\phi) = \frac{a^2}{r_0}\cos(\phi)\sqrt{1 - \frac{b^4}{a^4}\tan^2\phi\cot^2\theta} \quad (17)$$

$$y(\phi) = \frac{b^2}{r_0}\sin(\phi)\cot(\theta) \quad (18)$$

$$z(\phi) = \frac{b^2}{r_0}\sin(\phi) \quad (19)$$

for $0 \le \|\phi\| \le \phi_{\max}$.

Figure 3a shows the necessary geometry required to illustrate the rotation-angle computation. In the figure, $\overrightarrow{ON}$ points toward the north and $\overrightarrow{OE}$ toward the east; points A and B lie on the satellite's ground trace and are separated by an infinitesimally small distance ds. The satellite is descending from north to south and overhead at A. The angle that the negative of the satellite's heading direction makes from true north at A is the rotation angle Ψ that we seek in order to transform satellite imagery from GEO to RAD space. It is expressed by

$$\tan(\Psi) = \lim_{ds\to 0}\frac{\Delta\lambda}{\Delta\phi} = \frac{d\lambda}{d\phi}$$

That is, given a latitude ϕ, the rotation angle Ψ is given by

$$\Psi = \tan^{-1}\left(\frac{d\lambda}{d\phi}\right) \quad (20)$$

Now, from Equation 14 we have

$$\frac{d\lambda}{d\phi} = \frac{d}{d\phi}\left(\sin^{-1}\left(\frac{b^2}{a^2}\tan(\phi)\cot(\theta)\right) - \delta_{\lambda_\phi}\right)$$

which can be rewritten using Equations 15 and 16 as

$$\frac{d\lambda}{d\phi} = \frac{d}{d\phi}\left(\sin^{-1}\left(\frac{b^2}{a^2}\tan(\phi)\cot(\theta)\right)\right) - \frac{\pi}{43{,}200v_g}\frac{d}{d\phi}\left(\int_0^\phi \frac{ds}{d\phi}d\phi\right) \quad (21)$$

Computation of Maximum Latitude

In this subsection, we shall compute the maximum attainable latitude for the given orbit inclined at an angle θ. Figure 3b illustrates the geometry necessary for this computation. Points of extreme latitude are precisely at the intersection of the prime vertical (the intersection of the Earth's ellipsoid with the $y - z$ plane) and the line $z = y\tan(\theta)$. Therefore, the coordinates (y_0, z_0) of the point P, where the maximum latitude $\phi_{\max}$ is attained, are expressed by the following equations:

$$y_0 = \frac{ab}{\sqrt{b^2 + a^2\tan^2(\theta)}} \qquad z_0 = \frac{ab\tan(\theta)}{\sqrt{b^2 + a^2\tan^2(\theta)}} \quad (22)$$

The latitude $\phi_{\max}$ is given by

$$\tan\left(\phi_{\max}\right) = -\left.\frac{dy}{dz}\right|_{(y_0,z_0)} = \left.\frac{za^2}{yb^2}\right|_{(y_0,z_0)} \tag{23}$$

where $(y^2 / a^2) + (z^2 / b^2) = 1$. Upon further simplification of Equation 23, we get

$$\tan\left(\phi_{\max}\right) = \frac{a^2}{b^2}\tan\theta$$

Numerical Simulation

We have simulated rotation-angle estimation as a function of geographic latitude using Equations 20 and 21 for the near-polar retrograde orbit of *Cartosat-2S* with inclination approximately 98°. For a 98° inclined low-Earth near-polar orbit with v_g taken as 6.9 km/s, the rotation-angle computation simulation is done using MATLAB 16. Figure 4a shows the ground trace of the orbit after considering the Earth's rotation. Figure 4b and 4c shows the shift in longitude against longitudes and latitudes, respectively. Finally, in Figure 4d the rotation angle against latitudes is shown in descending mode. Thus, for a given scene, the amount of rotation is calculated by computing the rotation angle at scene-center latitude.

Modeling of Residual Attitude for GEO Products

We shall now present the mathematical model for estimating residual attitude using georeferenced products. All the algorithm steps are described in a sequential manner. Figure 5 depicts the steps in coordinate conversion from GEO to RAD image space. Let S be the number of scans and P the number of pixels in the GEO image. The following steps are performed:

1. First the origin of the GEO image is shifted to the center from the top left corner. That is, every pixel in the image is subjected to following transformation :

$$\left(s,p\right) \xrightarrow{T_S} \left(s-\frac{S}{2}, p-\frac{P}{2}\right) \triangleq \left(s^c, p^c\right)$$

2. On this shifted image, a rotation T_R: $\mathbb{R}^2 \rightarrow \mathbb{R}^2$ with rotation angle Ψ is performed. That is,

$$\left(s^c, p^c\right) \xrightarrow{T_R} R_\Psi\left(s^c, p^c\right) \triangleq \left(s^c_R, p^c_R\right)$$

where R_Ψ denotes the 2×2 rotation matrix with rotation angle Ψ.

3. Let (s_i, p_i) be the GEO image coordinates of the ith control point and be the image coordinates of the same control point in the GEO image obtained by ground-to-image affine transformation, where the ground coordinates of the control point are taken from the map or qualified reference image. Using steps 1 and 2, all the image-map quadruplets $(s_i, p_i, s_i^\dagger, p_i^\dagger)$, $1 \le i \le n$, corresponding to the n control points in the GEO image are transformed to RAD image space with centered origin. Thus, we have the following linear transformation:

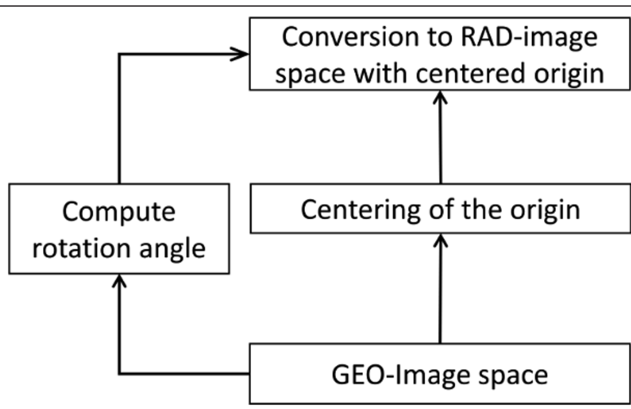

Figure 5. Conversion from GEO to RAD space. GEO = geometrically corrected; RAD = radiometrically corrected.

$$\left(s_i, p_i, s_i^\dagger, p_i^\dagger\right) \xrightarrow{T_R \circ T_S} \left(s^c_{i_R}, p^c_{i_R}, s^{\dagger c}_{i_R}, p^{\dagger c}_{i_R}\right)$$

This equation should be interpreted in the following sense:

$$T_R \circ T_s\left(s_i, p_i\right) = \left(s^c_{i_R}, p^c_{i_R}\right) \tag{24}$$

$$T_R \circ T_s\left(s_i^\dagger, p_i^\dagger\right) = \left(s^{\dagger c}_{i_R}, p^{\dagger c}_{i_R}\right) \tag{25}$$

Note that $T_R \circ T_S$ maps the GEO image coordinates to the RAD image space with centered origin. However, in the model (Equation 8), the actual image coordinates in RAD image space are required. Thus, we need to either convert the centered RAD image coordinates to the original RAD space or Equation 8 needs to be changed in accordance with the centered RAD image coordinate system. Since the RAD image is not available, direct conversion from centered coordinates to the original RAD coordinates is not possible. However, under some reasonable assumption, which is more often the case, forward-model equations with respect to the centered RAD coordinate system can be obtained from Equation 8. This is achieved by eliminating p_0, a number that describes the center of yaw-rotation, from Equation 8. Usually, the center of yaw rotation is considered as half of the total number of detectors in a pushbroom imaging row, but in exceptional cases it can be slightly different from the center of the charge-coupled device (CCD) detectors. Thus in general we can have a safe assumption that p_0 is the center of the CCD detectors. Therefore, Equation 8 can be expressed in p_0-free form by considering the origin of the RAD image to be shifted to the center from the top left corner. Thus, by introducing variables $s_c = s - S_R / 2$ (resp., $s_c' = s' - S_R / 2$) and $p_c = p - P_R / 2$ (resp., $p_c' = p' - R_R / 2$)—where S_R and P_R denote the total number of scans and pixels, respectively, in the RAD image—Equation 8 can be expressed as follows:

$$\begin{bmatrix} s_c' \\ p_c' \end{bmatrix} = \begin{bmatrix} 1 & \sin\left(\delta\gamma\right) \\ 0 & \cos\left(\delta\gamma\right) \end{bmatrix} \begin{bmatrix} s_c + \mu\delta\mathrm{p} \\ p_c + \mu\delta\mathrm{r} \end{bmatrix} + \begin{bmatrix} \eta^{\mathrm{s}}\left(s_c, p_c\right) \\ \eta^{\mathrm{p}}\left(s_c, p_c\right) \end{bmatrix} \tag{26}$$

This is referred to as the forward model. Now, we can use this forward model with inputs $T_R \circ T_S(s_i, p_i, s_i^\dagger, p_i^\dagger)$. It should be noted that the model equations remain valid for conditions of high roll or pitch tilt, and they can also be applied for large-swath satellites. For large-swath satellites, the Earth's curvature needs to be taken in account for precise location of a pixel. The relative error in locating a particular pixel is almost negligible for a low Earth-orbiting satellite, and is around 1% (0.01 pixel) for 2° of roll for geostationary satellites. In Figure 6a, we show the variation of relative percentage change in pixel location due to a flat-Earth assumption for a satellite at an altitude of 600 km; in Figure 6b, the same is shown for a geostationary or geosynchronous satellite. We shall now formulate the inverse model. Let the residual function $\mathcal{R}$: $\mathbb{R}^2 \rightarrow \mathbb{R}^2$ be defined as follows:

$$\mathcal{R}\left(\delta\mathrm{r}, \delta\mathrm{p}, \delta\lambda\right) = \sum_{i=1}^{n} \left(\eta^{\mathrm{s}}\left(s^c_{i_R}, p^c_{i_R}\right)\right)^2 + \left(\eta^{\mathrm{p}}\left(s^c_{i_R}, p^c_{i_R}\right)\right)^2$$

where $\eta^{\mathrm{p}}(s^c_{i_R}, p^c_{i_R})$ and $\eta^{\mathrm{s}}(s^c_{i_R}, p^c_{i_R})$ are the modeling errors at the *i*th GCP in the pixel and scan direction, respectively, and are expressed by

$$\eta^{\mathrm{s}}\left(s^c_{i_R}, p^c_{i_R}\right) = s^{\dagger c}_{i_R} - s^c_{i_R} - \mu\delta\mathrm{p} - \sin\left(\delta\gamma\right)\left(\mu\delta\mathrm{r} + p^c_{i_R}\right) \tag{27}$$

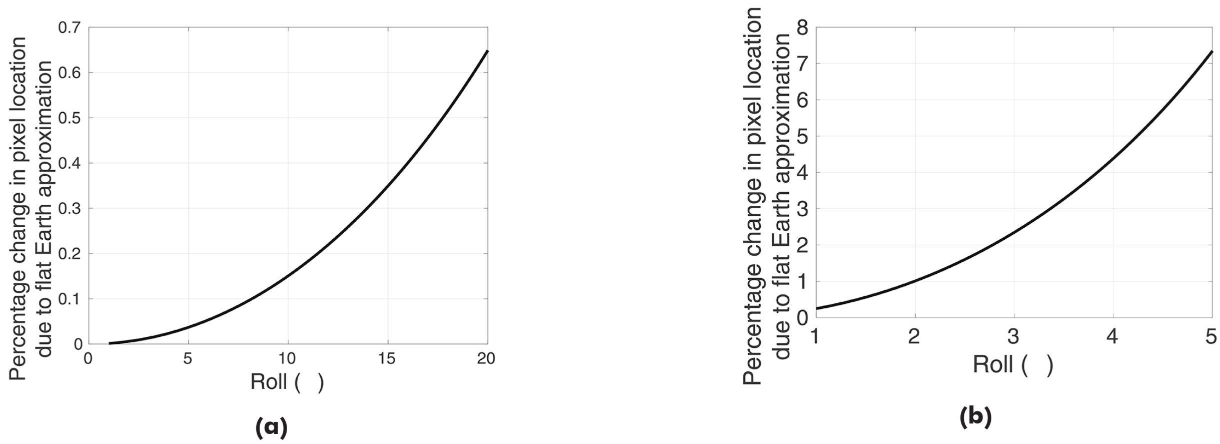

Figure 6. Relative change in pixel location due to Earth's curvature: (a) Low Earth orbits (600 km altitude). (b) Geosynchronous orbits (36000 km altitude).

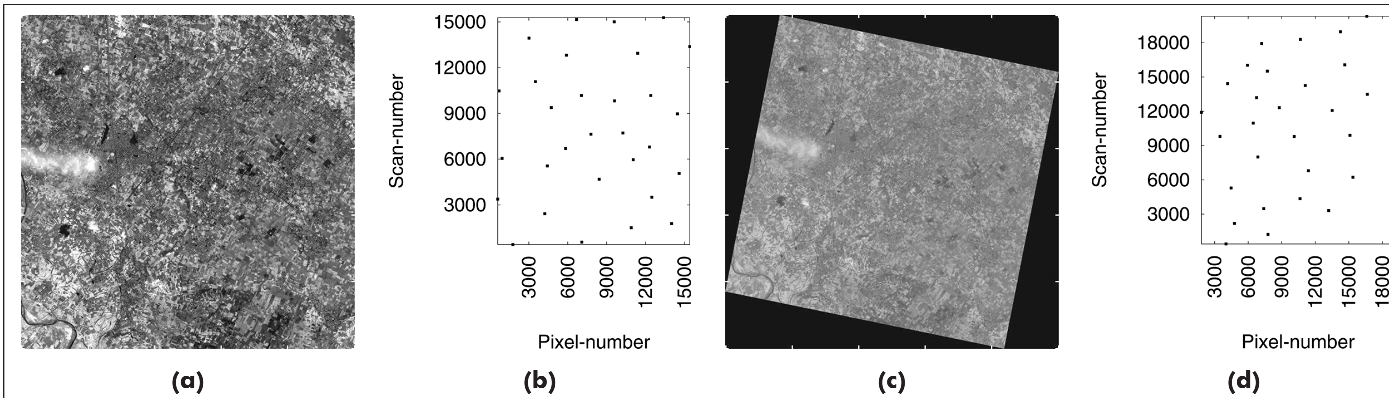

Figure 7. RAD and GEO scenes and their GCP distributions for test 6. GCP = ground control point; GEO = geometrically corrected; RAD = radiometrically corrected. (a) RAD-image. (b) GCPs of RAD-image. (c) GEO-image. (d) GCPs of GEO-image.

$$\eta^{\mathrm{p}}\left(s^{c}_{i_R}, p^{c}_{i_R}\right) = p^{\dagger c}_{i_R} - \cos\left(\delta\lambda\right)\left(\mu\delta \mathrm{r} + p^{c}_{i_R}\right) \tag{28}$$

Now our aim is to solve the following minimization problem: let Ω be a bounded open subset of $\mathbb{R}^3$ —more precisely, a bounded open cube around some suitable guess in $\mathbb{R}^3$ for residual attitude. Consider the problem

$$\left(\mathrm{P}\right) \min_{(\delta \mathrm{r}, \delta \mathrm{p}, \delta\lambda) \in \Omega \subset \mathbb{R}^3} \mathcal{R}\left(\delta \mathrm{r}, \delta \mathrm{p}, \delta\gamma\right)$$

Problem (P) is referred to as the inverse model. This minimization problem can be solved using Newton's method or the Levenberg–Marquardt method (Ruszczyński 2006). We solve it using Newton's method with an appropriate initial guess. In the following section, we invoke the results established in this section to compute the attitude residuals based on GEO products of the high-resolution Indian satellites *Cartosat-2E* and *Cartosat-2F*.

Experimental Results

In this section, we demonstrate our results on the high-resolution Indian satellites *Cartosat-2E* and *Cartosat-2F*. Cartosat-2S is a series of agile high-resolution Indian Earth observation satellites equipped with time-delay integration push-broom imaging technology capable of acquiring images with a resolution of 0.65 m in panchromatic and 1.50 m in multispectral bands. To design a rigorous experiment, we chose a set of ten system-level GEO data products as well as corresponding RAD data products of *Cartosat-2E* and *Cartosat-2F* satellites. Using reference images, well-distributed control points are marked in the GEO image. Subsequently, using the proposed method, residual roll, pitch, and yaw are estimated. It is shown that after application of the residual attitude biases, location errors in all the test scenes are reduced significantly.

As there is a well-established method for residual attitude estimation based on RAD products (Dubey and Kartikeyan 2018), estimated residual attitudes for GEO products are cross verified with the residual attitude estimates based on the corresponding RAD products. We expect that the residual attitude estimates using GEO products should not differ significantly from those obtained using RAD products. Through several comparisons, we establish that indeed there is no significant difference between the residual attitude estimates using GEO products and those obtained using RAD products. We also compare our results with existing results in the literature.

Preparation of Test Data Sets

A set of ten GEO products and corresponding RAD products of different geographic terrains were selected for the analysis of residual attitude estimation results. A typical RAD and GEO product pair, with GCP distribution corresponding to test 6, is shown in Figure 7. The RAD image size is approximately 16,000×16,000 pixels, with a resolution of 0.6 m, whereas the size of a GEO image is approximately 20,000×20,000 pixels, with 0.6-m spatial sampling. The chosen GEO products were generated with system-level accuracy alone, using no other information related to accuracy improvement, alignment angle calibration, or attitude refinement using GCPs. This ensures that the accuracy of the GEO products is equivalent to that of the RAD products. The RAD and GEO data products are compared in terms of location accuracy

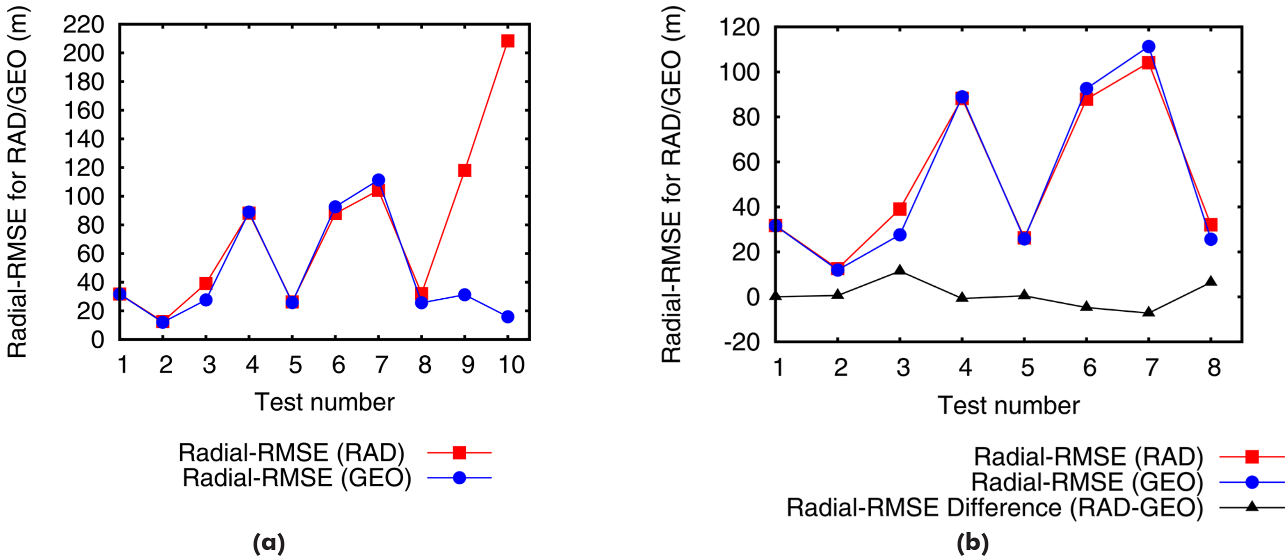

Figure 8. Comparison of radial RMSE using RAD and GEO products. GEO = geometrically corrected; RAD = radiometrically corrected; RMSE = root-mean-square error. (a) Without outlayer rejection. (b) With outlayer rejection.

(root-mean-square error [RMSE]). Figure 8a shows the radial RMSE[1] for both the RAD and GEO products. Tables 1 and 2 present the radial RMSE, mean location errors, standard deviation, and RMSE, both along track and across track, for, respectively, system-level GEO products and corresponding RAD products.

Two cases (tests 9 and 10) show relatively large differences in location accuracy (radial RMSE) between RAD and GEO products—87 and 204 m, respectively, which are much higher than in the other cases. This could be due to some incorrect processing option that led to the generation of accuracy-improved GEO products instead of system-level products. Since in subsequent analyses the attitude residuals estimated using system-level GEO products are compared with those from corresponding system-level RAD products, we do not consider tests 9 and 10 in those analyses. Figure 8b shows the radial RMSE comparison between the RAD and GEO products after tests 9 and 10 are dropped.

Table 1. System-level location accuracy for geometrically corrected products.

			Radial	Location Accuracy (m)					
			RMSE	Along Track[a]			Across Track[b]		
Test	Satellite	Place	(m)	Mean	SD	RMSE	Mean	SD	RMSE
1	*Cartosat-2E*	Akhnur	31.55	31.04	2.39	31.13	−5.53	1.02	5.62
2	*Cartosat-2F*	Anjar	11.26	−8.04	3.82	8.9	−3.4	7.6	8.32
3	*Cartosat-2F*	Chatra	27.38	−24.67	4.84	25.14	−2.59	12.04	12.32
4	*Cartosat-2E*	Fatehabad	88.99	−82.21	3.98	82.31	33.99	1.68	34.03
5	*Cartosat-2F*	Indore	27.04	−26.29	4.01	26.60	−4.56	4.48	6.39
6	*Cartosat-2E*	Jalalabad	92.92	−84.71	2.28	84.74	38.18	0.74	38.19
7	*Cartosat-2E*	Kishangarh	111.56	−106.81	2.36	106.84	32.12	2.73	32.24
8	*Cartosat-2E*	Mukerian	25.83	−23.34	1.04	23.36	−11.06	0.26	11.06
9	*Cartosat-2F*	Gumla	29.78	−28.58	4.44	28.92	4.09	7.62	8.65
10	*Cartosat-2F*	Imphal	17.27	0.64	5.53	5.57	−14.95	4.99	15.76

RMSE = root-mean-square error, [a]Positive values indicate north, negative values indicate south, [b]Positive values indicate east, negative values indicate west.

Table 2. System-level location accuracy for radiometrically corrected products.

			Radial	Location Accuracy (m)					
			RMSE	Along Track[a]			Across Track[b]		
Test	Satellite	Place	(m)	Mean	SD	RMSE	Mean	SD	RMSE
1	*Cartosat-2E*	Akhnur	30.23	29.89	1.01	29.9	−4.3	1.43	4.53
2	*Cartosat-2F*	Anjar	12.8	−3.06	4.88	5.76	−9.18	8.53	12.53
3	*Cartosat-2F*	Chatra	38.04	−24.23	5.44	24.83	28.91	5.36	29.4
4	*Cartosat-2E*	Fatehabad	87.68	−82.09	3.06	82.14	30.68	2.44	30.78
5	*Cartosat-2F*	Indore	25.55	−25.13	4.01	25.45	3.38	3.22	4.67
6	*Cartosat-2E*	Jalalabad	88.34	−82.96	2.0	82.98	30.32	1.86	30.38
7	*Cartosat-2E*	Kishangarh	102.92	−102.43	2.38	102.5	9.32	2.97	9.80
8	*Cartosat-2E*	Mukerian	31.41	−27.8	3.13	27.9	14.42	2.36	14.61
9	*Cartosat-2F*	Gumla	116.6	−34.2	6.17	34.75	111.4	10	111.8
10	*Cartosat-2F*	Imphal	221.86	−21.55	3.53	21.84	222.07	3.53	222.1

RMSE = root-mean-square error, [a]Positive values indicate north, negative values indicate south, [b]Positive values indicate east, negative values indicate west.

Residual Attitude Estimation Results and Discussion

The residual attitude (δ_r, δ_p, δ_λ) is estimated for GEO products using the proposed method. The estimated residual biases are uplinked to the satellite in a specific rotation sequence which modifies the roll, pitch, and yaw rotation matrices, and eventually improves the location accuracy. The complete steps of ground-to-image transformation, which involve the computation of several rotation matrices, have been described previously (Dubey and Kartikeyan 2018).

The effect of residual attitude compensation is indeed in accordance with the forward model (Equation 26). We shall now provide its precise formulation. Let M_r, M_p, and M_y be affine mappings from $\mathbb{R}^2$ to $\mathbb{R}^2$ defined as follows: $M_r(\mathbf{z}) = \mathbf{Iz} + \mathbf{b}_1$, $M_p(\mathbf{z}) = \mathbf{Iz} + \mathbf{b}_2$, and $M_y(\mathbf{z}) = \mathbf{Rz}$, where $\mathbf{I}$ is the 2×2 identity matrix, $\mathbf{b}_1 = (0, \mu\delta r)$, $\mathbf{b}_2 = (\mu\delta p, 0)$, and

$$\mathbf{R} = \begin{bmatrix} 1 & \sin(\delta\gamma) \\ 0 & \cos(\delta\gamma) \end{bmatrix}$$

1. Radial RSME is calculated as $\sqrt{(\mathrm{RMSE}_{al})^2 + (\mathrm{RMSE}_{ac})^2}$, where “al” and “ac” denote the along-track and across-track directions, respectively.

Now, the residual bias compensation law in a GEO image is described as follows: a given pixel $(s, p) \triangleq \mathbf{x}$ in the GEO image obtains its new position as per the following equation:

$$\mathbf{y} = (T_R \circ T_S)^{-1} M_y M_p M_r (T_R \circ T_S)\mathbf{x} \tag{29}$$

After application of the computed attitude biases in accordance with Equation 29, the radial RMSE is shown to decline significantly. The reduction in GEO radial RMSE is also cross verified with the reduction in radial RMSE for corresponding RAD products, whose residuals are estimated using our previous method (Dubey and Kartikeyan 2018). Table 3 presents the original and bias-compensated radial RMSE for both the GEO and RAD products. Figure 9a shows the original and attitude bias-compensated radial RMSE for GEO products, and Figure 9b shows the same for RAD products.

It is clear from Figure 9 that the reduction in RMSE after application of the residual attitude biases for both RAD and GEO products is almost the same. The original error vectors (ten times scaled) and along-track and across-track errors at GCPs for GEO product 6 (Jalalabad GEO scene) are shown in Figure 10, and the same are plotted for the corresponding RAD product 6 (Jalalabad RAD scene) in Figure 11. Similar plots are obtained for rest of the GEO-RAD product pairs.

Comparison with Existing Results

We now show the effectiveness of the proposed approach through several comparisons with existing approaches (Pulsule *et al.* 2008; Srinivasan *et al.* 2008; Dubey and Kartikeyan 2018). According to Pulsule *et al.*, the model equations for residual attitude estimation are valid for polar nadir-looking satellites—that is, the along- and across-track directions are precisely the northing and easting directions on the map. The results of Pulsule *et al.* are not accurate for GEO products based on inclined orbits. Our study confirms that even for a 98° inclined orbit, the net rotation angle that the along- and across-track directions require to conform to northing and easting directions may be significantly large (see, e.g., Figure 4d: at least as large as 27° for imaging at 60° latitude). If this rotation is not properly taken care of, as is the case in the study by Pulsule *et al.*, the results may be misleading. Srinivasan *et al.* used plots of scan differences against scan numbers and pixel differences against scan numbers to derive pitch and roll biases, respectively, and plots of scan differences against pixel numbers to estimate residual yaw. However, their results cannot be directly applied to GEO products, and even for RAD products the combined effect of roll, pitch, and yaw needs to be further investigated.

A comparison of estimated residual attitude using GEO products and corresponding RAD products is carried out using the existing and proposed approaches. Ideally, the estimated residual attitude using RAD products should be approximately equal to that estimated using GEO products. The residual roll, pitch, and yaw for the GEO products and corresponding RAD products differ largely when estimated using the approach of Pulsule *et al.*, whereas our approach shows reliable and promising results. Table 4 shows the estimated residual attitude for the GEO and the corresponding RAD products using the old method; Table 5 presents the estimated residual attitude using our approach. In Table 5, columns 2 through 4 show the estimation carried out using our previous approach for RAD products, and columns 6 through 8 show the estimation using the approach discussed in this article.

Figure 12 shows residual attitude differences between estimation based on the GEO and RAD products using both the old and the proposed approaches. It is clear from the figure that with the new approach, the residual roll and pitch differences are almost close to zero, as desired, whereas residual yaw differences are within 0.02° for most cases and in no case are greater than 0.05°. For comparative analysis, regression lines on the same scale are fitted between the estimated residual attitude for the GEO (y-axis) and RAD (x-axis) products using both approaches, and the slope, offset, and R^2 (measure of the goodness of fit) are computed. Ideally, the slope and offset for the fitted regression lines should be 1 and 0, respectively. A small departure from the ideal slope and offset values can be attributed to inconsistency of location errors and internal distortion between the products; however, a drastic change in the values is undesired. It is shown that the fitted lines for roll and pitch deviate drastically from their expected behavior using the old approach, whereas following the proposed approach they show a close match.

Figure 13 shows scatterplots along with regression lines of estimated residuals using the old method. The slopes and offsets of the fitted lines show huge departures from the expected values of 1 and 0. Figure 14 shows those scatterplots using the proposed method, and it

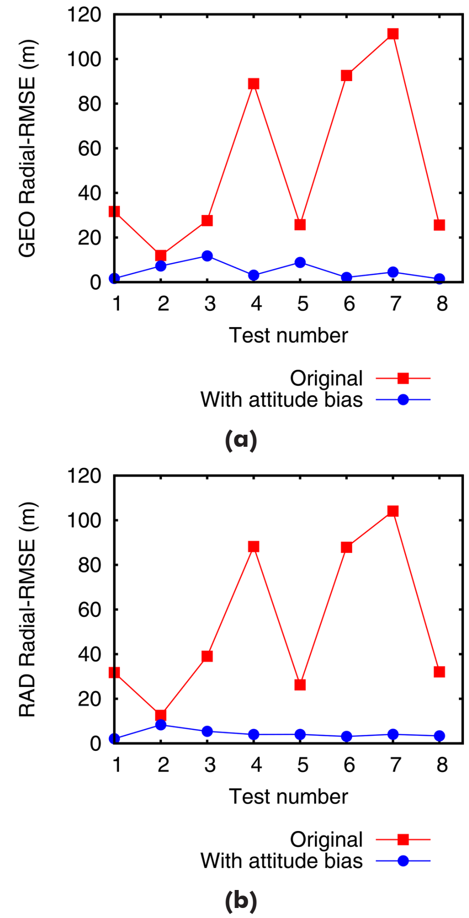

Figure 9. Comparison of radial RMSE for GEO and RAD products before and after residual attitude correction. GEO = geometrically corrected; RAD = radiometrically corrected; RMSE = root-mean-square error. (a) GEO products. (b) RAD products.

Table 3. Original and bias-compensated radial root-mean-square error (m) for RAD and GEO products.

			RAD		GEO	
Test	**Satellite**	**Place**	**Original**	**Bias Compensated**	**Original**	**Bias Compensated**
1	*Cartosat-2E*	Akhnur	30.23	2.10	31.55	1.68
2	*Cartosat-2F*	Anjar	12.80	8.30	11.26	7.23
3	*Cartosat-2F*	Chatra	38.04	5.40	27.38	11.75
4	*Cartosat-2E*	Fatehabad	87.68	4.00	88.99	3.11
5	*Cartosat-2F*	Indore	25.55	4.05	27.04	8.85
6	*Cartosat-2E*	Jalalabad	88.34	3.13	92.92	2.15
7	*Cartosat-2E*	Kishangarh	102.92	4.08	111.56	4.49
8	*Cartosat-2E*	Mukerian	31.41	3.38	25.83	1.48

GEO = geometrically corrected; RAD = radiometrically corrected.

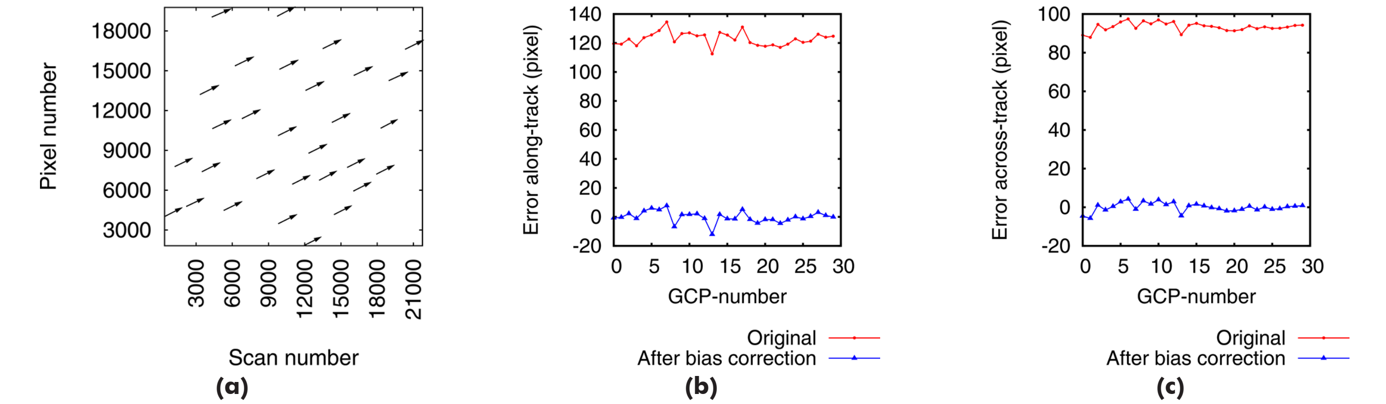

Figure 10. Pre and post residual attitude bias-corrected location errors for geometrically corrected products at GCPs for test 6 (Jalalabad). GCP = ground control point. (a) Original error vectors. (b) Along-track error. (c) Across-track error.

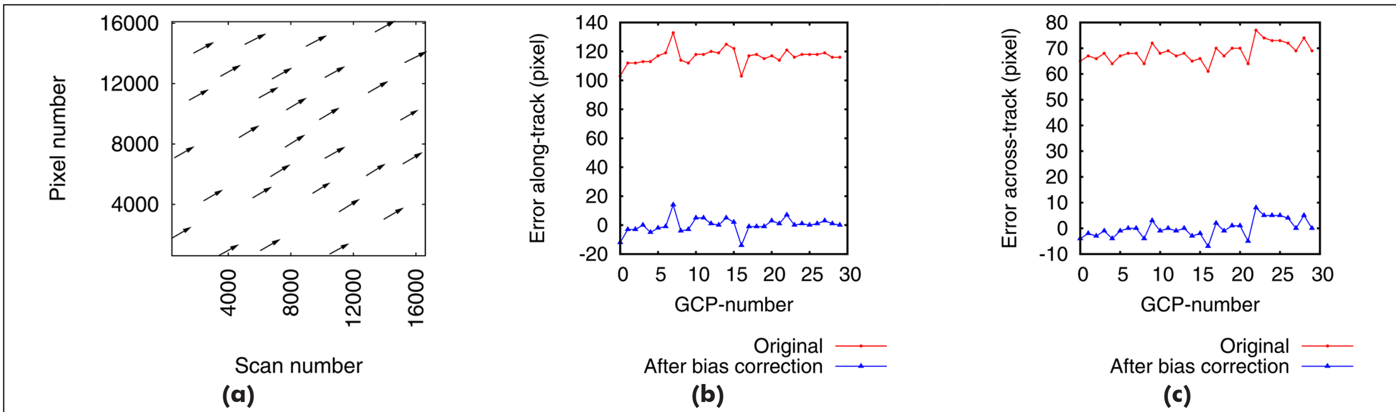

Figure 11. Pre and post residual attitude bias-corrected location errors for radiometrically corrected products at GCPs for test 6 (Jalalabad). GCP = ground control point. (a) Original error vectors. (b) Along-track error. (c) Across-track error.

is observed that the slopes and offsets of the fitted lines are reasonably close to their expected values of 1 and 0.

In Table 6, the slope, offset, and R^2 of regression lines for residual roll, pitch, and yaw are provided for both approaches. It is clear that R^2 estimates of residual attitude using the proposed method are significantly higher than using the existing method. In an ideal situation, when the GEO and RAD product accuracies are almost the same, the R^2 value is expected to be greater than 9. However, the GEO and RAD product accuracies are slightly different in our case, and the exact reasons for this need to be further investigated. Possible causes may include the use of different DEMs for RAD and GEO product generation, terrain distortions, and sampling- and time-related errors (Jiang *et al.* 2022). Nevertheless, through several comparisons it is evident that the proposed method is capable of estimating residual attitude more reliably and accurately than the existing methods in the literature.

Conclusions

In this article, a method for estimating residual attitude using georeferenced data products is developed. The main contributions of the article are summarized as follows:

1. Forward and inverse models for residual attitude estimation based on GEO products are

Table 4. Residual attitude (°) for RAD and GEO products using the old method.

	RAD			GEO			Difference (RAD − GEO)		
Test	Roll	Pitch	Yaw	Roll	Pitch	Yaw	Roll	Pitch	Yaw
1	−0.0005	−0.0034	0.0098	−0.0064	0.0266	0.0330	0.0059	−0.03	−0.0232
2	−0.0011	0.0004	0.0071	0.0082	0.0129	0.0100	−0.0093	−0.0125	−0.0029
3	0.0033	0.0027	0.0920	−0.0920	0.0214	0.0331	0.0953	−0.0187	0.0589
4	0.0035	0.0092	0.0444	0.0003	0.0576	0.0450	0.0032	−0.0484	−0.0006
5	0.0004	0.0028	0.0410	−0.0520	0.0272	0.0209	0.0524	−0.0244	0.0201
6	0.0034	0.0093	−0.0196	−0.0007	−0.0124	−0.0303	0.0041	0.0217	0.0107
7	0.0011	0.0115	−0.0078	0.0185	0.0261	0.0149	−0.0174	−0.0146	−0.0227
8	0.0016	0.0031	−0.0331	0.0026	−0.0007	−0.0031	−0.001	0.0038	−0.03

GEO = geometrically corrected; RAD = radiometrically corrected.

Table 5. Residual attitude (°) for RAD and GEO products using the proposed method.

	RAD			GEO			Difference (RAD − GEO)		
Test	Roll	Pitch	Yaw	Roll	Pitch	Yaw	Roll	Pitch	Yaw
1	−0.0012	−0.0032	−0.0029	−0.0016	−0.0035	−0.0284	0.0004	0.0003	0.0255
2	−0.0011	0.0004	−0.0147	−0.0012	0.0008	−0.0515	0.0001	−0.0004	0.0368
3	0.0039	0.0020	−0.0931	0.0004	0.0029	−0.0476	0.0035	−0.0009	−0.0455
4	0.0052	0.0082	−0.0305	0.0063	0.0086	−0.0536	−0.0011	−0.0004	0.0231
5	0.0009	0.0027	−0.0662	0.00024	0.0029	−0.1115	0.00066	−0.0002	0.0453
6	0.0051	0.0086	0.0282	0.0069	0.0091	0.0281	−0.0018	−0.0005	0.0001
7	0.0032	0.011	0.0141	0.0066	0.0115	0.0111	−0.0034	−0.0005	0.003
8	0.0022	0.0028	0.037	−0.0006	0.0031	0.0126	0.0028	−0.0003	0.0244

GEO = geometrically corrected; RAD = radiometrically corrected.

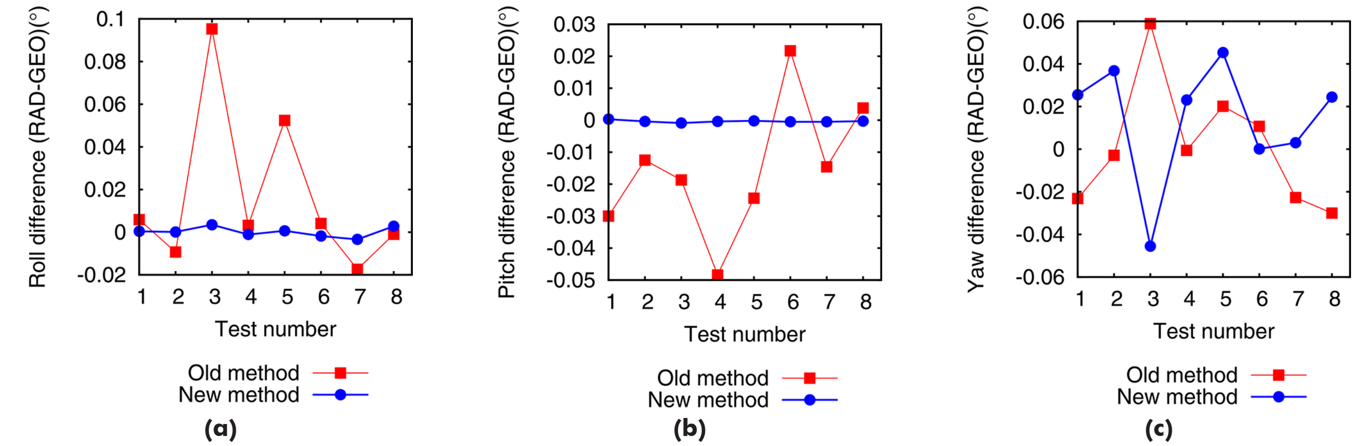

Figure 12. Comparison of differences in residual attitude between RAD and GEO products using the old and new approaches. GEO = geometrically corrected; RAD = radiometrically corrected. (a) Difference in residual roll. (b) Difference in residual pitch. (c) Difference in residual yaw.

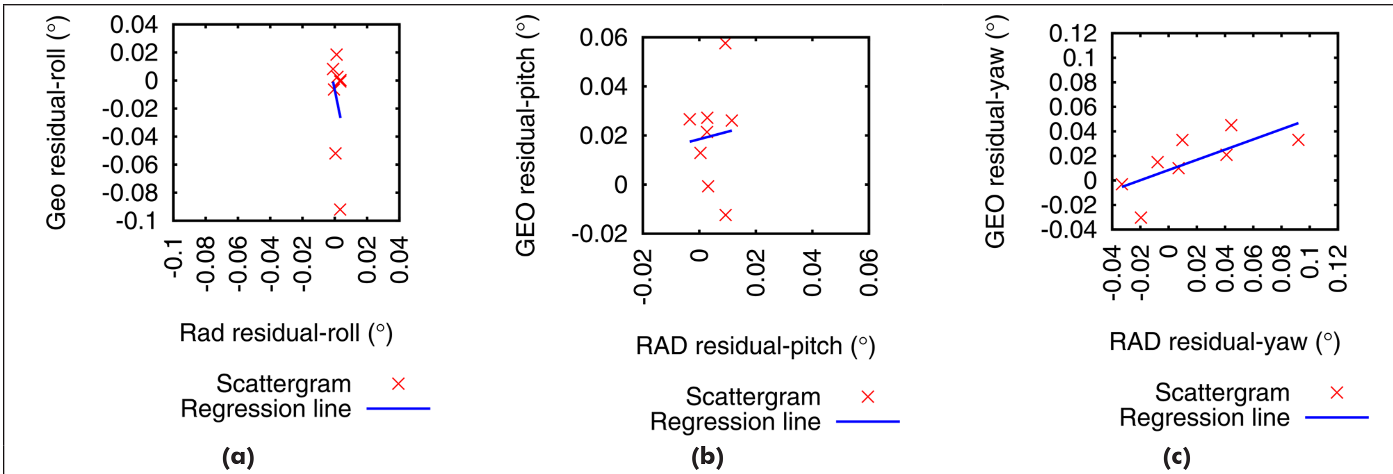

Figure 13. Comparison of GEO and RAD residuals using the old approach. GEO = geometrically corrected; RAD = radiometrically corrected. (a) GEO and RAD residual roll. (b) GEO and RAD residual pitch. (c) GEO and RAD residual yaw.

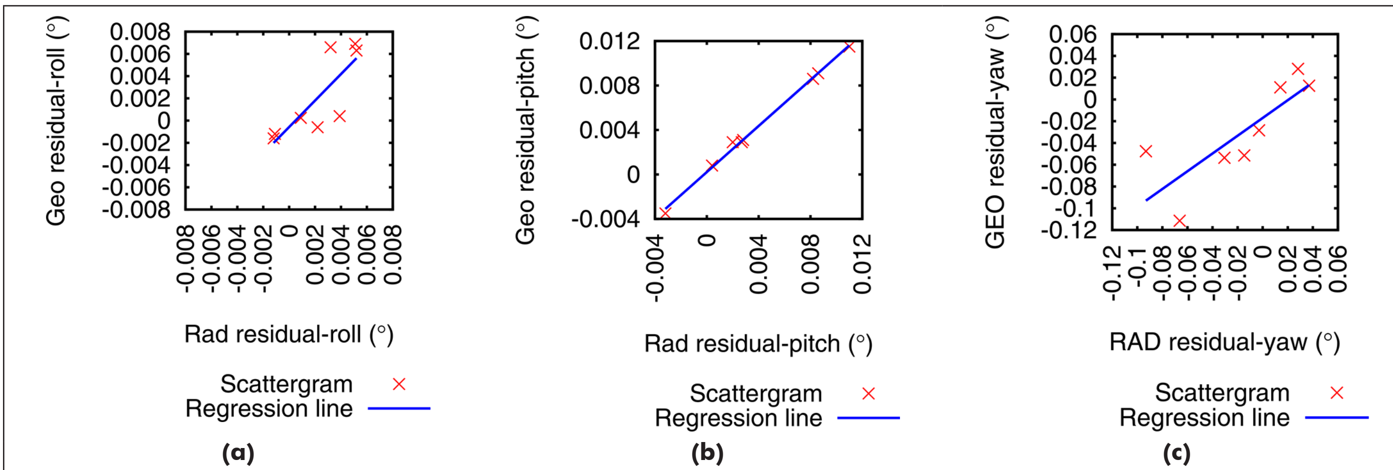

Figure 14. Comparison of GEO and RAD residuals using the proposed approach. GEO = geometrically corrected; RAD = radiometrically corrected. (a) GEO and RAD residual roll. (b) GEO and RAD residual pitch. (c) GEO and RAD residual yaw.

Table 6. Slope, offset, and R^2 comparison between estimates using the old and proposed approaches.

	Old Approach			Proposed Approach		
Rotation	**Slope**	**Offset**	**R^2**	**Slope**	**Offset**	**R^2**
Roll	−5.63	0.01	0.074	1.18	0.00	0.65
Pitch	0.30	0.02	0.005	1.03	0.00	0.99
Yaw	0.41	0.01	0.50	0.82	0.02	0.65

established. A procedure for estimating the GEO-to-RAD rotation angle as a function of latitude based on orbit geometry is presented.
2. The proposed technique is demonstrated on GEO products of *Cartosat-2S*, and it is established that after application of the attitude biases, location error declines significantly. Further, the validation of our results is carried out by estimating the residual attitude for corresponding RAD products using our previous approach (Dubey and Kartikeyan 2018).
3. The results obtained by our approach are further compared with those of other approaches to residual attitude estimation in the literature (Pulsule *et al.* 2008). The R^2 estimates for residual roll, pitch, and yaw are 0.074, 0.005, and 0.50, respectively, using the old method, and 0.65, 0.99, and 0.65 using the proposed method.

The novelty of the proposed technique lies in the fact that it directly deals with widely available GEO (level 2) products for estimating residual attitude, which so far in the literature is investigated using only RAD (level 1) products. We feel that our proposed technique not only enriches our knowledge about residual attitude estimation but also is simple to implement in operational practice. Overall, the proposed technique has high accuracy and provides higher reliability than the existing methods.

Acknowledgments

The authors thank the director of the Space Applications Centre, Ahmedabad, and the group director of the Signal and Image Processing Group for encouragement and support in this work. We acknowledge the support of the High Resolution Data Processing Division for providing the RAD and GEO data products used in this article. Support from the team members of the Image Analysis and Quality Evaluation Division is gratefully acknowledged.

References

Anuta, P. E. 1973. *Geometric Correction of ERTS-1 Digital Multispectral Scanner Data. LARS Information Note 103073.* West Lafayette, Ind.: Laboratory for Applications of Remote Sensing, Purdue University.

Cao, H., P. Tao, H. Li and J. Shi. 2019. Bundle adjustment of satellite images based on an equivalent geometric sensor model with digital elevation model. *ISPRS Journal of Photogrammetry and Remote Sensing* 156:169–183.

Chen, Y., Z. Qiu, Z. Xie, Y. Le and S. Fang. 2017. Detection of attitude constant error and in-orbit calibration for the three-line CCD sensor of the ZY-3 satellite. *International Journal of Remote Sensing* 38(23):7333–7356.

Crassidis, J. L., F. L. Markley and Y. Cheng. 2007. Survey of nonlinear attitude estimation methods. *Journal of Guidance, Control, and Dynamics* 30(1):12–28.

Davison, G. J. 1986. Ground control pointing and geometric transformation of satellite imagery. *International Journal of Remote Sensing* 7(1):65–74.

Dubey, B. and B. Kartikeyan. 2018. A novel approach for estimation of residual attitude of a remote sensing satellite. *International Journal of Remote Sensing* 39(22):8219–8245.

Dubey, B., B. Kartikeyan and M. M. Subbiah. 2019. Rational polynomial coefficients modeling and bias correction by using iterative polynomial augmentation. *Journal of the Indian Society of Remote Sensing* 47:165–175.

Ford, G. E. and C. I. Zanelli. 1985. Analysis and quantification of errors in the geometric correction of satellite images. *Photogrammetric Engineering and Remote Sensing* 51(11):1725–1734.

Grassi, M. 1997. Attitude determination and control for a small remote sensing satellite. *Acta Astronautica* 40(9):675–681.

Jiang, Y., G. Zhang, L. Li, Z. Tan, Z. Tang and Y. Xu. 2022. A novel inverse transformation algorithm for pushbroom TDI CCD imaging. *International Journal of Remote Sensing* 43(3):1074–1090.

Leprince, S., S. Barbot, F. Ayoub and J. Avouac. 2007. Automatic and precise orthorectification, coregistration, and subpixel correlation of satellite images, application to ground deformation measurements. *IEEE Transactions on Geoscience and Remote Sensing* 45(6):1529–1558.

Mahapatra, A., R. Ramchandran and R. Krishnan. 2004. Modeling the uncertainty in orientation of IRS-1C/1D with a rigorous photogrammetric model. *Photogrammetric Engineering and Remote Sensing* 70(8):939–946.

Pan, H., Z. Zou, G. Zhang, X. Zhu and X. Tang. 2016. A penalized spline-based attitude model for high resolution satellite imagery. *IEEE Transactions on Geoscience and Remote Sensing* 54(3):1849–1859.

Pulsule, S. S., B. Shah, G. Paswan, A. Sharma, A. Garg, H. Pandya, S. S. Srivastava and S. Roy. 2008. Resourcesat-1 data quality evaluation system. *International Journal of Applied Earth Observation and Geoinformation* 10:147–158.

Radhadevi, P. V., R. Müller, P. d'Angelo and P. Reinartz. 2011. In-flight geometric calibration and orientation of ALOS/PRISM imagery with a generic sensor model. *Photogrammetric Engineering and Remote Sensing* 77(5):531–538.

Radhadevi, P. V. and S. S. Solanki. 2008. In-flight geometric calibration of different cameras of IRS-P6 using a physical sensor model. *The Photogrammetric Record* 23(121):69–89.

Ruszczyński, A. 2006. *Nonlinear Optimization*, 3d ed. Princeton, N.J.: Princeton University Press.

Shen, X., B. Liu and Q.-Q. Li. 2017. Correcting bias in the rational polynomial coefficients of satellite imagery using thin-plate smoothing splines. *ISPRS Journal of Photogrammetry and Remote Sensing* 125:125–131.

Soken, H. E., C. Hajiyev and S.-i. Sakai. 2014. Robust Kalman filtering for small satellite attitude estimation in the presence of measurement faults. *European Journal of Control* 20(2):64–72.

Srinivasan, T. P., B. Islam, S. K. Singh, B. G. Krishna and P. K. Srivastava. 2008. In-flight geometric calibration—an experience with Cartosat-1 and Cartosat-2. *The International Archives of the Photogrammetry, Remote Sensing and Spatial Information Sciences* 37(B1):83–88.

Srivastava, P. K. and M. S. Alurkar. 1997. Inflight calibration of IRS-1C imaging geometry for data products. *ISPRS Journal of Photogrammetry and Remote Sensing* 52:215–221.

Tommaselli, A. M. G. and C. L. Tozzi. 1996. A recursive approach to space resection using straight lines. *Photogrammetric Engineering and Remote Sensing* 62(1):57–66.

Wahba, G. 1965. A least squares estimate of satellite attitude. *SIAM Review* 7(3):409.

Wang, M., Y. Cheng, X. Chang, S. Jin and Y. Zhu. 2017. On-orbit geometric calibration and geometric quality assessment for the high-resolution geostationary optical satellite GaoFen4. *ISPRS Journal of Photogrammetry and Remote Sensing* 125:63–77.

Weser, T., F. Rottensteiner, J. Willneff, J. Poon and C. S. Fraser. 2008. Development and testing of a generic sensor model for pushbroom satellite imagery. *The Photogrammetric Record* 23(123):255–274.

Westin, T. 1992. Interior orientation of SPOT imagery. *International Archives of Photogrammetry and Remote Sensing* 29:193–198.

Xiong, Z. and Y. Zhang. 2009. A generic method for RPC refinement using ground control information. *Photogrammetric Engineering and Remote Sensing* 79(9):1083–1092.

Yang, Z., X. Zhu, Z. Cai, W. Chen and J. Yu. 2021. A real-time calibration method for the systematic errors of a star sensor and gyroscope units based on the payload multiplexed. *Optik* 225:165731.

Zhang, G., Y. Jiang, D. Li, W. Huang, H. Pan, X. Tang and X. Zhu. 2014. In-orbit geometric calibration and validation of ZY-3 linear array sensors. *The Photogrammetric Record* 29(145):68–88.

UNITED STATES POSTAL SERVICE® Statement of Ownership, Management, and Circulation (All Periodicals Publications Except Requester Publications)

1. Publication Title	2. Publication Number	3. Filing Date
Photogrammetric Engineering & Remote Sensing	0 4 3 0 – 9 6 0	
4. Issue Frequency	**5. Number of Issues Published Annually**	**6. Annual Subscription Price**
Monthly	12	$1105.00

7. Complete Mailing Address of Known Office of Publication *(Not printer) (Street, city, county, state, and ZIP+4®)*
ASPRS
425 Barlow Place, Suite 210
Bethesda, MD 20814

Contact Person
Rae Kelley

Telephone *(Include area code)*
301-493-0290

8. Complete Mailing Address of Headquarters or General Business Office of Publisher *(Not printer)*
Same as block #7

9. Full Names and Complete Mailing Addresses of Publisher, Editor, and Managing Editor *(Do not leave blank)*

Publisher *(Name and complete mailing address)*
ASPRS
425 Barlow Place, Suite 201
Bethesda, MD 20814

Editor *(Name and complete mailing address)*
Dr. Alper Yilmaz
470 Hitchcock Hall
Columbus, OH 43035

Managing Editor *(Name and complete mailing address)*
Rae Kelley, ASPRS
425 Barlow Place, Suite 201
Bethesda, MD 20814

10. Owner *(Do not leave blank. If the publication is owned by a corporation, give the name and address of the corporation immediately followed by the names and addresses of all stockholders owning or holding 1 percent or more of the total amount of stock. If not owned by a corporation, give the names and addresses of the individual owners. If owned by a partnership or other unincorporated firm, give its name and address as well as those of each individual owner. If the publication is published by a nonprofit organization, give its name and address.)*

Full Name	Complete Mailing Address
American Society for Photogrammetry and Remote Sensing	Same as block #7

11. Known Bondholders, Mortgagees, and Other Security Holders Owning or Holding 1 Percent or More of Total Amount of Bonds, Mortgages, or Other Securities. If none, check box → ☒ None

Full Name	Complete Mailing Address

12. Tax Status *(For completion by nonprofit organizations authorized to mail at nonprofit rates) (Check one)*
The purpose, function, and nonprofit status of this organization and the exempt status for federal income tax purposes:
☒ Has Not Changed During Preceding 12 Months
☐ Has Changed During Preceding 12 Months *(Publisher must submit explanation of change with this statement)*

PS Form **3526,** July 2014 *[Page 1 of 4 (see instructions page 4)]* PSN: 7530-01-000-9931 **PRIVACY NOTICE:** See our privacy policy on *www.usps.com.*

13. Publication Title	14. Issue Date for Circulation Data Below	
Photogrammetric Engineering & Remote Sensing	October 2022	
15. Extent and Nature of Circulation	**Average No. Copies Each Issue During Preceding 12 Months**	**No. Copies of Single Issue Published Nearest to Filing Date**
a. Total Number of Copies *(Net press run)*	350	303
b. Paid Circulation *(By Mail and Outside the Mail)* (1) Mailed Outside-County Paid Subscriptions Stated on PS Form 3541 (Include paid distribution above nominal rate, advertiser's proof copies, and exchange copies)	152	150
(2) Mailed In-County Paid Subscriptions Stated on PS Form 3541 *(Include paid distribution above nominal rate, advertiser's proof copies, and exchange copies)*	0	0
(3) Paid Distribution Outside the Mails Including Sales Through Dealers and Carriers, Street Vendors, Counter Sales, and Other Paid Distribution Outside USPS®	63	0
(4) Paid Distribution by Other Classes of Mail Through the USPS (e.g., First-Class Mail®)	55	54
c. Total Paid Distribution *[Sum of 15b (1), (2), (3), and (4)]*	270	204
d. Free or Nominal Rate Distribution *(By Mail and Outside the Mail)* (1) Free or Nominal Rate Outside-County Copies included on PS Form 3541	0	0
(2) Free or Nominal Rate In-County Copies Included on PS Form 3541	0	0
(3) Free or Nominal Rate Copies Mailed at Other Classes Through the USPS (e.g., First-Class Mail)	0	0
(4) Free or Nominal Rate Distribution Outside the Mail *(Carriers or other means)*	15	15
e. Total Free or Nominal Rate Distribution *(Sum of 15d (1), (2), (3) and (4))*	15	15
f. Total Distribution *(Sum of 15c and 15e)*	285	219
g. Copies not Distributed *(See Instructions to Publishers #4 (page #3))*	80	99
h. Total *(Sum of 15f and g)*	365	318
i. Percent Paid *(15c divided by 15f times 100)*	94.73	93.15

* If you are claiming electronic copies, go to line 16 on page 3. If you are not claiming electronic copies, skip to line 17 on page 3.

PS Form **3526,** July 2014 *(Page 2 of 4)*

UNITED STATES POSTAL SERVICE® Statement of Ownership, Management, and Circulation (All Periodicals Publications Except Requester Publications)

16. Electronic Copy Circulation	Average No. Copies Each Issue During Preceding 12 Months	No. Copies of Single Issue Published Nearest to Filing Date
a. Paid Electronic Copies	122	125
b. Total Paid Print Copies (Line 15c) + Paid Electronic Copies (Line 16a)	392	329
c. Total Print Distribution (Line 15f) + Paid Electronic Copies (Line 16a)	407	344
d. Percent Paid (Both Print & Electronic Copies) (16b divided by 16c × 100)	96.31	95.64

☒ **I certify that 50% of all my distributed copies (electronic and print) are paid above a nominal price.**

17. Publication of Statement of Ownership

☒ If the publication is a general publication, publication of this statement is required. Will be printed in the October 2022 issue of this publication. ☐ Publication not required.

18. Signature and Title of Editor, Publisher, Business Manager, or Owner
Rae Kelley

Date
9/9/2022

I certify that all information furnished on this form is true and complete. I understand that anyone who furnishes false or misleading information on this form or who omits material or information requested on the form may be subject to criminal sanctions (including fines and imprisonment) and/or civil sanctions (including civil penalties).

PS Form **3526,** July 2014 *(Page 3 of 4)* **PRIVACY NOTICE:** See our privacy policy on *www.usps.com.*

Efficient Building Inventory Extraction from Satellite Imagery for Megacities

Edmond Yat-Man Lo, En-Kai Lin, Velautham Daksiya, Kuo-Shih Shao, Yi-Rung Chuang, and Tso-Chien Pan

Abstract

Accurate building inventories are essential for city planning and disaster risk management. Traditionally generated via census or selected small surveys, these suffer from data quality and/or resolution. High-resolution satellite imagery with object segmentation provides an effective alternative, readily capturing large extents. This study develops a highly automated building extraction methodology for location-based building exposure data from high (0.5 m) resolution satellite stereo imagery. The development relied on Taipei test areas covering 13.5 km² before application to the megacity of Jakarta. Of the captured Taipei buildings, 48.8% are at one-to-one extraction, improving to 71.9% for larger buildings with total floor area >8000 m², and to 99% when tightly-spaced building clusters are further included. Mean absolute error in extracted footprint area is 16% for these larger buildings. The extraction parameters are tuned for Jakarta buildings using small test areas before covering Jakarta's 643 km² with over 1.247 million buildings extracted.

Introduction

The international disaster event database NatCatSERVICE (2019) reported USD $150 billion economic loss worldwide for the year 2018, arising from 820 natural hazard events, of which Asia accounts for 50%. Reliable estimates of the potential losses need to be developed to support effective risk management of such loss events, particularly those occurring in cities/megacities with consequent large socio-economic impacts. This in turn requires accurate descriptions of the exposures along with the hazard levels faced (Grossi et al. 2005). Such exposure data typically requires spatial maps on assets (e.g., buildings and infrastructures) at risk of covering their location, size, and other characteristics such as vulnerability, as depending on the hazard faced. Exposure maps for individual building location, height, and footprint area, and spanning the entire building inventory are needed for overlaying with hazard event maps in detailed loss assessment such as for floods and earthquakes, the two largest perils by loss magnitude for Asia (NatCatSERVICE 2019). However, such data in Asia and Southeast Asia is generally poor in quality, accessibility, and availability.

A detailed estimation of building inventory traditionally uses census data, conducting of surveys, and/or manual processing of satellite/aerial images. While rich in details at an individual building level, these are often expensive and time consuming processes, implying by necessity either coarseness in spatial resolution or in overall coverage (Figueiredo and Martina 2016; Silva et al. 2015). Automatic building footprint (BFT) extraction from high-resolution satellite and aerial imageries are attractive alternatives in terms of data availability, acquisition cost, and the ability to cover large geographical extents (De Angeli et al. 2016; Gunasekera et al. 2015). However, challenges arise from the close proximity of buildings in dense cities, the diversity of building forms, and the level of differentiation from other background objects (Li et al. 2019). Different approaches are reported (Chen et al. 2018; Gavankar and Ghosh 2018; Li et al. 2019; Ok 2013; Huang and Zhang 2012), with multi-resolution segmentation being the most widely used (Belgiu and Drăguţ 2014; Im et al. 2014). More recent studies involve deep learning applied to semantic segmentation algorithms (Lu et al. 2018; Xu et al. 2018; Sun et al. 2018; Im et al. 2014), though a large scale, city-wide application has yet to be reported.

Besides BFT, building height along with spatial location are also needed for building exposure development. Use of aerial imagery and lidar from low-flying aircraft and/or UAVs for generating Digital Surface Models (DSM) and extracting BFT and height have been reported (Haithcoat et al. 2001; Sahar et al. 2010; Awrangjeb et al. 2010; Yuan 2018; Lu et al. 2018; Xu et al. 2018; Sun et al. 2018). While such imagery offers increased resolution, there are inherent difficulties in securing permission to fly over dense, urban areas. It should also be noted that global commercial technology companies, e.g., Google have developed in-house, proprietary algorithms for extracting BFTs and heights from aerial imagery. There have also been recent, major advances in computer vision, and particularly in image segmentation using Deep Learning (DL) techniques (recent reviews are given in Garcia-Garcia et al. (2017) and Minaee et al. (2021)) applied to deep neural networks (DNN) (the most popular being convolution neural networks). Applications are reported for object detection and classification in both urban and nonurban settings (e.g., Zhang and Zhang 2018; Maltezos et al. 2019; Zhang et al. 2019). The specific works for building classification in urban areas are predominantly based on images from low flying platforms such as airborne laser scanning (ALS) or lidar (Maltezos et al. 2019) or multi-view images (Yu et al. 2021). Building footprint delineation over large areas (Wei et al. 2020) and building reconstruction at Level-of-Detail 1 (LoD-1) for small areas (Zhang and Zhang 2018; Yu et al. 2021) has been reported. Most recently (Gui and Qin 2021) applied DL techniques on very high resolution multi-view satellite images (0.3 to 0.5 m ground sampling distances) and orthophotos to achieve up to LoD-2 level of building reconstruction as demonstrated for small areas (0.5 to 2.25 km²) in three cities. Optional incorporation of the public OpenStreetMap building data further enabled refinement in building orientation. Although DL techniques and DNN have exhibited excellent capability for building extraction and reconstruction, its performance is highly correlated with the size and diversity of labelled training data as appropriate for the city scene. Therefore, building footprint and height reconstruction in complex, diverse, and dense city scenes using DNN remains an active area of research with a variety of data types (e.g., ALS, lidar, multispectral), pre- and post-processing strategies (e.g., Gui and Qin 2021), footprint regularization techniques (e.g., Wei et al. 2020), and fusion of networks (e.g., Bittner et al. 2018)

Edmond Yat-Man Lo, Velautham Daksiya, and Tso-Chien Pan are with the Institute of Catastrophe Risk Management, Nanyang Technological University, Block N1, Level B1b, 50 Nanyang Ave, Singapore 639798 (cymlo@ntu.edu.sg).

Edmond Yat-Man Lo and Tso-Chien Pan are also with the School of Civil and Environmental Engineering, Nanyang Technological University, Block N1, 50 Nanyang Ave, Singapore 639798.

En-Kai Lin, Kuo-Shih Shao, and Yi-Rung Chuang are with Sinotech Engineering Consultants, Inc., No. 171, Sec 5, Nanking E. Rd., Taipei City, Taiwan.

Contributed by Zhenfeng Shao, August 23, 2021 (sent for review April 26, 2022; reviewed by Nan Yang, Min Chen).

Photogrammetric Engineering & Remote Sensing
Vol. 88, No. 10, October 2022, pp. 643–652.
0099-1112/22/643–652

doi: 10.14358/PERS.21-00053R2

proposed, with building footprint and height extraction at whole-city scale yet to be demonstrated. An accuracy-quantified, low-cost, highly-automated, and scalable methodology using readily available high-resolution satellite imagery for extracting location based BFTs and heights as demonstrated here for a megacity have yet to be reported.

In the work here, an efficient, scalable BFT and height extraction methodology is developed and piloted over a 27.9 km^2 area in Taipei, Taiwan and further applied to cover the entire megacity of Jakarta, Indonesia covering an area of 643 km^2. The recently developed rational polynomial coefficient (RPC) stereo processor (RSP) (Qin 2016) for DSM generation, and the commercial *eCognition* software (http://www.ecognition.com/) for image segmentation are applied on high (0.5 m pixel) resolution satellite stereo imagery. Over 1.247 million buildings in Jakarta are extracted. It is further shown that only a small fraction of the extracted BFT require manual adjustment, typically larger buildings as comprising less than 10% of the total building count. This represents huge cost and time savings over traditional methods.

The study areas in Taipei and Jakarta along with data used are presented in the section "Study Areas and Data". A description of the BFT extraction methodology and performance evaluation are in sections "Building Footprint and Height Extraction" and "Performance Evaluation". Results from the Taipei pilot area are presented in the section "Taipei Test Areas", while the application to Jakarta presented in the section "Jakarta City", followed by the Conclusion section.

Study Areas and Data

The Taipei 27.9 km^2 pilot area is located in downtown Taipei (Figure 1a), which spans various building types, including residential, commercial, and public buildings. Two test areas comprising 13.52 km^2 within the pilot area are used for building extraction methodology development and validation. These two test areas represented different building characteristics, with the first test area of 8.43 km^2 being in a newer part of the city, while the second area of 5.09 km^2 is in an older part. The test areas include modern, low- to high-rise buildings, and important landmarks, such as the Taipei Train Station and the supertall 101-storey Taipei 101. Parameters in the developed building extraction methodology are tuned for Jakarta's building using Jakarta's two test areas comprising 9.80 km^2 (Figure 1b), before being applied to the whole city covering 643 km^2. The tuning is needed due to the different building characteristics between Taipei and Jakarta. Jakarta's test areas are chosen from Central (Pusat) Jakarta that covers a variety of residential, commercial, and public buildings, and from north (Utara) Jakarta to further cover industrial buildings. The tallest building included is the 47-storey Menara Astra.

Taipei vector data (TVD) developed by Taipei city government in 2010 is available for both Taipei test areas and served as highly accurate ground reference data for accuracy assessment. The TVD is constructed via stereo-plotting of aerial stereo photos, and is continually updated by Sinotech Engineering Consultants Inc. The data contains detailed (1/1000 scale) boundaries of surface structures including building rooftops in vector format and rooftop height values. Figure 2 (upper panels) show histograms of the 13,208 TVD buildings' BFT areas and heights over the test areas. Only footprint areas >50 m^2 are considered, as Taipei government regulations deem land plots ≤67 m^2 as nonbuildable. The first and second test areas have 6745 and 6459 buildings, respectively, with most having BFT areas ≤2000 m^2.

Similar ground reference data did not exist for Jakarta. Therefore, satellite images are manually stereo-plotted to extract accurate individual building BFT and height for use as ground reference data. The accuracy of the manual extraction was confirmed by two independent polygon extractions done on a small subset of 114 buildings (BFT areas up to 4200 m^2) with the mean absolute difference in extracted BFT areas being <5%. The ground reference set has 11,626 buildings with BFT areas mostly ≤2000 m^2 as in Taipei but with the peak shifted to smaller BFT values (Figure 2, lower panels). Most of the buildings are also lower, ≤3 stories.

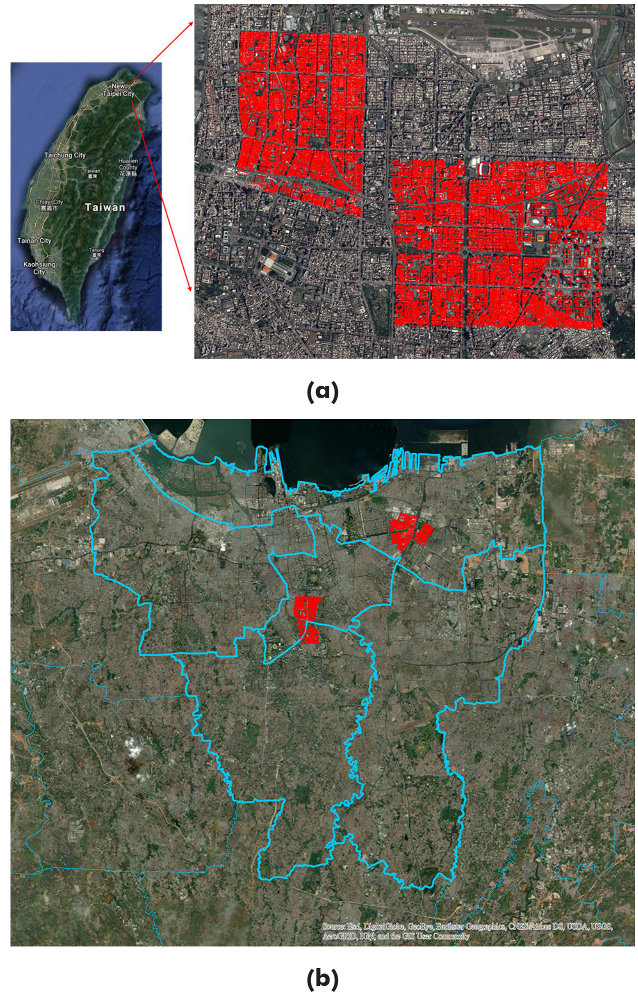

Figure 1. Study areas comprising (a) Taipei pilot area and (b) Jakarta city with its five regions. Test areas are indicated in red.

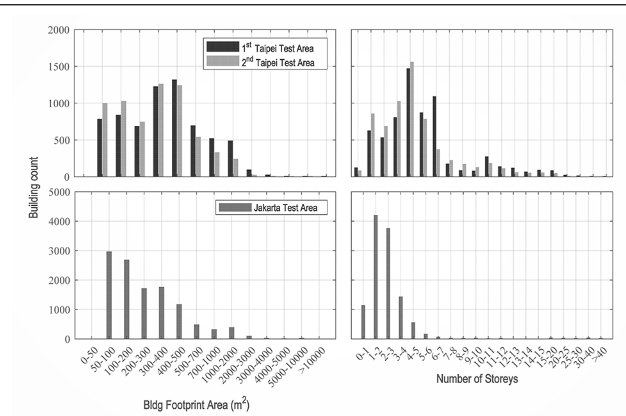

Figure 2. Distribution of building footprint (BFT) area and building height in ground reference data for test areas of Taipei (upper panels) and Jakarta (lower panels). An inter-story height of 3.45 m was used to covert height values to stories.

Regarding sources of satellite stereo images, images from WorldView series, *GeoEye-1*, *QuickBird*, *Pleiades 1A/1B* series, *KOMPSAT-3A/3A*, *CARTOSAT*, and *DMC3*/Triple Sat were evaluated for suitability. The *Pleiades 1A/1B* series were chosen as it allowed tight stereo angle specifications, providing ortho-rectified color data at 0.5 m resolution with high revisit interval of ~two days over Southeast

Asia. A tight stereo angle control was needed to capture tall buildings, while a high revisit rate allowed for cloud/mist free images even in wet, tropical regions, such as that for Jakarta. However, it should be noted that with the rapid advances in commercial satellite imaging, other satellite imagery that meet or exceed these requirements can equally be used.

Building Footprint and Height Extraction

Figure 3 shows a schematic of the BFT extraction methodology. A high degree of automation was achieved via use of RSP, *eCognition* and Geographical Information System (GIS) software, augmented with internally developed software. For DSM generation, the recently available RSP software shown to be particularly suited for use with large scale satellite stereo images (Qin 2016), and the more conventional SOCET GXP (GXP) are assessed with improved results using RSP obtained. In particular, DSM generation in RSP was performed by applying aerial triangulation, referring to ground control points and image matching.

The BFT shape extraction comprise automated segmentation with edge regularization along with a manual adjustment on a small percentage of extracted polygons (Figure 3). The segmentation and regularization procedures followed that of Kuo et al. (2018) and Su et al. (2015). Segmentation was applied only on preprocessed, built-up areas with roads and vegetation surfaces removed. Road surfaces were defined using road vectors from Open Street Map (OSM), with a road buffer width ranging from 1 m (small alleys) to 60 m (arterial road) applied as depending on the road type. Vegetation areas were classified using a Normalized Difference Vegetation Index (NDVI) (Huete et al. 2002), which is a normalized ratio of near infrared (IR) and red bands. Here a calibrated cut-off NDVI value of 0.25 was applied. The *eCognition* software was used for image segmentation on an Object Height Model (OHM), being the difference between DSM and DEM, for high-rise building, and on ortho-rectified images for low-rise buildings, following the segmentation algorithm of Baatz and Schäpe (2000). The first segmentation was exercised on an edge-preserving Kuwahara filtered (sharpened) OHM covering the built-up area following a

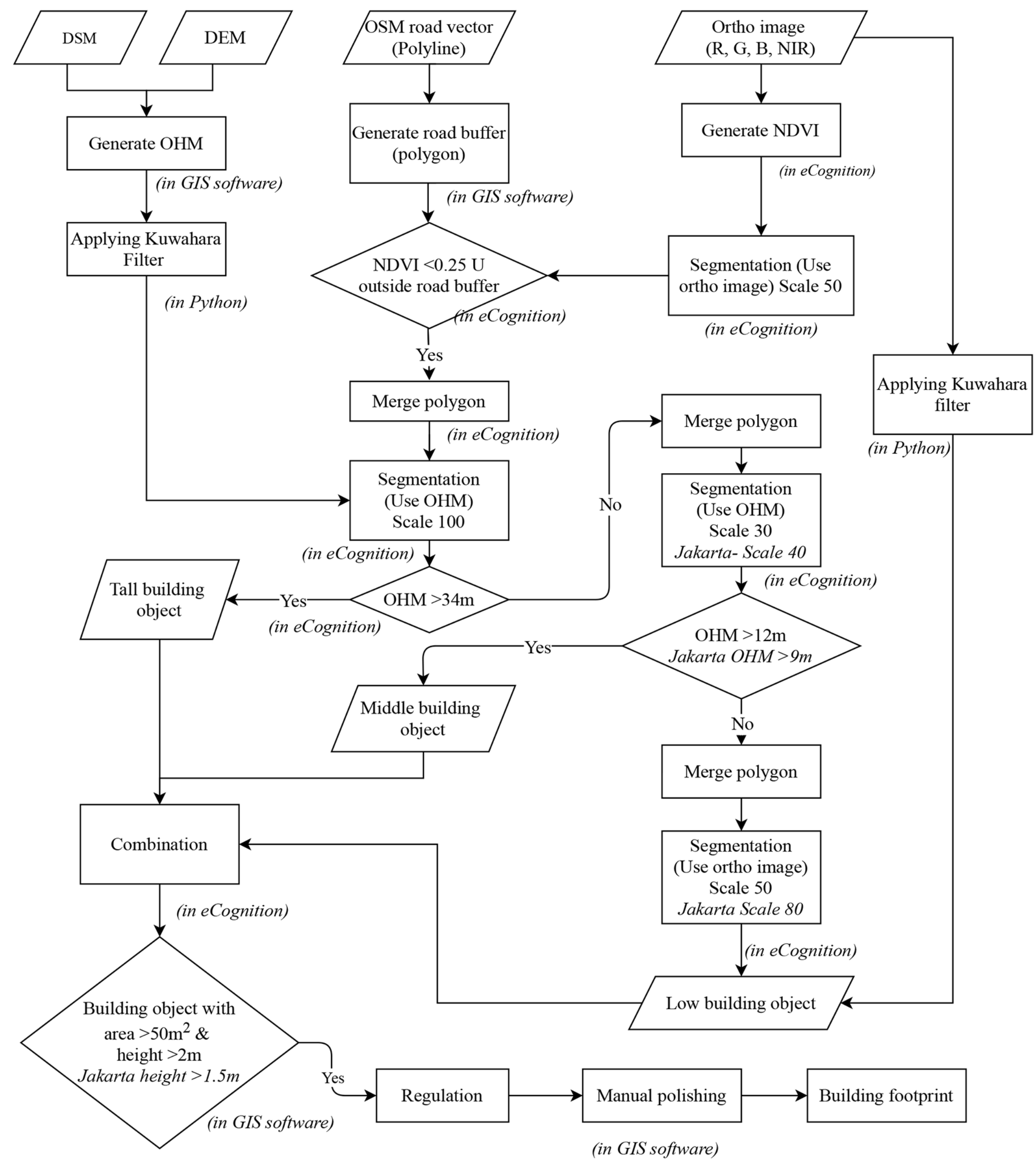

Figure 3. Building footprint (BFT) shape and height extraction methodology flow chart. Parameters, unless separately indicated for Jakarta, are same for Taipei and Jakarta.

building categorization based elevation values (see Figure 3). Regions with high elevations corresponded to larger building objects, which necessitated a larger scale parameter. For low elevation buildings, use of OHM consistently produced over-segmentation with many small objects identified. Rather segmentation on ortho-rectified color images produced satisfactory results for the low elevation buildings. Since the segmentation was based roof top elevations (high- and mid-elevation regions) and roof top features (low elevation region), the segmented objects were found to be sensitive to smaller roof top structures such as lift shafts, water tanks, or in the case of low residential buildings, small (often illegal) roof top additions. As these roof top features did not signify distinct buildings, adjacent polygons in mid- and low-elevation regions are merged if the height difference is less than 1.5 m. Polygons with BFT area ≤50 m^2 (nonbuildable land lots) or height ≤2 m (i.e., nonbuilding objects of low height) were also removed.

The regularization step following Kuo et al. (2018) is to partially correct for jagged lines in the segmented polygon shapes, removing/merging small, extraneous extracted polygons, and straightening of polygon edges. In dense urban areas such as Taipei and Jakarta, many buildings are connected to each other and edges between such adjacent buildings would share the same geometry. These shared edges were simplified and regularized simultaneously to retain the shared edge. A small percentage of the polygons required manual adjustment on footprints by cross-comparison with Google maps and Google Streetview. Manual polishing is conducted on larger size buildings as defined by total floor area (TFA) being ≥8000 m^2 for Taipei and ≥2500 m^2 for Jakarta. This comprised less than 10% total number of buildings and indeed this 10% value was used as a guide in setting the TFA cutoff values for the city-specific larger buildings and thus, the manual effort required. After BFT shape extraction, building height was determined by averaging the OHM values within the extracted polygon shape with allowance of a boundary buffer and removal of outliers. In setting the TFA, an inter-story height of 3.45 m representing an average story height (residential 3.3 m and commercial 3.6 m) in Taipei and Jakarta is used for converting extracted building height to number of stories, which when multiplied by the BFT area gives the TFA.

The extraction methodology development involved a trial-and-error process as guided by a comparison of the extracted building polygons with the ground reference TVD data from Taipei first test area and using Taipei second test area as verification. The parameters of the extraction methodology are expected to have values for Jakarta different from Taipei's due to their different building characteristics (see Figure 2). These are tuned as guided by results from the Jakarta test areas. The notable differences are: <9 m building height is defined as low rise buildings in Jakarta while <12 m is used for Taipei. The segmentation scale for middle and low rise are, respectively, 40 and 80 for Jakarta, while they are 30 and 50 for Taipei. All processing unless otherwise indicated, are done within an ArcGIS environment. The most time intensive step is in the manual polishing performed on the small number of large, extracted building polygons. This required a modest 40 man-weeks (four summer interns were deployed) to cover whole Jakarta spanning 643 km^2.

Performance Evaluation

The detected building polygon areas are first assessed for an overall building area detection performance via standard metrics of True Positive/Negative (TP/TN) and False Positive/Negative (FP/FN). Here TP/TN denote areas correctly classified as spanning buildings/non-building areas, FP denotes area incorrectly classified as building area, and FN as area incorrectly classified as nonbuilding area. From these, quality metrics of quality percentage (QP), detection rate (DR), and overall accuracy (OA) are computed. QP accounts for both boundary delineation accuracy and building detection rate, DR denotes the percentage building area correctly detected, and OA the percentage of building and non-building areas correctly detected.

$$QP = \frac{TP}{TP + FP + FN}; DR = \frac{TP}{TP + FN}; OA = \frac{TP + TN}{TP + TN + FP + FN} \quad (1)$$

However, beyond such metrics on overall building area being accurately detected, the individually extracted buildings (or polygons) do not necessarily have one-to-one match with the actual, with a common challenge of closely spaced buildings being extracted as one building in dense urban settings. This necessitated a more detailed object-level accuracy assessment, as achieved here by categorizing the extracted polygons into five cases below:

- Case 1 (extraneous): An extraneous polygon when the centroid of the extracted polygon does not fall within the boundary of any ground reference polygon.
- Case 2 (one-to-one): One-to-one (desired) match between an extracted polygon and a ground reference polygon. Here the centroids of extracted polygon and ground reference polygon fall within the boundaries of each other.
- Case 3 (one-to-many): The extracted polygon enclosed several ground reference polygons as defined by the centroids of the ground reference polygons falling within the boundary of the extracted polygon.
- Case 4 (many-to-one): Multiple polygons are extracted from one single ground reference polygon, and the boundary of the ground reference polygon encompasses the centroids of several extracted polygons.
- Case 5 (missed): Polygon missed in extraction.

Case 3 occurs when a cluster of tightly spaced ground reference buildings of similar height and inseparable from aerial views are grouped together in the extracted polygon (see Figure 4a). This often happens in dense urban settings with a prevalence of rows of tightly-spaced, inseparable buildings. Case 4 corresponds to buildings with complex roof top configurations or features resulting in multiple polygons being extracted within a single ground reference polygon (Figure 4b). As such, a count accuracy analysis across the five cases is first performed before an accuracy evaluation on the values of extracted BFT area and height. The analysis is performed separately for Taipei first test area (used for methodology development, i.e., a calibration) and tested independently over the second test area (i.e., a verification).

Results and Discussion

DSM generation using RSP and the more conventional GXP were first quantitatively compared for the Taipei test areas. Building rooftop elevations from TVD (subset of 125 buildings) are used to determine convergence angle requirements in the satellite stereo imagery needed for capturing tall buildings. The 125 TVD elevation values ranged up to 174 m, with a further value at 391 m corresponding to the super tall Taipei 101. Building rooftop elevation values calculated using RSP are more accurate than using GXP with regions of higher elevation having better delineation. Over 92% of the 125 buildings have elevation error <3 m at 14° convergence angle, this improving to 94% at 10°. The sole exception is Taipei 101, where RSP significantly underestimated and GXP even more so. The subsequent images used below for Jakarta are at 12° convergence angle. For OHM generation, a DEM was derived by sampling the RSP generated DSM ground points in free space such as parks and roads. A total of 432 ground points within and around the Taipei test areas are interpolated for DEM generation.

Figure 5 shows the extracted BFT polygons for the Taipei and Jakarta test areas. QP, DR, and OA values for Taipei first test area are 71.4%, 83.9%, and 87.5%, respectively, and 73.6%, 85.6%, and 86.8%, respectively, for the second test area. These values are within reported ranges for building detection applications from satellite imagery (Hermosilla et al. 2011; Ghandour and Jezzini 2018; Jin and Davis 2005; Lee et al. 2003), though higher ranges are reported by Khoshelham et al. (2010) who used multi-source (including lidar) data. The QP, DR, and OA values are 79.3%, 88.3%, and 91.4%, for the Jakarta test areas, slightly better than Taipei's.

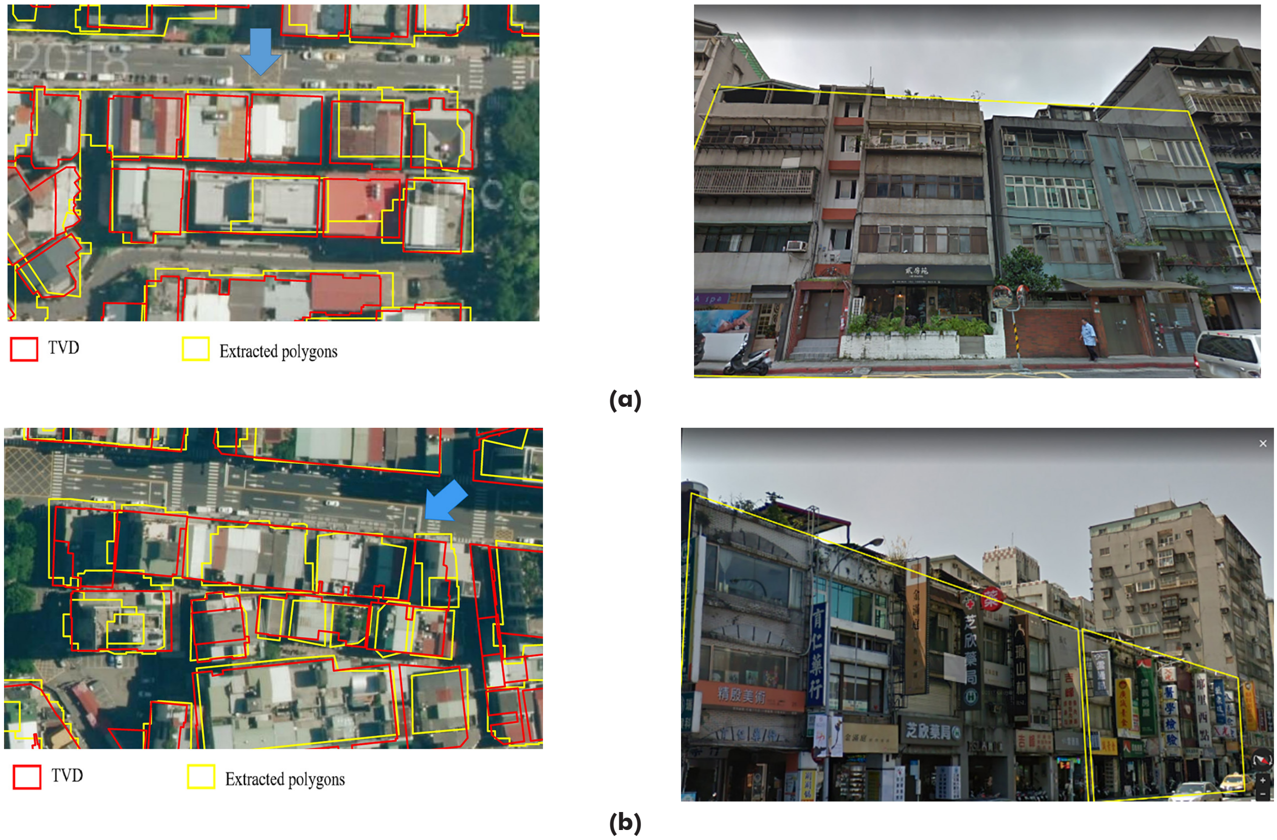

Figure 4. Buildings categorized as (a) Case 3: unseparated buildings due to small separation and small difference in roof height and (b) Case 4: over-segmented due to various rooftop structures. Examples shown are from Taipei test areas.

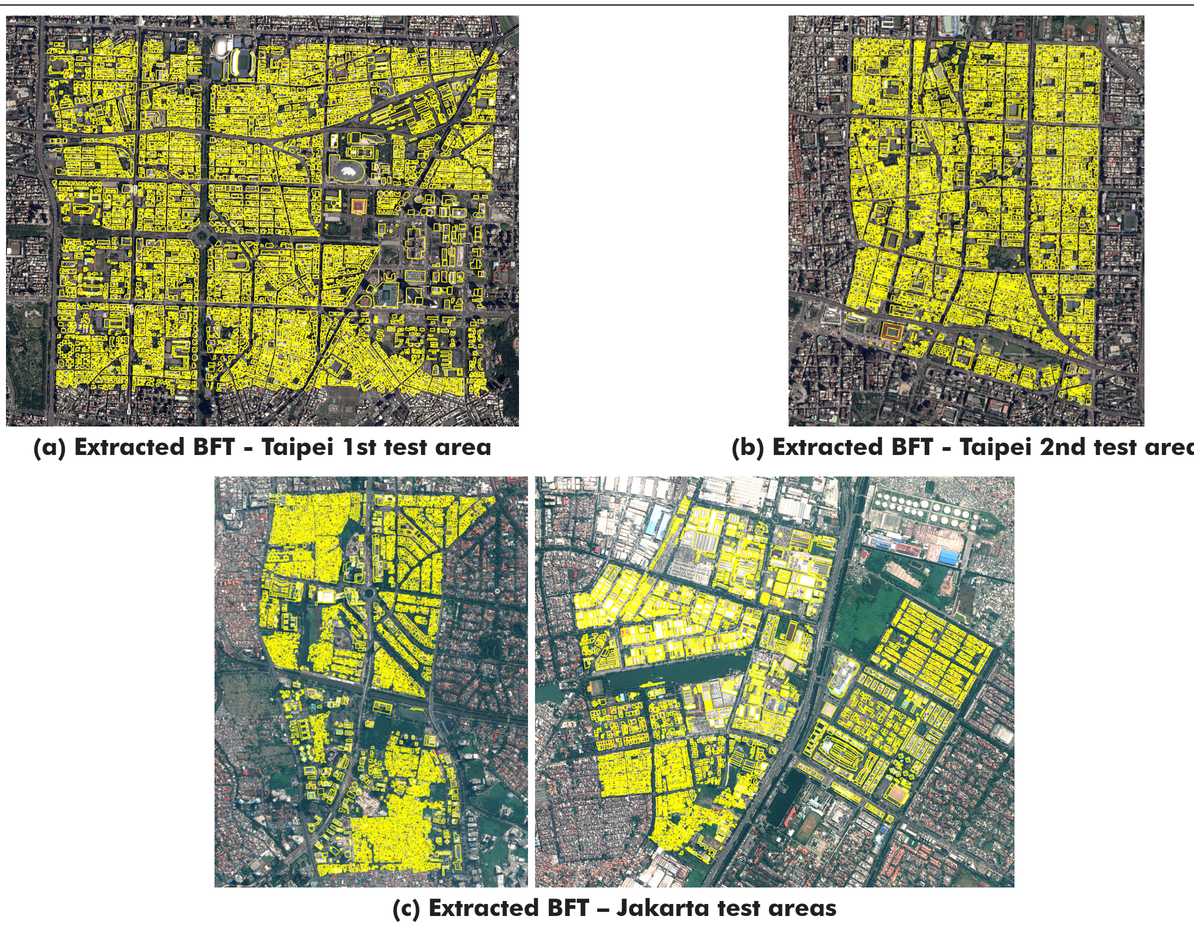

Figure 5. Samples of extracted building footprint (BFT) from Taipei and Jakarta test areas.

Taipei Test Areas

The number of building polygons falling in each Case 1 to 5 are shown in Table 1 for Taipei's two test areas individually and combined. Focusing on the first test (calibration) area, 46.9% of the extracted polygons have a one-to–one (Case 2, ideal) extraction, while Cases 2 and 3 combined totals 67.0%. For estimating total building value exposed to hazards, Cases 3 and 4 as representing dense building clusters would also be considered as correct extraction. This is because Case 3 has one extracted building (polygon) encompassing several tightly-spaced, i.e., essentially inseparable buildings that would be very similar in height and in structural characteristics, and therefore in building exposure and vulnerability characteristics. This also applies for Case 4 where several extracted building polygons with very similar characteristics collectively represent one actual building. With this, the combined polygons over Cases 2, 3, and 4 comprise 95.07% of the extracted. Only a small percentage at 4.93% are in Case 1 (extraneous) polygons. It is noted these percentage counts are based on the total extracted polygon count (i.e., Sum Cases 1 to 4). The number of missed polygons (Case 5) is 713, i.e. 13.5% relative to the total number of extracted polygons. Similar extraction performance is seen for Taipei second test (verification) area. The extracted have 50.7% one-on–one (Case 2), and 95.3% in combined Cases 2, 3, and 4, with only a small 4.71% Case 1 (extraneous polygon). The number of missed polygons (Case 5) is 440, i.e., 8.5% relative to the total number extracted.

The extraction performance, particularly Case 2, is improved for the larger TFA building polygons (Table 1). For building TFA >4000 m^2, Case 2 extraction is slightly improved at 51.8% from 48.8% for the combined Taipei test areas and improving significantly to 71.9% for TFA >8000 m^2. Thus, progressively more of the larger buildings, and thus building values exposed to hazards, are extracted on one-to-one basis. The percentage in extracted Cases 3 and 4 (i.e., building clusters) is essentially unchanged for TFA >4000 m^2, but notably reduced for TFA >8000 m^2 at 27.4%. Greater than 99% accuracy over combined Cases 2 to 4 is achieved for the larger buildings with TFA >4000 m^2 and >8000 m^2 (Table 1); this also holds for the individual test areas (not shown).

The percentage distribution of building polygon counts across Cases 1–5 and cumulative for Taipei's combined test areas are plotted in TFA bins (Figure 6). It is evident that Case 2 (one-to-one) extraction (red bars) becomes dominant at larger building TFA bins. In contrast, Case 1's 506 extraneous polygons (Table 1) and Case 5's 1153 missed polygons were mostly confined to buildings with small TFA of <1000 m^2. This again indicates that the larger buildings are better extracted. Successfully capturing such large buildings is key towards capturing the city's entire built-up TFA, and thus a city's inventory of building values and exposure. Thus Figure 6 shows that the larger TFA>8000 m^2 buildings contributing 43% of the test areas' cumulative TFA.

Detailed error analysis on extracted BFT area and height values are next discussed considering Cases 2, 3, and 4 individually, and covering Taipei first (calibration) and second (verification) test area separately. Table 2 summarizes the BFT area error, dA, for all buildings and building with large TFA >4000 m^2 and >8000 m^2. The results show that 67–74% of all buildings in Cases 2 and 3 had error abs(dA) <30% across the two test areas. In this error calculation, Case 3 used the total BFT areas of the encompassed ground truth (TVD) buildings as these are corresponded to tightly-spaced, inseparable buildings. As expected, there is a significant improvement for the larger TFA buildings where 71–89% in Cases 2 and 3 has abs(dA) <30% for building with TFA >4000 m^2, and >92% for TFA >8000 m^2. By comparison, the errors for

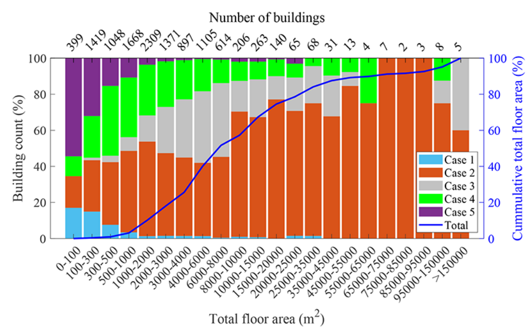

Figure 6. Building count (%) over Cases 1–5 with buildings grouped in total floor area (TFA) bins for combined Taipei test areas. Upper horizontal axis indicates number of buildings in each TFA bin. Solid blue line and right vertical axis indicates the cumulative TFA (%) spanned over the test areas.

Table 1. Count Analysis across Cases 1 to 5 building polygons for Taipei and Jakarta test areas. Percentage numbers in parentheses are based on number of extracted polygons (sum Cases 1 to 4).

	Taipei					Jakarta Test Area		
			Combined Test Areas					
Case	First Test Area (Calibration)	Second Test Area (Verification)	All	TFA >4000 m^2	TFA >8000 m^2	All	TFA >4000 m^2	TFA >8000 m^2
1 (extraneous), n (%)	261 (4.93)	245 (4.71)	506 (4.82)	24 (0.96)	6 (0.75)	642 (6.49)	3 (0.53)	1 (0.28)
2 (one-to-one), n (%)	2485 (46.9)	2635 (50.7)	5120 (48.8)	1301 (51.8)	577 (71.9)	4851 (49.0)	481 (85.1)	299 (84.2)
3 (one to many), n (%)	1065 (20.1)	928 (17.9)	1993 (19.0)	834 (33.2)	145 (18.1)	1793 (18.1)	61 (10.8)	46 (13.0)
4 (many to one), n (%)	1483 (28.0)	1390 (26.7)	2873 (27.4)	352 (14.0)	75 (9.3)	2606 (26.3)	20 (3.5)	9 (2.5)
5 (missed)	[713]	[440]	[1153]	[23]	[12]	[1043]	[8]	[1]
Total Extracted (Sum Cases 1 to 4)	5294	5198	10,492	2511	803	9892	565	355
Sum Cases 2 to 4/Total Extracted (%)	95	95.3	95.2	99.0	99.3	93.4	99.5	99.7

TFA = total floor area.

Table 2. Count and percentage of buildings in Taipei test areas with building footprint error abs(dA) < 20% and < 30%.

		Taipei First Test Area						Taipei Second Test Area					
		All buildings		TFA >4000 m^2		TFA >8000 m^2		All buildings		TFA >4000 m^2		TFA >8000 m^2	
Case		Count	%	Count	%	Count	%	Count	%	Count	%	Count	%
Case 2	abs(dA) < 20%	1345/2485	54	600/783	77	330/376	88	1493/2635	57	376/518	73	160/201	80
	abs(dA) < 30%	1672/2485	67	678/783	87	356/376	95	1864/2635	71	459/518	89	188/201	94
Case 3	abs(dA) < 20%	580/1065	54	274/505	54	92/118	78	514/928	55	185/329	56	14/27	89
	abs(dA) < 30%	759/1065	71	359/505	71	108/118	92	685/928	74	244/329	74	27/27	100
Case 4	abs(dA) < 20%	121/1483	8	47/230	20	8/40	20	114/1390	8	23/122	19	6/35	17
	abs(dA) < 30%	204/1483	14	69/230	30	11/40	28	176/1390	13	36/122	30	7/35	20

TFA = total floor area.

Case 4 buildings are much larger, as expected, since the one extracted polygon encompassed several TVD polygons, but only one TVD polygon was matched with the extracted for the dA error calculation.

Table 3 shows the errors dH in the extracted building heights. For Taipei first (calibration) test area, 91% and 94% of all buildings in Case 2 and 3, respectively had abs(dH) <3 m and with the accuracy being essentially unchanged for the larger TFA buildings, whilst 81% of all buildings in Case 4 had abs(dH) <3 m. The height accuracy for the second (verification) test area was less by comparison, which was attributed to the TVD height values being less accurate due to this area being in an older part of Taipei with older TVD.

The Mean Absolute Errors (MAE) for BFT area, height, and TFA are listed in Table 4 for the combined Taipei test areas. Results at four TFA ranges are shown, comprising all TFA values, TFA ≤4000 m², TFA between 4000 m²–8000 m², and TFA >8000 m². While the MAE values on both BFT area and TFA over all buildings (all TFA values) are high at 37%–40%, the values are much reduced for buildings with TFA between 4000–8000 m² and TFA >8,000 m², with the MAE in TFA being at 29% and 17%, respectively.

The scalability of the building extraction algorithm is next demonstrated by applying the extraction framework to the full Taipei pilot area of 27.9 km² (see Figure 7a). In total, 20,597 building polygons are extracted, of which 2355 are with large BFT area (>1000 m²) and 1957 have height >10 floors. Also 47% (i.e., almost half) of the entire TFA over the pilot area is contributed by the larger buildings (TFA >8000 m²); these buildings comprise only 9% of total building count. Furthermore, these buildings are expected to have small MAE as their extracted BFT area, height, and TFA (Table 4).

Jakarta City

The full scalability of the building extraction is demonstrated for the megacity of Jakarta covering an area of 643 km². The extraction algorithm parameters are first tuned using the Jakarta test areas' ground reference to account for building characteristics being different from Taipei's. The earlier Table 1 also shows the number of extracted building polygons from Jakarta test areas as falling into Cases 1 to 5. Compared to the Taipei test areas, the algorithm had comparable performance in Case 2 (one-to-one) extraction, and with a better improvement for the larger TFA buildings at 84%–85% extraction, with the percentages for Cases 3 and 4 correspondingly reduced. Case 1 extraneous and Case 5 missed polygons remain small as with Taipei's test areas. Figure 8 plots the percentage distribution of building polygons counts across Cases 1–5 and cumulative for Jakarta's combined test areas against TFA bins (i.e., as shown earlier in Figure 6 for Taipei test areas). As with the Taipei test area results, Case 2 (one-to-one) extraction becomes dominant at large TFA bins, while Case 1 (extraneous) polygons and Case 5 missed polygons are mostly confined to small TFA bins. Similarly, the larger building contributed disproportionally to the cumulative TFA, e.g., building with TFA >4000 m² contributed 70.5% of Jakarta's test areas cumulative TFA.

In terms of dA errors on BFT area, 52.4% of all buildings are extracted with abs(dA) < 30%, and further improved for larger TFA (>4000 m²) buildings at 92.9%. The error in building height dH has 75.7% of extracted buildings having abs(dH) < 3 m, and 75.4% (i.e., essentially unchanged) for the larger TFA (>4000 m²) buildings. The MAE values (Table 4) are comparable to that achieved for Taipei test areas, and better for the larger TFA buildings.

The algorithm extracted over 1.247 million buildings for the megacity of Jakarta (Figure 7b). Extracted BFT area, height, and TFA statistics are shown in Figure 9. Jakarta's buildings largely are low rise with 59% (32%) of the buildings are at one (two) story (Figure 9a), and only 1744 buildings having >10 stories. 78% of the buildings have BFT areas of 50–300 m², while only 13,302 buildings have BFT >1000 m² area (Figure 9b). Small TFA <4000 m² buildings contributes to 76% of Jakarta's entire TFA (Figure 9c), this representing 99% of the total number of buildings, whilst large buildings of TFA >8000 m² contributes 18% of Jakarta's entire TFA, i.e., a smaller percentage when compared to the Jakarta (also Taipei) test areas. This is because these test areas, being in their respective downtown core, are more populated with high-rise and large footprint buildings.

Conclusion

The work demonstrates a highly efficient and automated BFT and height extraction methodology using high-resolution satellite stereo images and off-the-shelf software, with an application to the megacity of Jakarta. The methodology is developed using small Taipei test areas where accurate ground reference TVD is available. Differences in building characteristics between the two cities are accounted for via tuning of algorithm parameters using small Jakarta test areas.

The results on extracted buildings are analyzed over the test areas, both on the extraction count over buildings, which can be closely

Table 3. Count and percentage of buildings in Taipei test areas with height error abs(dH) < 2 m and < 3 m.

		Taipei First Test Area						Taipei Second Test Area					
		All buildings		TFA >4000 m²		TFA >8000 m²		All buildings		TFA >4000 m²		TFA >8000 m²	
Case		Count	%	Count	%	Count	%	Count	%	Count	%	Count	%
Case 2	abs(dH) < 2 m	2113/2485	85	675/783	86	316/376	84	1703/2635	65	312/518	60	101/201	50
	abs(dH) < 3 m	2263/2485	91	699/783	89	331/376	88	2116/2635	80	371/518	72	126/201	63
Case 3	abs(dH) < 2 m	959/1065	90	457/505	90	99/118	84	729/928	79	269/329	82	23/27	85
	abs(dH) < 3 m	1001/1065	94	473/505	94	104/118	88	832/928	90	299/329	91	24/27	89
Case 4	abs(dH) < 2 m	1045/1483	70	187/230	81	26/40	65	817/1390	59	62/122	51	14/35	40
	abs(dH) < 3 m	1201/1483	81	199/230	87	28/40	70	996/1390	72	76/122	62	18/35	51

TFA = total floor area.

Table 4. Mean Absolute Errors (MAE) (%) in building footprint (BFA), height, and total floor area (TFA) for buildings in the combined test areas of Taipei.

	Taipei				Jakarta			
Parameter	All TFA buildings	TFA ≤4000 m²	TFA: 4000–8000 m²	TFA >8000 m²	All TFA buildings	TFA ≤4000 m²	TFA: 4000–8000 m²	TFA >8000 m²
BFT MAE	37	42	27	16	37	39	9	8
Height MAE	12	14	8	7	28	29	14	8
TFA MAE	40	45	29	17	48	49	20	15

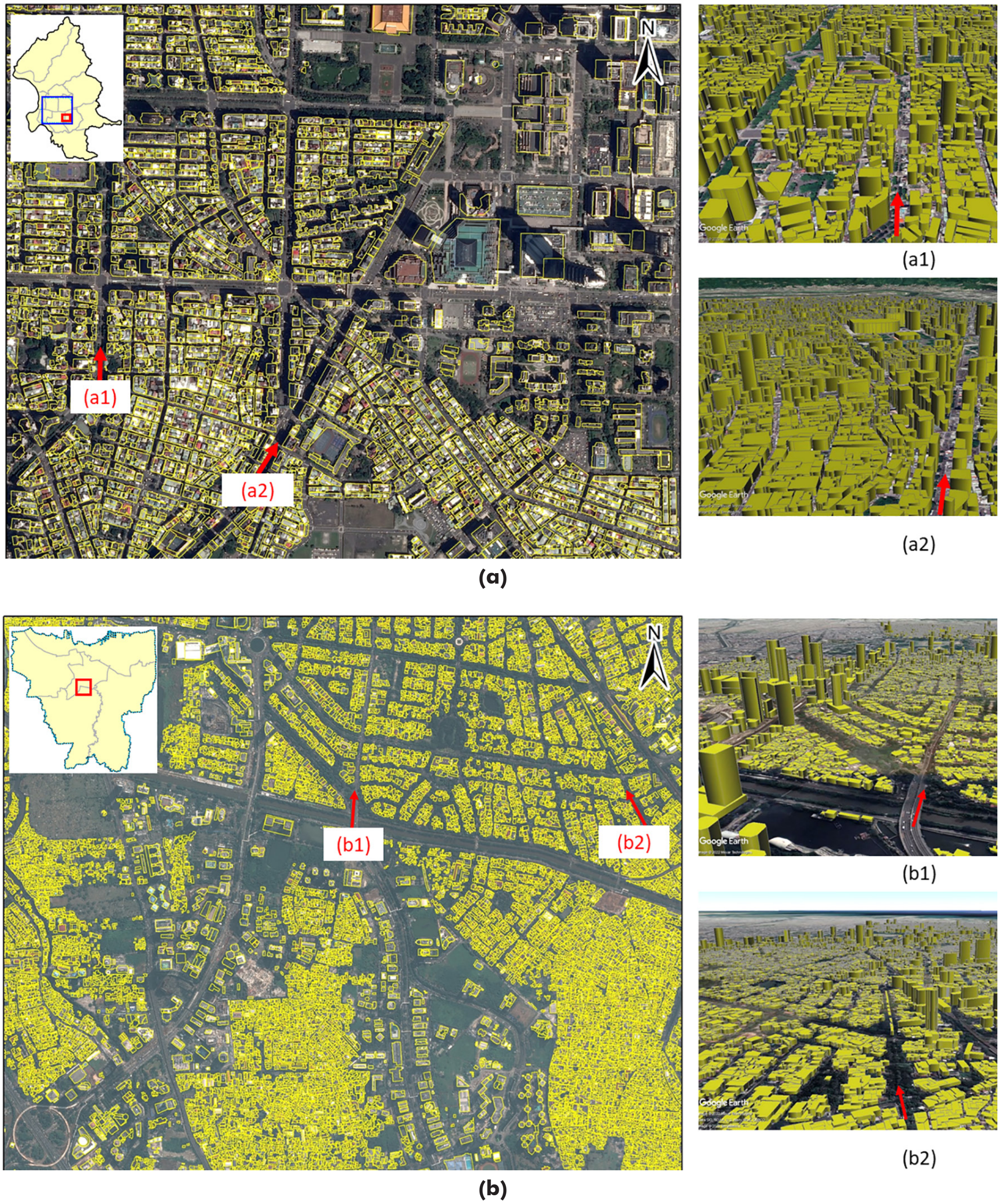

Figure 7. Building polygons extracted from (a) Taipei 27.9 km^2 pilot area and (b) Jakarta over 643 km^2. Solid blue lines in upper left inset indicate the full areal extent covered, and solid red lines show the areal extent of an expanded two-dimensional view with further detailed three-dimensional views shown in the left panels at locations indicated by the red arrows.

spaced in dense urban areas, and on errors in the extracted BFT area, height, and TFA. It is shown that buildings captured in Taipei test areas are at one-to-one (Case 2) extraction for 48.8% of the captured buildings, improving to 71.9% for larger buildings with TFA >8000 m^2, and further reaches 99% accuracy when closely-spaced, inseparable building clusters of similar height and structural characteristics are included, as appropriate for building exposure development. Extraneous and missed building were small in number, and notably are largely confined to small TFA buildings. The MAE in BFT area, while being at 37% over all captured buildings, reduced significantly to 27% for larger TFA buildings (TFA between 4000–8000 m^2), and to 16% for buildings with TFA >8000 m^2. Similar extraction performance and accuracies hold for the Jakarta test areas. It is also shown that the larger TFA buildings, while small in count number, contributes disproportionally to the cumulative TFA for both Taipei and Jakarta test areas, e.g., Jakarta's test areas located in the downtown core have buildings with TFA >4000 m^2 contributing to 70.5% of the cumulative TFA, whilst over the entire Jakarta of 643 km^2, such buildings with >4000 m^2 TFA contributes 24% of the cumulative TFA.

The analyses indicate that the extraction methodology is effective, even for megacities, accurately capturing building inventory covering areas and heights via readily available satellite imagery. This provides

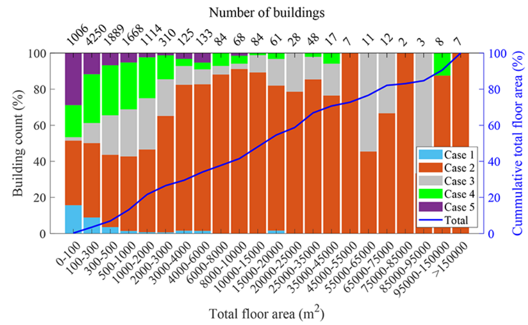

Figure 8. Building count (%) over Cases 1–5 with buildings grouped in total floor area (TFA) bins for combined Jakarta test areas. Upper horizontal axis indicates number of buildings in each TFA bin. Solid blue line and right vertical axis indicates the cumulative TFA (%) spanned over the test areas.

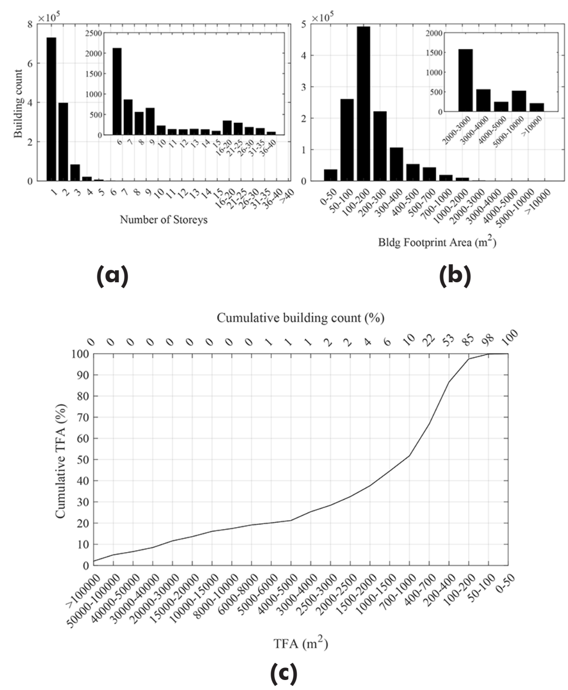

Figure 9. Statistics on buildings in Jakarta. Note in (c) total floor area (TFA) bins are plotted in decreasing bin size and the upper horizontal axis indicate cumulative building count (%).

a cost-effective, readily deployable option for quantifying city-wide building inventory needed in city planning, and for risk analysis under hazards. It would therefore find use in national and regional government units involved in disaster planning and management. Lastly, the extraction methodology can readily take advantage of increasingly more accurate satellite imagery or aerial/UAV images as they become available.

References

Awrangjeb, M., M. Ravanbakhsh and C. S. Fraser. 2010. Automatic detection of residential buildings using LIDAR data and multispectral imagery. *ISPRS Journal of Photogrammetry and Remote Sensing* 65(5):457–467.

Baatz, M. and A. Schäpe. 2000. Multiresolution segmentation: An optimization approach for high quality multi-scale image segmentation. Pages 12–23 in *Proceedings Angewandte Geographische Informationsverarbeitung XII*, *Beiträge zum AGIT-Symposium Salzburg 2000*. Edited by J. Strobl. Karlsruhe, Germany: Herbert Wichmann Verlag.

Belgiu, M. and L. Drăguţ. 2014. Comparing supervised and unsupervised multiresolution segmentation approaches for extracting buildings from very high resolution imagery. *ISPRS Journal of Photogrammetry and Remote Sensing* 96:67–75.

Bittner, K., F. Adam, S. Cui, M. Körner and P. Reinartz. 2018. Building footprint extraction from VHR remote sensing images combined with normalized DSMs using fused fully convolutional networks. *IEEE Journal of Selected Topics in Applied Earth Observations and Remote Sensing* 11(8):2615–2629.

Chen, R., X. Li and J. Li. 2018. Object-based features for house detection from RGB high-resolution images. *Remote Sensing* 10(3):451.

De Angeli, S., F. Dell'Acqua and E. Trasforini. 2016. Application of an earth-observation-based building exposure mapping tool for flood damage assessment. In *Proceedings 3rd European Conference on Flood Risk Management (FLOODrisk 2016)*. Edited by M. Lang, F. Klijn and P. Samuels. *EDP Science*. https://doi.org/10.1051/e3sconf/20160705001.

Figueiredo, R. and M. Martina. 2016. Using open building data in the development of exposure data sets for catastrophe risk modelling. *Natural Hazards and Earth System Sciences* 16(2):417–429. https://doi.org/10.5194/nhess-16-417-2016.

Garcia-Garcia, A., S. Orts, S. Oprea, V. Villena-Martinez and J. G. Rodríguez. 2017. A review on deep learning techniques applied to semantic segmentation. arXiv:1704.06857v1.

Gavankar, N. L. and S. K. Ghosh. 2018. Automatic building footprint extraction from high-resolution satellite image using mathematical morphology. *European Journal of Remote Sensing* 51(1):182–193. https://doi.org/10.1080/22797254.2017.1416676.

Gui, S. and R. Qin. 2021. Automated LoD-2 model reconstruction from very-high-resolution satellite-derived digital surface model and orthophoto. *ISPRS Journal of Photogrammetry and Remote Sensing* 181:1–19.

Ghandour, A. J. and A. A. Jezzini. 2018. Autonomous building detection using edge properties and image color invariants. *Buildings* 8(5):65.

Grossi, P., H. Kunreuther and D. Windeler. 2005. An introduction to catastrophe models and insurance. In *Catastrophe Modeling: A New Approach to Managing Risk*, edited by P. Grossi and H. Kunreuther, 23–42. Boston, Massachusetts: Springer.

Gunasekera, R., O. Ishizawa, C. Aubrecht, B. Blankespoor, S. Murray, A. Pomonis and J. Daniell. 2015. Developing an adaptive global exposure model to support the generation of country disaster risk profiles. *Earth-Science Reviews* 150:594–608. https://doi.org/10.1016/j.earscirev.2015.08.012.

Haithcoat, T. L., W. Song and J. D. Hipple. 2001. Building footprint extraction and 3-D reconstruction from LIDAR data. In *Proceedings IEEE/ISPRS Joint Workshop on Remote Sensing and Data Fusion over Urban Areas (Cat. No.01EX482)*, held in Rome, Italy, 8–9 November 2001. https://doi.org/10.1109/DFUA.2001.985730.

Hermosilla, T., L. A. Ruiz, J. A. Recio and J. Estornell. 2011. Evaluation of automatic building detection approaches combining high resolution images and lidar data. *Remote Sensing* 3(6):1188–1210.

Huang, X. and L. Zhang. 2012. Morphological building/shadow index for building extraction from high-resolution imagery over urban areas. *IEEE Journal of Selected Topics in Applied Earth Observations and Remote Sensing* 5(1):161–172. https://doi.org/10.1109/JSTARS.2011.2168195.

Huete, A., K. Didan, T. Miura, E. P. Rodriguez, X. Gao and L. G. Ferreira. 2002 Overview of the radiometric and biophysical performance of the MODIS vegetation indices. *Remote Sensing of Environment* 83(1):195–213. https://doi.org/10.1016/S0034-4257(02)00096-2.

Im, J., L. J. Quackenbush, M. Li and F. Fang. 2014. Optimum scale in object-based image analysis. In *Scale Issues in Remote Sensing*, edited by Q. Weng. Hoboken, New Jersey: Wiley. https://doi.org/10.1002/9781118801628.ch10.

Jin, X. and C. H. Davis. 2005. Automated building extraction from high-resolution satellite imagery in urban areas using structural, contextual, and spectral information. *EURASIP Journal on Advances in Signal Processing* (14):745309. https://doi.org/10.1155/ASP.2005.2196.

Khoshelham, K., C. Nardinocchi, E. Frontoni, A. Mancini and P. Zingaretti. 2010. Performance evaluation of automated approaches to building detection in multi-source aerial data. *ISPRS Journal of Photogrammetry and Remote Sensing* 65(1):123–133. https://doi.org/10.1016/j.isprsjprs.2009.09.005.

Kuo, H-Y., J-Y. Rau and EY-M. Lo. 2018. Building footprint regulation assisted by road vector derived from open street map. *Proceedings International Symposium on Remote Sensing*, held in Pyeongchang, Korea, 9–11 May 2018.

Lee, D. S., J. Shan and J. S. Bethel. 2003. Class-guided building extraction from Ikonos imagery. *Photogrammetric Engineering & Remote Sensing* 69(2):143–150. https://doi.org/10.14358/PERS.69.2.143.

Li, W., C. He, J. Fang, J. Zheng, H. Fu and L. Yu. 2019. Semantic segmentation-based building footprint extraction using very high-resolution satellite images and multi-source GIS data. *Remote Sensing* 11(4):403.

Lu, T., D. Ming, X. Lin, Z. Hong, X. Bai and J. Fang. 2018. Detecting building edges from high spatial resolution remote sensing imagery using richer convolution features network. *Remote Sensing* 10(9):1496.

Maltezos, E., A. Doulamis, N. Doulamis and C. Ioannidis. 2019. Building extraction from LiDAR data applying deep convolutional neural networks. *IEEE Geoscience and Remote Sensing Letters* 16(1):155–159.

Minaee, S., Y. Y. Boykov, F. Porikli, A. J. Plaza, N. Kehtarnavaz and D. Terzopoulos. 2021. Image segmentation using deep learning: A survey. *IEEE Transactions on Pattern Analysis and Machine Intelligence*. https://doi.org/10.1109/TPAMI.2021.3059968.

NatCatSERVICE–Munich Re. 2019. Münchener Rückversicherungs-Gesellschaft (Munich Reinsurance Company). <https://natcatservice.munichre.com> Accessed 26 March 2021.

Ok, A. O. 2013. Automated detection of buildings from single VHR multispectral images using shadow information and graph cuts. *ISPRS Journal of Photogrammetry and Remote Sensing* 86:21–40. https://doi.org/10.1016/j.isprsjprs.2013.09.004.

Qin, R. 2016. RPC stereo processor (RSP)—A software package for digital surface model and orthophoto generation from satellite stereo imagery. Pages 77–82 in *Proceedings ISPRS Annals of the Photogrammetry, Remote Sensing and Spatial Information Sciences*, held in Prague, Czech Republic, 12–19 July 2016. Copernicus Publications. https://doi.org/10.5194/isprs-annals-III-1-77-2016.

Sahar, L., S. Muthukumar and S. P. French. 2010. Using aerial imagery and GIS in automated building footprint extraction and shape recognition for earthquake risk assessment of urban inventories. *IEEE Transactions on Geoscience and Remote Sensing* 48(9):3511–3520. https://doi.org/10.1109/TGRS.2010.2047260.

Silva, V., H. Crowley, H. Varum and R. Pinho. 2015. Seismic risk assessment for mainland Portugal. *Bulletin of Earthquake Engineering* 13:429–457. https://doi.org/10.1007/s10518-014-9630-0.

Su, G., W. Qi, S. Zhang, T. Sim, X. Liu, R. Sun, L. Sun and Y. Jin. 2015. An integrated method combining remote sensing data and local knowledge for the large-scale estimation of seismic loss risks to buildings in the context of rapid socioeconomic growth: A case study in Tangshan, China. *Remote Sensing* 7(3):2543.

Sun, Y., X. Zhang, X. Zhao and Q. Xin. 2018. Extracting building boundaries from high resolution optical images and LiDAR data by integrating the convolutional neural network and the active contour model. *Remote Sensing* 10(9):1459.

Wei, S., S. Ji and M. Lu. 2020. Toward automatic building footprint delineation from aerial images using CNN and regularization. *IEEE Transactions on Geoscience and Remote Sensing* 58(3):2178–2189.

Xu, Y., L. Wu, Z. Xie and Z. Chen. 2018. Building extraction in very high resolution remote sensing imagery using deep learning and guided filters. *Remote Sensing* 10(1):144.

Yu, D., S. Ji, J. Liu and S. Wei. 2021. Automatic 3D building reconstruction from multi-view aerial images with deep learning. *ISPRS Journal of Photogrammetry and Remote Sensing* 171:155–170.

Yuan, J. 2018. Learning building extraction in aerial scenes with convolutional networks. *IEEE Transactions on Pattern Analysis and Machine Intelligence* 40(11):2793–2798. https://doi.org/10.1109/TPAMI.2017.2750680.

Zhang, L., Z. Shao, J. Liu and Q. Cheng. 2019. Deep learning based retrieval of forest aboveground biomass from combined LiDAR and Landsat 8 data. *Remote Sensing* 11(12). https://doi.org/10.3390/rs11121459.

Zhang, L. and L. Zhang. 2018. Deep learning-based classification and reconstruction of residential scenes from large-scale point clouds. *IEEE Transactions on Geoscience and Remote Sensing* 56(4):1887–1897.

IN-PRESS ARTICLES

Sunil Kumar Pundir, Rahul Dev Garg. Development of technique for Vehicle specific off-road trafficability assessment using soil cone index, water index & geospatial data.

Weidong Li, Fanqian Meng, Yongbo Yu. The use of indices and modified U-Net network in improving the classification of planting structures.

Weiwei Liu. Managing earth hazards using deep reinforcement learning algorithm for industrial IoT network.

Itiya Aneece, Prasad S. Thenkabail. New generation hyperspectral sensors DESIS and PRISMA provide improved agricultural crop classifications.

Yanzhe Shi, Yumin Tan, Yunxin Li, Bo Xu. Automatic registration method of multi-source point clouds based on building facades matching in urban scenes.

Zhang Yan, Wang Xiangyu, Zhang Zhongwei, Sun Yemei, and Liu Shudong. Foreground-Aware Refinement Network for Building Extraction from Remote Sensing Images.

Yumin Tan, Yanzhe Shi, Yunxin Li, and Bo Xu. Automatic registration method of multi-source point clouds based on building facades matching in urban scenes.

Yan Lv, Hongwei Guo, Shuanggen Jin, Lu Wang, Haiyi Bian, and Haijian Liu. Permanganate index variations and factors in Hongze Lake from Landsat-8 images based on machine learning.

Songjing Guo, Xueling Wu, Ruiqing Niu, and Wenfu Wu. Exploring spatiotemporal variations and driving factors of urban comprehensive carrying capacity in the Yangtze River Delta urban agglomeration.

A Semi-Supervised Learning Method for Hyperspectral-Image Open Set Classification

Zhaolin Duan, Hao Chen, Xiaohua Li, Jiliu Zhou, and Yuan Wang

Abstract

We present a conceptually simple and flexible method for hyperspectral-image open set classification. Unlike previous methods, where the abundant unlabeled data inherent in the data set are ignored completely and unknown classes are inferred using score post-calibration, our approach makes the unlabeled data join in and help to train a simple and practical model for open set classification. The model is able to provide an explicit decision score for both unknown classes and each known class. The main idea of the proposed method is augmenting the original training set of K known classes using the pseudo-labeled unknown-category samples that are detected elaborately from the unlabeled data using modified OpenMax and semi-supervised iterative learning. Then a (K + 1)-class deep convolutional neural network model is trained based on the augmented training set with (K + 1) class samples. The model can not only classify instances of each known class but also refuse instances of unknown class explicitly. We validated the proposed method on four well-known hyperspectral-image data sets, obtaining superior performance over previous methods.

Introduction

A hyperspectral image (HSI) consists of hundreds of narrow contiguous-wavelength bands carrying a wealth of spectral information. Taking advantage of the rich spectral information, hyperspectral data are extremely useful in a wide range of applications in remote sensing, such as urban monitoring (Fauvel *et al.* 2008), agriculture (Lanthier *et al.* 2008), change or target detection (Mercier and Girard-Ardhuin 2006; Bovolo 2009). Hyperspectral-image classification, which assigns each pixel to one certain category based on its characteristics, is the most vibrant field of research in the hyperspectral community and has drawn broad attention in the remote sensing field (S. Li *et al.* 2019).

Hyperspectral-image classification (HSIC) methods can be divided into those based on spectral features and those based on spectral-spatial features, according to the input information used. In early research attempts, the spectral vector of the pixel was intuitively used for classification to take advantage of abundant spectral bands (Jia and Richards 1994; Murat Dundar and Landgrebe 2002; Bazi and Melgani 2006; J. Li *et al.* 2010). With the development of imaging technology, hyperspectral sensors can provide higher spatial resolution. As a result, detailed spatial information has become available. It has been found that spectral-spatial-based methods can provide good improvement in terms of classification accuracy (He *et al.* 2018). More and more spectral-spatial feature-based classification frameworks have been developed (Benediktsson *et al.* 2005; Camps-Valls *et al.* 2006), which incorporate the spatial contextual information into pixel-wise classifiers.

Recently, deep convolutional neural networks (DCNNs) have begun to dominate the classification of hyperspectral images, and manual feature engineering has been replaced by automatic deep learning, such as with 3D-CNN (Y. Chen *et al.* 2016), CNN-PPF (W. Li *et al.* 2017), and DFFN (Song *et al.* 2018). Now, HSIC has entered a stage of 99% classification accuracy (Zhong *et al.* 2018; Paoletti *et al.* 2019). However, this high accuracy is achieved under the closed set assumption, in which the classes of all test samples are seen in training time. However, the closed set assumption is easily violated in HSIC, where collecting all possible classes for training is almost impossible. Due to budget limits, sample collection based on a field survey usually covers only a small portion of the study area, and only finite classes of interest are annotated (H. Chen *et al.* 2021). Classifiers with the closed set assumption are prone to errors with samples of unknown classes not of interest, and this limits their usability in HSIC. For example, if a closed set classifier is used to map certain crop types in a real HSI that contains other unknown land covers, it will inevitably overestimate crop area and therefore the total amount of food supplies.

In contrast, open set classification (OSC) assumes that for those test instances that do not belong to any known classes (seen by the classification model in training stage), the classifier must correctly identify them as an extra unknown class, as opposed to incorrectly classifying them as one of the known classes. Multi-class open set classification is challenging because it requires correct probability estimation of all known classes together with simultaneous precise refusal of unknown classes. To tackle this challenge, a number of approaches have been proposed for everyday images (Scheirer *et al.* 2013, 2014; Jain *et al.* 2014; Bendale and Boult 2016; Ge *et al.* 2017; Yoshihashi *et al.* 2019). However, for HSI this research is just getting started. Only a few attempts have been made. Y. Liu *et al.* (2020) directly used OpenMax (Bendale and Boult 2016) for open set HSIC. S. Liu *et al.* (2021) argued that the existing centroid-based method for everyday images was not suitable for few-shot HSIC, and proposed a multi-task deep-learning method based on the idea that the unknown should be poorly reconstructed using the classification feature.

In addition to few-shot mentioned by S. Liu *et al.* (2021), there are other notable differences between hyperspectral-image classification and everyday-image classification. First, the spatial resolution of hyperspectral images is much lower than that of everyday images, as hyperspectral images are remote sensing whereas everyday images are sensing at close range. For example, the India Pines data set, one of the most popular hyperspectral benchmarks, records 16 land cover classes in a region of 4350×4350 m^2 with a 30-m ground sampling distance. As a direct result of low spatial resolution, not all pixels in a hyperspectral image can be annotated with an explicit label. In this article, we borrow the term in the HSI unmixing task and divide the pixels of an HSI into two categories: pure and mixed; we deem only pure pixels suitable as examples for training a classification model. Second, there are more unlabeled than labeled pixels in the existing HSI data sets; for example, the Pavia University data set consists of 42 776 labeled pixels and 164 624 unlabeled pixels. These unlabeled pixels are ignored completely in existing HSIC work. Does that mean that unlabeled data are useless for classification tasks? Certainly not! In this article, we will use

Zhaolin Duan, Hao Chen, Xiaohua Li, and Jiliu Zhou are with the College of Computer Science, Sichuan University, Chengdu 610064, People's Republic of China (lxhw@scu.edu.cn).

Yuan Wang is with the Key Laboratory of Radiation Physics and Technology, Ministry of Education, Institute of Nuclear Science and Technology, Sichuan University, Chengdu 610064, People's Republic of China (wyuan@scu.edu.cn).

Contributed by Ruisheng Wang, September 10, 2021 (sent for review March 14, 2022; reviewed by Perpetual Akwensi, Bo Guo, Amr Abd-Elrahman).

Photogrammetric Engineering & Remote Sensing
Vol. 88, No. 10, October 2022, pp. 653–664.
0099-1112/22/653–664

doi: 10.14358/PERS.21-00067R3

them to help train the HSI open set classification model. Based on these two notable differences between hyperspectral-image classification and everyday-image recognition (low spatial resolution and abundant unlabeled pixels), we present a novel HSI open set classification method based on semi-supervised learning. As shown in Figure 1b, the proposed approach focuses on finding unknown-class examples from the inherent unlabeled data and then mixing them with original samples with explicit labels to create an augmented training set. After that, a standard $(K + 1)$-class DCNN is trained for HSI open set classification.

The existing framework, as shown in Figure 1a, trains a K-class deep convolutional neural network model (DCNN_K) model, fits a group of outlier distribution functions at the training stage, and calibrates the K-score to a $(K + 1)$-score for open set HSIC at the prediction stage. In contrast, in our framework (Figure 1b), the K-class training set is augmented to a $(K + 1)$-class set in advance by a semi-supervised learning method, and a $(K + 1)$-class deep convolutional neural network (DCNN_{K+1}) model is trained, which is used directly for open set HSIC at the prediction stage.

The contributions of this article are as follows:

1. A novel framework is proposed to tackle the challenge of HSI classification in open sets. Different from existing framework, which convert open set classification into a posterior probability calibration task based on the extreme value theory, the proposed framework directly trains a $(K + 1)$-class DCNN model for open set classification based on semi-supervised learning.
2. We let the unlabeled data join in the model training, leading to a simple and effective open set classification model for HSI.
3. A data-augmentation method based on semi-supervised learning is presented, in which OpenMax (Bendale and Boult 2016) is implemented iteratively to pseudo-label the samples in the unlabeled data and then an augmented training set is created by combining the pseudo-labeled samples with the original samples with true labels.
4. Comprehensive experiments are conducted on four typical HSI data sets to evaluate the effectiveness of the proposed method.

Related Work

Open Set Classification

In closed set classification tasks, researchers assume that they have samples from all possible classes (Scheirer *et al.* 2013). However, in practice, enumerating and labeling all classes is impossible; dealing with instances that do not belong to the labeled known classes is inevitable in the prediction stage. This is the problem OSC is faced with (Scheirer *et al.* 2013).

OSC can be described as follows: there is a labeled training set A and a test set B. The training set A consists of labeled examples of K known classes, and the test set B contains M ($>K$) classes which include instances of one or more unknown classes in addition to the instances of K known classes. OSC requires a solution which can identify each known class accurately while simultaneously rejecting the unknown classes correctly instead of assigning any such instance to one of the K known classes. This means we can pose the open set classification problem as a classification of $K + 1$ classes, where all instances of the $M - K$ unknown classes must be assigned to one additional class.

To tackle the challenge, a number of approaches have proposed. Early attempts involved adapting closed set classifiers based on support vector machines (SVM). Scheirer *et al.* (2013) proposed the 1-vs-Set Machine, which detects an unknown class by exploiting a decision space from the marginal distances of a binary SVM classifier. Later, Scheirer *et al.* (2014) proposed a compact abating probability model that extended the 1-vs-Set Machine to a nonlinear Weibull-calibrated SVM (W-SVM) for a multi-class open set scenario. Meanwhile, a few works have explored non-closed set methods for open set tasks. Jain *et al.* (2014), based on statistical extreme value theory, used a Weibull distribution to model the posterior probability of inclusion for each known class and classified an example as having unknown class if the probability was below a rejection threshold.

The origin of deep open set classifiers was OpenMax (Bendale and Boult 2016). Since then, a few deep open set classifiers have been reported. G-OpenMax (Ge *et al.* 2017), a direct extension of OpenMax, trains a network with synthesized unknown data by using generative models. However, it cannot be applied to multi-channel images other than handwritten characters, due to the difficulty of generative modeling. CROSR (Classification-Reconstruction learning for Open-Set Recognition; Yoshihashi *et al.* 2019), another extension of OpenMax, uses latent representations for reconstruction to enhance detection of unknowns. Recently, MDL4OW (S. Liu *et al.* 2021), which is designed for few-shot HSI classification following CROSR's classification and reconstruction joint learning paradigm, used the reconstruction error of whole training data to fit the distribution function of outliers. Among these methods, G-OpenMax share with ours the idea of training a $(K + 1)$-class classifier. The difference is that our approach finds

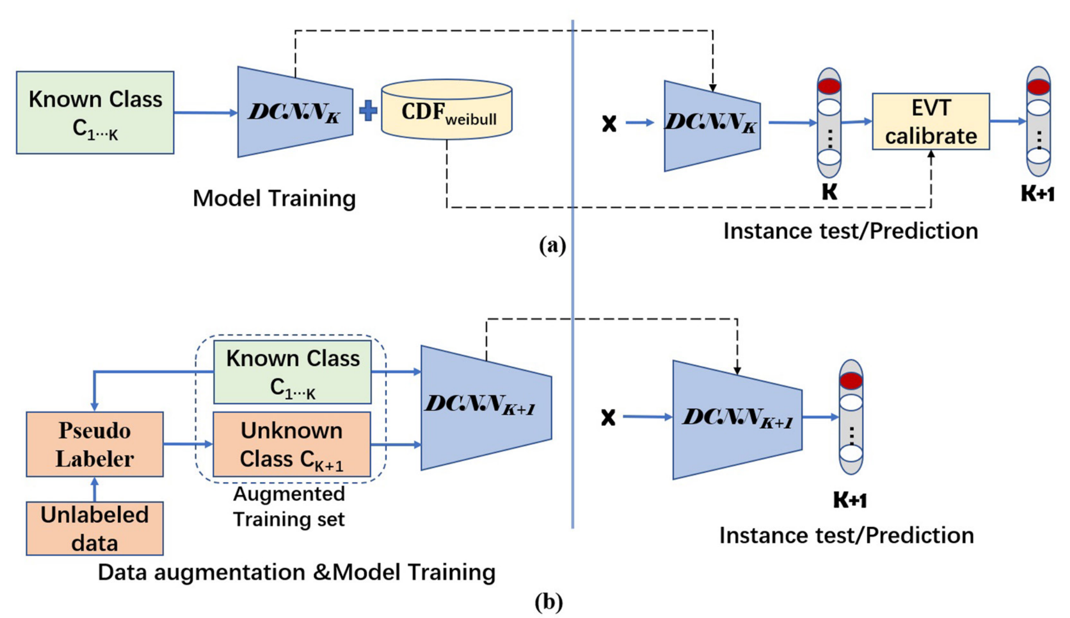

Figure 1. Overview of existing methods and our deep frameworks for HSI open-set classification. (a) Existing deep HSI open set classification (OpenMax, MDL4OWs); (b) Semi-Supervised Learning for HSI Open-Set Classification (SSLOSC). HSI = hyperspectral image.

unknown-class examples from the inherent unlabeled data, whereas G-OpenMax synthesizes them by using generative models based on the original known-class data.

OpenMax

OpenMax (Bendale and Boult 2016), which was initially developed for natural-image OSC and then introduced to HSI (Y. Liu *et al.* 2020), is the origin of existing deep open set classifiers. It is an extension of Softmax that uses extreme value theory to define a compact abating probability model to limit open space risk. The schematic diagram of OpenMax in deep networks is shown in Figure 2, and involves two key modules described in the square area with a yellow background.

Given a set of known classes $\varkappa = \{c_1, c_2, \ldots, c_K\}$, a basic K-class DCNN (DCNN_k) is first trained with the normal Softmax layer to minimize cross entropy loss. For each correctly classified training sample, the activation vector, which represents the output of the deep network's penultimate layer, is then computed, and the mean per-class activation vector μ is calculated using these activation vectors. The distances between these correctly classified training samples' activation vectors and their corresponding class's μ are calculated and used to fit the Weibull distribution of their own class and obtain the corresponding Weibull cumulative distribution function $\mathbf{CDF}^i_{\text{Weibull}}$ with hyperparameters based on extreme value theory:

$$\mathbf{CDF}^i_{\text{Weibull}}\left(\mathbf{D}\left(f\left(\mathbf{x}\right),\mu_i\right);\rho_i\right) = 1 - \exp\left(-\frac{\mathbf{D}\left(f\left(\mathbf{x}\right),\mu_i\right)}{\eta_i}\right)^{\lambda_i}; \quad i = 1,2,\ldots,K \quad (1)$$

Here, f denotes the deep CNN as a function, $f(\mathbf{x})$ represents the activation vector of an input $\mathbf{x}$, and $\mathbf{D}(,)$ denotes the distance measure.

At the test stage, which is critical in OpenMax, the activation vector $\mathbf{y}$ of an input instance $\mathbf{x}$ is revised as $\hat{\mathbf{y}}$ using the $\mathbf{CDF}^i_{\text{Weibull}}$, and then a pseudo-activation value $\hat{\mathbf{y}}_{K+1}$ is computed for unknown classes, which are labeled as $\mathbf{c}_{K+1}$. The process is formulated as

$$y = [y_1, y_2, \ldots, y_k] = f(\mathbf{x}) \quad (2)$$

$$w_j = 1; \quad s_j = \text{argsort}(y_j); \quad j = 1, 2, \ldots, K \quad (3)$$

$$w_{s_i} = 1 - \frac{\alpha - i}{\alpha}\mathbf{CDF}^{s_i}_{\text{Weibull}}\left(\mathbf{D}\left(f\left(\mathbf{x}\right),\mu_{s_i}\right);\rho_{s_i}\right); \quad i = 1,2,\ldots,\alpha \quad (4)$$

$$\hat{y} = y_i * w_i; \quad i = 1, 2, \ldots, K \quad (5)$$

$$\hat{y}_{K+1} = \sum_{i=1}^{K} y_i\left(1 - w_i\right) \quad (6)$$

where s_j is the index in the activation vector sorted in descending order.

Finally, the probability $\mathbf{P}(c_i|\mathbf{x})$ of the input x for each known class c_i (i = 1, 2, …, K) and the unknown class $\mathbf{c}_{K+1}$ is computed using Softmax on the revised (K + 1)-dimension activation vector $\hat{\mathbf{y}}$; the maximum score will yield a corresponding predicted class c^*:

$$\mathbf{P}\left(c_i|\boldsymbol{x}\right) = \frac{exp\left(\hat{y}_i\right)}{\sum_{j=1}^{K+1} exp\left(\hat{y}_i\right)}; \quad i = 1,2,\ldots,K,K+1 \quad (7)$$

$$c^* = \text{argmax}_{c_i}\mathbf{P}(c_i|\mathbf{x}); \quad i = 1, 2, \ldots, K, K+1 \quad (8)$$

Method

In this section, we will first provide an overview of our semi-supervised learning-based HSI open set classification (SSLOSC), followed by a deep insight into the inherent nature of existing hyperspectral data sets and a detailed description of our semi-supervised learning method for training-data augmentation.

Overview of the Proposed Approach

The proposed approach is conceptually simple, as shown in Figure 1b. Different from the existing OSC methods (Figure 1a), which follow a framework of score post-calibration, our approach adopts a framework of training-set pre-augmentation, which aims to augment the original training set with the pseudo-labeled samples and then train a (K + 1)-class DCNN model for HSI open set classification. The proposed approach is a semi-supervised learning method, which combines both unlabeled and labeled data for training the classification model, supervised only by the labeled known-class data. Existing OSC methods are based on supervised learning, which train the classification model using only the known-class labeled data.

The essence of our approach is to make the unlabeled pixels in the HSI data set join in and help train the open set classification model as much as possible. First, a modified OpenMax deep model is trained based on semi-supervised iterative learning. Then the trained model is used to predict the unlabeled data, thus creating pseudo-labels for unlabeled data. An augmented training set is created by combining the original known-class samples with true labels and the new samples with

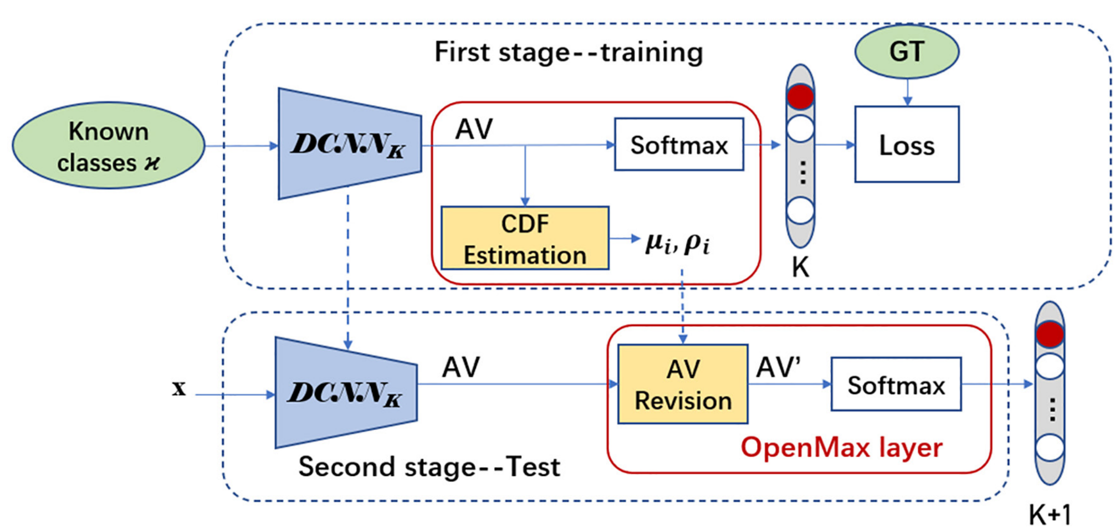

Figure 2. Schematic diagram of OpenMax in deep networks.

pseudo-labels. Finally, a $(K + 1)$-class DCNN model (DCNN_{K+1}) is trained based on the augmented training set for HSI open set classification.

Understanding HSI Data Sets

As we known, the spatial resolution of a hyperspectral image is much lower than that of an everyday image, as hyperspectral images are remote sensing. Low resolution means the spectral vector of a pixel could be either a pure constituent spectrum or a mixture of several pure constituent spectra. In general, a hyperspectral image can be represented as $\mathbf{R} = [r_1, r_2, \ldots, r_{N_p}]$, where N_p is the number of pixels and r_i is the ith pixel, represented as a spectral vector with N_b components, N_b being the number of bands in the hyperspectral image. In the linear mixing model (Guerra *et al.* 2015), each pixel in $\mathbf{R}$ can be represented as a linear combination of a set of spectrally pure pixels or endmembers $\mathbf{e}$, weighted by an abundance factor $\mathbf{a}$, which establishes the proportion of each endmember in the pixel under inspection:

$$\mathbf{r}_i = \sum_{j=1}^{N_e} e_j a_{i,j} + n_i \tag{9}$$

where e_j represents the jth endmember signature, N_e is the number of endmembers in the image, and $a_{i,j}$ is the abundance of endmember e_j in the pixel r_i. The noise present in r_i is contained in the vector n_i.

According to the distribution characters of the abundance factor $\boldsymbol{a}$, we divide the pixels in $\mathbf{R}$ into two categories: if $\boldsymbol{a_i}$ is a one-hot vector or an approximate one-hot vector, r_i is called a pure pixel; otherwise r_i is called a mixed pixel. The scope of the ground that a pure pixel covers would consist of a single land cover, whereas the scope of the ground a mixed pixel covers would consist of several land covers. When it comes to HSI classification, we think only pure pixels are suitable as examples for classifier training, because the class label of an example should be explicit rather than ambiguous.

In HSI classification, almost all data sets consist of one hyperspectral image and a corresponding land cover reference map. Furthermore, the reference map covers only some of the pixels—for example, 50% in the Indian Pines data set, 20% in the Pavia University dataset (for detailed descriptions of the data sets, please see later)—since labeling each pixel is laborious and impossible for an HSI. Given a hyperspectral data set with N_l labeled pixels and N_u unlabeled pixels, the labeled data set and the unlabeled data set can be represented respectively as

$$\mathbf{X} = \{\mathbf{x_i}, \boldsymbol{y_i}\}_{i=1}^{N_l};\ \check{\mathbf{X}} = \{\check{\mathbf{x}}_\mathbf{i}\}_{i=1}^{N_l} \tag{10}$$

where $\mathbf{x_i} \in Z^{m\times m\times N_b}$ is the ith element in the labeled data set $\mathbf{X}$, which represents the spectral-spatial information of the ith labeled pixel, and $y_i \in \{1, 2, \ldots \boldsymbol{K}\}$ is the corresponding class label of the ith labeled pixel, $\check{\mathbf{x}}_i \in Z^{m\times m\times N_b}$ is the ith element in unlabeled data set $\check{\mathbf{X}}$, N_b represents the number of bands, K represents the number of known classes, and m is the size of the spatial neighborhood.

The existing HSI classification approaches usually train their models based only on the labeled data set $\mathbf{X}$, completely ignoring the unlabeled data set $\check{\mathbf{X}}$, although it is always there.

In this article, we try to use the unlabeled data $\check{\mathbf{X}}$ to help train our HSI open set classification model based on semi-supervised learning—combining both unlabeled and labeled data for model training.

Considering the mixing model in Equation 9 and the concept of the pure pixel, we think that all the labeled pixels are pure pixels with noise, since the domain experts have labeled them as ground truth. At the same time, we deem that three cases can occur for unlabeled pixels: a pure pixel belonging to one of the known classes, a pure pixel belonging to the unknown class, or a mixed pixel.

It is clear that finding the pure pixels, especially pure pixels of unknown class, from the unlabeled data $\check{\mathbf{X}}$ will be the key step of our proposed method. After that, a standard $(K + 1)$-class DCNN model will be easily trained for HSI open classification based on the augmented training set, which combines the original known-class examples with true labels and the pseudo-labeled endmember examples.

Training-Data Augmentation Based on Semi-Supervised Learning

Instinctively, we can use OpenMax to get the predicted labels on unlabeled data $\check{\mathbf{X}}$. However, it is unrealistic to directly use the pseudo-labeled examples to augment the original training set. Specifically, the unlabeled data in an HSI data set, as described in the previous section, consists of $K + 2$ classes (K known classes, one unknown class, and another class made up of mixed pixels) rather than $K + 1$. That means the desired detection model should have the ability to distinguish between known-class pure pixels, unknown-class pure pixels, and mixed pixels. It is clear that OpenMax is not qualified. If OpenMax is used directly, the mixed pixels, which are unsuitable as training examples, will be misclassified into either the unknown class or one of the known classes. Furthermore, OpenMax is centroid based, where a large number of training samples are needed to estimate the centroid and the $\text{CDF}_{\text{Weibull}}$ of each class; but the size of some classes in the training set is usually small in HSI classification.

To find the available examples from $\check{\mathbf{X}}$ as reliably as possible, two improvements are introduced. First, we modify OpenMax by thresholding the output confidence scores to distinguish mixed pixels from pure ones. Second, a semi-supervised iterative learning algorithm is proposed to select the pure pixels in the unlabeled data as reliably as possible and then augment the training set.

Modified OpenMax

According to the mixing model, mixed pixels connect to uncertainty, and uncertainty usually connects to low classification confidence (Scheirer *et al.* 2013). So we deem a sample a mixed pixel if the confidence score is low. To separate pure pixels from mixed ones, we modify the OpenMax classifier (Equations 2–8) as follows. We replace Equation 8 by applying a threshold δ to the probability $\mathbf{P}(c_i|\mathbf{x})$ to separate pure pixels from mixed ones:

$$\hat{c}^* = \begin{cases} \arg\max_{c_i} \mathbf{P}(c_i \mid \mathbf{x}) & \text{if } \max_{c_i} \mathbf{P}(c_i \mid \mathbf{x}) > \boldsymbol{\delta}; \quad i = 1,2,\ldots,K,K+1 \\ c_{K+2} & \text{otherwise} \end{cases} \tag{11}$$

where $c_1, c_2, \ldots, c_K$ denote the K known classes, c_{K+1} is the unknown class, and c_{K+2} is the extra class containing mixed pixels which is unsuitable for training.

Semi-Supervised Iterative Learning Algorithm for Training-Data Augmentation

Modified OpenMax (M-OpenMax) helps separate pure pixels from mixed pixels, but it is still not enough for pure-pixel detection, since the size of the original training set is usual small. Here, in order to reliably augment the training data based on the unlabeled data, a semi-supervised iterative learning algorithm is proposed, as shown in Figure 3. Initially, M-OpenMax is trained based on the original K-class training set made of labeled examples of known classes. Then it is used to predict the unlabeled data, thus creating $(K + 2)$-class pseudo-labels. Further, the pseudo-labels are refined based on a cumulative voting strategy. Finally, the original labeled training set and the newly pseudo-labeled known-class samples are combined in a new augmented known-class training set that will be used to retrain M-OpenMax. The process is performed iteratively until the stop condition is met. Specifically, at the nth round, the trained M-OpenMax is used to get the prediction result matrix $L^{(n)}(i,j)$ of the unlabeled data set $\check{\mathbf{X}}$. Then a cumulative result matrix $\mathbf{S}^{(n)}(i,j)$ and a refined prediction result matrix $\hat{\mathbf{L}}^{(n)}(i,j)$ are computed using Equations 13 and 14. Finally, the elements in $\check{\mathbf{X}}$ which are denoted as known classes in $\hat{\mathbf{L}}^{(n)}(i,j)$ are used to update the original training set:

$$\hat{\mathbf{L}}^{(n)}(i,j) = \text{M-OpenMax}^{(n)}(\check{X}) \tag{12}$$

$$\mathbf{S}^{(n)}(i,j) = \mathbf{S}^{(n-1)}(i,j) + \mathbf{L}^{(n)}(i,j) \tag{13}$$

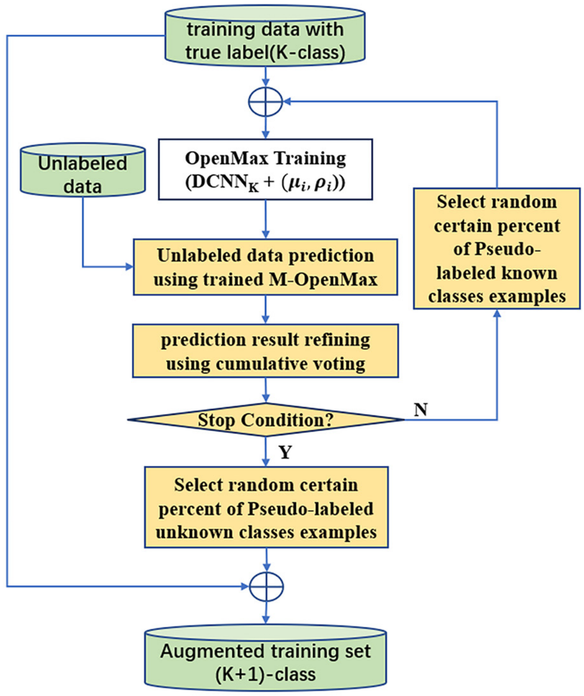

Figure 3. Flow diagram of training-set augmentation module. Assume the original labeled data set X has been divided randomly into training set A and test set B. Here, only the training set A and the unlabeled set are used in the semi-supervised data-augmentation module.

$$\hat{\mathbf{L}}^{(n)}(i,j)=\begin{cases}1 & \text{if } \mathbf{S}^{(n)}(i,j)>\zeta * n\\ 0 & \text{otherwise}\end{cases} \tag{14}$$

where $i = 1, 2, \ldots, K, K+1, K+2$; $j = 1, 2, \ldots, N_u$; K is the number of original known classes; is the number of pixels in the unlabeled data-set; $\boldsymbol{L}^{(n)}(i,j)$ is the predicted class label matrix of $\check{\mathbf{X}}$ among $K + 2$ classes at the nth iteration; and $\hat{\boldsymbol{L}}^{(n)}(i,j)$ is the refined predicted class label matrix. A value of $\boldsymbol{L}^{(n)}(i,j) = 1$ means the predicted class label of $\check{x}_j$ is c_i, and $\zeta = \in(0, 1]$ is the voting factor to control the acceptance degree of pure pixels. Initially, we set $S^{(0)}(i,j) = 0$,

$$\hat{\mathbf{L}}^{(0)}(i,j) = 0.$$

If the stop condition met, the elements in $\check{\mathbf{X}}$ which get a predicted class label c_{K+1} in $\hat{\boldsymbol{L}}^{(n)}(i,j)$ will be mixed with the K-class training set to create the augmented $(K + 1)$-class training set. After that, a standard $(K + 1)$-class DCNN model will be trained based on the augmented training set.

It is worth pointing out that both the augmented K-class training set of known classes and the final $(K + 1)$-class augmented training set use a parameter sample_rate to control the percentage of pseudo-labeled data that we mix with the original training samples. Setting sample_rate = 0.0 means that the model will use only training samples with true labels, and sample_rate = 0.5 means that the model will use original training samples with true labels and half of the pseudo-labeled samples.

<u>Stop Condition:</u> In general, the higher the number of iterations, the more reliable the detected unknown-class examples with pseudo-labels. So we can use a higher iteration number as the stop condition. However, we found that with increasing iterations, the number of unknown-class examples stabilizes. So we set the stop condition as

$$\frac{\Sigma_j\left(\left|\hat{\mathbf{L}}^{(n)}(K+1,j)-\hat{\mathbf{L}}^{(n-1)}(K+1,j)\right|\right)}{\Sigma_j\hat{\mathbf{L}}^{(n)}(K+1,j)}<\mu \tag{15}$$

Here, we call the ratio on the left side of the equation the update rate of the unknown class in the unlabeled data.

Experiments and Results

Data Sets

To validate the performance of our method, we conduct experiments on four well-known hyperspectral image data sets: Indian Pines (IP), Salinas Valley (SV), Kennedy Space Center (KSC), and Pavia University (PU).

The IP data set was gathered by AVIRIS sensor over the Indian Pines test site in northwestern Indiana and consists of a 145×145 image with 224 spectral reflectance bands in the wavelength range 400–2500 nm. Although the image contains 21 025 pixels, only 10 249 are labeled into the 16 classes in the reference map, as shown in Figure 4b, in which black regions are uncovered by the ground truth. The number of bands is reduced to 200 by removing bands covering the region of water absorption. The sample distribution is very unbalanced in this data set, where some classes contain more than 2000 pixels and some have only 20 pixels. In order to validate the open set classification, we have made two open set scenarios based on the original IP data set. In the first one, called the 12vs4 scenario, four classes are randomly chosen from the larger-size categories as the unknown/novel class and the remaining 12 classes are known classes. In the second one, called the 8vs8 scenario, four smaller-size and four larger-size categories are chosen as known classes and the remaining eight classes as the unknown/novel class.

The SV data set was collected by 224-band AVIRIS sensor over Salinas Valley, California, and is characterized by higher spatial resolution (3.7 m/pixel). As with the IP scene, the bands are reduced to 203 after removal of bands covering the region of water absorption. This data set includes a 217×512 image, in which only 54 129 pixels are labeled into 16 classes. Similar to S. Liu *et al.* (2021), we manually annotated some artificial materials, which should not belong to any of the original known classes, as the unknown/novel class for open set classification testing.

The KSC data set was collected by AVIRIS instrument over the Kennedy Space Center in Florida, USA, in 1996. Once noisy bands are removed, the resulting 512×614 image contains 176 bands, ranging from 400 to 2500 nm. Although the image contains 314 368 pixels, only 5211 pixels are annotated, into 13 different land cover types. By observing the false-color map of HSI, we manually annotated some pixels, which are totally different from the original labeled land cover types, as the unknown/novel class for OSC.

The PU data set was acquired by the ROSIS sensor during a flight campaign over Pavia in northern Italy. It includes a 610×340 image with 103 spectral bands. Only 42 776 pixels are labeled, into nine classes, in the reference map. We manually annotated a swimming pool, some vehicles, and some buildings as the unknown/novel class for OSC.

For each open set scenario, we randomly choose 20% of samples from each known class as the training set; the remaining 80% of samples of each known class and all samples from the unknown class are used as the testing set. The data-set settings of the five scenarios are displayed in Tables 1–5.

Evaluation Metrics

The following four metrics were selected to assess the performance of the classification model in open set scenarios:

- **F1 measure.** As suggested by Scheirer *et al.* (2013), we use the composite indicator as the first measure. For each class, its definition is

$$F1_i=\frac{2\text{Precision}_i\times\text{Recall}_i}{\text{Precision}_i+\text{Recall}_i};\quad i=1,2,\ldots,K,K+1 \tag{16}$$

$$\text{Precision}_i=\frac{\text{TP}_i}{\text{TP}_i+\text{FP}_i} \tag{17}$$

Table 1. IP data set, 12vs4 scenario, for OSC.

Category	Class	Name	Train	Test
Known	1	Alfalfa	9	37
	2	Corn-notill	286	1142
	3	Corn-min	166	664
	4	Corn	47	190
	7	Grass/pasture-mowed	6	22
	8	Hay-windrowed	96	382
	9	Oats	4	16
	10	Soybeans-notill	194	778
	11	Soybeans-min	491	1964
	12	Soybeans-clean	119	474
	13	Wheat	41	164
	16	Stone-steel towers	19	74
Unknown	5	Grass/pasture	—	483
	6	Grass/trees	—	730
	14	Woods	—	1265
	15	Bldg-grass-tree-drives	—	386
Unlabeled	—	—	10 776	

IP = Indiana Pines; OSC = open set classification.

Table 2. IP data set, 8vs8 scenario, for OSC.

Category	Class	Name	Train	Test
Known	2	Corn-notill	286	1142
	3	Corn-min	166	664
	4	Corn	47	190
	8	Hay-windrowed	96	382
	10	Soybeans-notill	194	778
	11	Soybeans-min	491	1964
	12	Soybeans-clean	119	474
	13	Wheat	41	164
Unknown	1	Alfalfa	—	46
	5	Grass/pasture	—	483
	6	Grass/trees	—	730
	7	Grass/pasture-mowed	—	28
	9	Oats	—	20
	14	Woods	—	1265
	15	Bldg-grass-tree-drives	—	386
	16	Stone-steel towers	—	93
Unlabeled	—	—	10 776	

IP = Indiana Pines; OSC = open set classification.

Table 3. SV data set for OSC.

Category	Class	Name	Train	Test
Known	1	Brocoli-green-weeds-1	402	1607
	2	Brocoli-green-weeds-2	745	2981
	3	Fallow	395	1581
	4	Fallow-rough-plow	279	1115
	5	Fallow-smooth	536	2142
	6	Stubble	792	3167
	7	Celery	716	2863
	8	Grapes-untrained	2254	9017
	9	Soil-vineyard-develop	1241	4962
	10	Corn-senesced-green-weeds	656	2622
	11	Lettuce-romaine-4wk	214	854
	12	Lettuce-romaine-5wk	385	1542
	13	Lettuce-romaine-6wk	183	733
	14	Lettuce-romaine-7wk	214	856
	15	Vineyard-untrained	1454	5814
	16	Vineyard-vertical-trellis	361	1446
Unknown	17	Novel	—	6336
Unlabeled	—	—	50 639	

OSC = open set classification; SV = Salinas Valley.

Table 4. KSC data set for OSC.

Category	Class	Name	Train	Test
Known	1	Scrub	152	609
	2	Willow-swamp	49	194
	3	CP-hammock	51	205
	4	Slash-pine	50	202
	5	Oak/broadleaf	32	129
	6	Hardwood	46	183
	7	Swap	21	84
	8	Graminoid-marsh	86	345
	9	Spartina-marsh	104	416
	10	Cattail-marsh	81	323
	11	Salt-marsh	84	335
	12	Mud-flats	101	402
	13	Water	185	741
Unknown	14	Novel	—	2783
Unlabeled	—	—	306 374	

KSC = Kennedy Space Center; OSC = open set classification.

Table 5. PU data set for OSC.

Category	Class	Name	Train	Test
Known	1	Asphalt	1326	5305
	2	Meadows	3730	14 919
	3	Gravel	420	1679
	4	Trees	613	2451
	5	Painted metal sheets	269	1076
	6	Bare soil	1006	4023
	7	Bitumen	266	1064
	8	Self-blocking bricks	736	2946
	9	Shadows	189	758
Unknown	10	Novel	—	4443
Unlabeled	—	—	160 181	

OSC = open set classification; PU = Pavia University.

$$\mathrm{Recall}_i = \frac{\mathrm{TP}_i}{\mathrm{TP}_i + \mathrm{FN}_i} \tag{18}$$

where TP_i, FN_i, and FP_i denote the true positive, false negative, and false positive rates, respectively, of the ith class.

- **Macro-F1.** Based on the F1 measure of each class, macro-F1 is defined to evaluate the overall performance:

$$\text{macro-}F1 = \frac{1}{K+1}\sum_{i=1}^{K+1} F1_i \tag{19}$$

- **Open overall accuracy ($\mathbf{OA_{open}}$).** This measure indicates the proportion of correct classification of all test samples:

$$\mathrm{OA_{open}} = \frac{\sum_{i=1}^{K+1}\mathrm{TP}_i}{\sum_{i=1}^{K+1}\mathrm{TP}_i + \mathrm{FN}_i} \tag{20}$$

where TP_i and FN_i are the true positive and false negative rates of the ith class, K is the number of known classes, and $K + 1$ is the unknown class.

- **Known overall accuracy ($\mathbf{OA_{known}}$).** In HSI classification, we are more interested in the accuracy of known classes rather than of the unknown class. However, the $\mathrm{OA_{open}}$ metric takes the accuracy of the unknown class into account. If the known classes account for only a small portion of the data, this metric will be dominated by the unknown class. For reference purposes, we use $\mathrm{OA_{known}}$ as follows to indicate the overall accuracy of the known classes:

$$\mathrm{OA_{known}} = \frac{\sum_{i=1}^{K}\mathrm{TP}_i}{\sum_{i=1}^{K}\mathrm{TP}_i + \mathrm{FN}_i} \tag{21}$$

Experiment Configuration

The experiments were conducted using PyTorch on a machine equipped with an Intel i5-8500 CPU, an Nvidia GeForce GTX 1080 Ti graphics processing unit, and 32 GB of RAM.

During the training phase, the AdaDelta optimizer was used for back-propagation, the minibatch size was 100, the learning rate was 0.01, the momentum was 0.9, the weight decay was 0.0001, and the number of training epochs was 200.

In the experiments, the threshold δ in Equation 11 was experimentally set at 0.95, the voting factor ζ mentioned in Equation 14 was experimentally set at 0.7, and the stop threshold   was set at 0.01. We compare our method with various others: closed DCNN (Paoletti *et al.* 2019), naïve open DCNN SoftMax* (Bendale and Boult 2016), plain DCNN OpenMax (Bendale and Boult 2016; Y. Liu *et al.* 2020), and MDL4OW and MDL4OW/C (S. Liu *et al.* 2021). For SoftMax* and MDL4OW, the unknown class was determined with a threshold of 0.5. For OpenMax, following Y. Liu *et al.* (2020), we set the tail number and α as 20% of the number of the training samples and 5, respectively. In all methods, the DCNN classifier, whether $DCNN_K$ or $DCNN_{K+1}$, had an equivalent architecture to pResNet (Paoletti *et al.* 2019), just with adjustments to the final layer so that the output matched the class number. For $CDF_{Weibull}$ fitting, the libMR (Scheirer *et al.* 2011) FitHigh function was used.

Experiment Results

Each experiment followed the steps of training, testing, and prediction—that is, the model was first trained using the training set, then the test set was fed to the trained model and objective metrics were calculated on the confusion matrix. Lastly, the entire HSI was predicted using the model and the classification map was acquired for visual illustration. Among the compared methods, the trained models of OpenMax, MDL4OW, and MDL4OW/C consist of two parts—$DCNN_K$ and $CDF_{Weibull}$—whereas the models of closed DCNN, SoftMax*, and our SSLOSC contain only a single standard DCNN model.

Results on IP Data Set

In this experiment, we applied the proposed method to two artificial open set scenarios. Tables 6 and 7 display the class-wise F1, macro-F1, OA_{open}, and OA_{known} under the 12vs4 and 8vs8 scenarios, respectively. Under both scenarios, our proposed SSLOSC method achieved the best performance. Under the 12vs4 scenario, macro-F1 and OA_{open} scores were 31% and 37% higher than for the closed method, which cannot reject the unknown class, and 12% and 12% higher than OpenMax, which was the second best among the OSC methods.

Table 6. Classification accuracy on IP data set, 12vs4 scenario. The bold face is the 1st result, and the italic is the 2nd result.

Class	Closed	SoftMax*	MDL4OW	MDL4OW/C	OpenMax	SSLOSC
1	0.18	0.63	0.47	0.68	0.77	0.91
2	0.97	0.98	0.91	0.95	0.92	0.97
3	0.97	0.97	0.96	0.95	0.80	0.97
4	0.92	0.88	0.88	0.90	0.82	0.95
7	0.04	0.38	0.32	0.30	0.92	0.61
8	0.96	0.96	0.94	0.96	0.75	1.00
9	0.19	0.23	0.56	0.46	0.47	0.87
10	0.89	0.93	0.89	0.92	0.86	0.98
11	0.96	0.96	0.90	0.91	0.91	0.98
12	0.92	0.95	0.94	0.94	0.86	0.99
13	0.15	0.33	0.29	0.27	0.87	0.99
16	0.99	0.98	0.74	0.97	0.91	1.00
Unknown (5, 6, 14, 15)	0.00	0.80	0.71	0.76	*0.84*	**0.98**
Macro-F1	0.63	0.77	0.73	0.77	*0.82*	**0.94**
OA_{open}	0.61	*0.86*	0.81	0.83	*0.86*	**0.98**
OA_{known}	**0.97**	*0.96*	0.94	0.94	*0.80*	**0.97**
Stop round	—	—	—	—	—	6

IP = Indiana Pines.

Table 7. Classification accuracy on IP data set, 8vs8 scenario. The bold face is the 1st result, and the italic is the 2nd result.

Class	Closed	SoftMax*	MDL4OW	MDL4OW/C	OpenMax	SSLOSC
2	0.93	0.94	0.95	0.94	0.93	0.97
3	0.96	0.96	0.96	0.94	0.91	0.97
4	0.83	0.85	0.89	0.89	0.84	0.90
8	0.31	0.49	0.75	0.85	0.95	0.97
10	0.62	0.76	0.91	0.93	0.90	0.95
11	0.94	0.96	0.91	0.91	0.95	0.97
12	0.91	0.95	0.86	0.86	0.92	0.88
13	0.29	0.39	0.06	0.30	0.92	0.61
Unknown (1, 5, 6, 7, 9, 14, 15, 16)	0.00	0.65	0.81	0.78	*0.90*	**0.94**
Macro-F1	0.64	0.77	0.79	*0.82*	**0.91**	**0.91**
OA_{open}	0.59	0.77	0.85	0.83	*0.92*	**0.94**
OA_{known}	**0.98**	0.88	0.94	0.94	0.94	*0.96*
Stop round	—	—	—	—	—	9

IP = Indiana Pines.

In addition, we can see that our SSLOSC has a higher OA_{known} score (0.97 in the 12vs4 scenario and 0.96 in the 8vs8 scenario), which ensures the effectiveness of the model when applied only to known classes. At the same time, its OA_{open} scores (0.98 in 12vs4 and 0.94 in 8vs8) are comparable to its OA_{known} scores, which means the unknown instances in the test set had less influence on the overall classification accuracy. And amazingly, for the unknown class, our SSLOSC got a high F1 score (0.98 in 12vs4 and 0.94 in 8vs8), which means most unknown instances were rejected correctly by the model. Moreover, the macro-F1 scores were 0.94 and 0.91, close to ideal performance.

For visual illustrative purposes, we show the open set classification maps under two scenarios in Figures 4 and 5. The reference map is shown in part b of both figures, where white means the unknown class and black means unlabeled pixels. The classification maps obtained by different methods are shown in parts c–h, where white and gray means that the sample was rejected as unknown. Specifically, only the white rejected pixels are considered in the computation of evaluation metrics, since they have a ground truth in the reference map. From Figure 4, we can notice that the closed method, as shown in part c, misclassified unknown (white in reference map) and all unlabeled (black in reference map) as known classes, leading to a lower OA_{open} (see Tables 6 and 7). Compared with other open methods, the proposed SSLOSC model, as shown in part h, successfully rejected most of the unknown instances while maintaining high accuracy on the known classes. In contrast, the other open methods, as shown in parts d–g, either incorrectly rejected some known instances (the region marked with a red boundary) as unknown or misclassified some unknown instances (the region marked with a yellow boundary) as known. Furthermore, from the false-color map in part a and the legend in part i, we can see that the IP data set mainly covers an agricultural region. It is obvious that the road on the upper side of the image is nonagricultural class and should be rejected. However, SoftMax*, MDL4OW, and MDL4OW/C misclassified the road as wheat, instead of recognizing it as unknown, as shown in Figures 4d–f and 5f, whereas our SSLOSC model successfully rejected it as unknown, as shown in Figures 4h and 5h.

Results on SV Data Set

To show the generalization of the proposed method in estimating crops, the SV data set, which has higher spatial resolution, was tested. The 16 agricultural classes contained in the original data set are regarded as known classes. In addition, we manually annotated some of the created materials as unknown class (white region in the reference map) from the unlabeled data, as shown in Figure 6b. The classification results on the test set are presented in Table 8. Similar to the result with the IP data set, SSLOSC achieved the best performance among all OSC methods. This experiment strongly shows the potential of the proposed SSL-based method in precisely estimating crop area.

Figure 6 illustrates the classification maps of different methods on this data set. We can notice that the proposed method successfully rejected most created materials unrelated to crops while maintaining high identification accuracy on the agricultural crop, as shown in Figure 6h. In contrast, other open methods either incorrectly rejected some known instances (the region marked with a red boundary) as unknown, as shown in Figures 6d, f, and g, or misclassified some unknown instances (the region marked with a yellow boundary) as known, as shown in Figure 6d–e. Furthermore, MDLO4W and MDLO4W/C totally failed to recognize some unknown instances (the road in the middle of the image) as unknown, as shown in Figure 6e–f.

Results on KSC Data Set

The KSC data set contains 13 land cover classes in marshland. In addition, we manually annotated some of the created materials (bridge, road, and boat) as the unknown class, as shown in the reference map in Figure 7b. The test results are listed in Table 9. Among all the OSC methods, SSLOSC achieved the best performance in terms of macro-F1, OA_{open}, and F1 of the unknown class.

The visualization of OSC results for this data set is shown in Figure 7. As can be observed, the proposed SSLOSC can provide spatially consistent classification outputs with well-delineated object borders and very few classification interferers.

Results on PU Data Set

The PU data set is more complicated, providing nine classes of samples whose spatial distribution is scattered. The scattered distribution brings much difficulty to the OSC task. In addition, the interclass spectral similarity is significant and the intraclass spatial variability is large (S. Liu *et al.* 2021). Attributed to these characteristics of the data set, though the proposed SSLOSC got a high OA_{known} score (0.98), the rejection ratio for the unknown class was low ($F1_{unknown}$ = 0.62), although it stood head and shoulders above those of other OSC methods, as shown in Table 10.

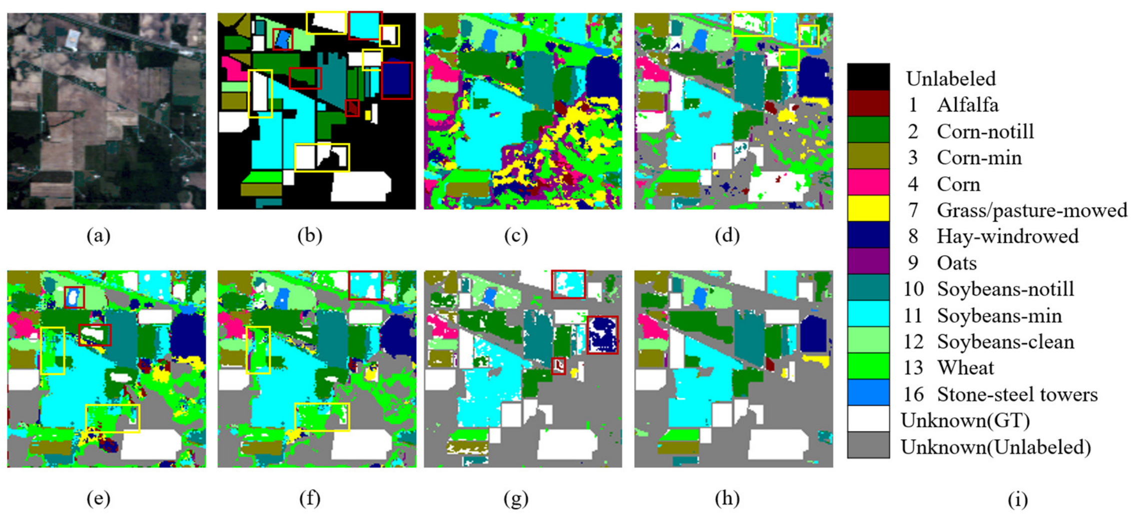

Figure 4. Classification map on the IP 12vs4 scenario. (a) False-color map; (b) reference map; (c) CSC-based $DCNN_k$; (d) Softmax*; (e) MDLO4W; (f) MDLO4W/C; (g) OpenMax; (h) SSLOSC; (i) legend. CSC = closed set classification; IP = Indiana Pines.

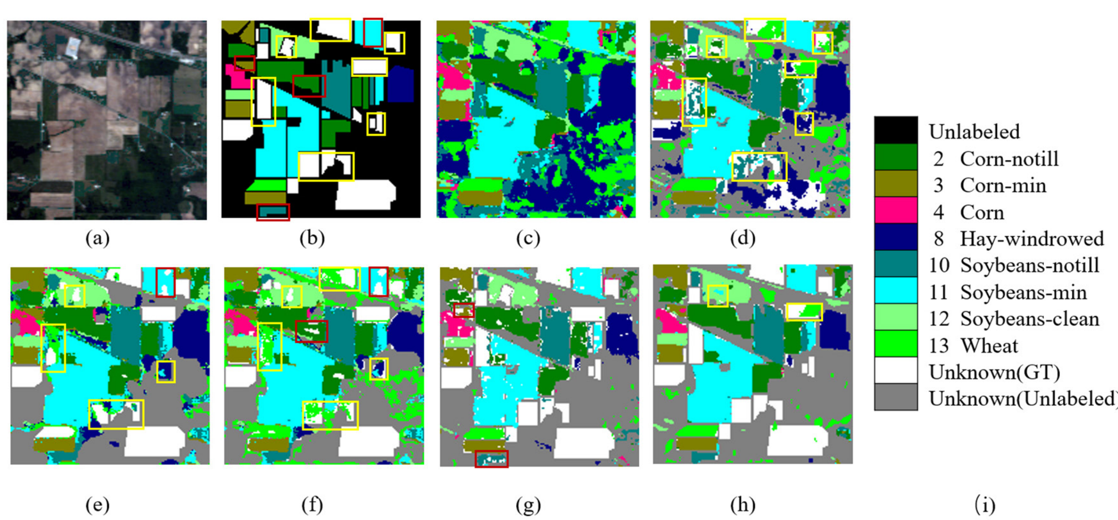

Figure 5. Classification map on the IP 8vs8 scenario. (a) False-color map; (b) reference map; (c) CSC-based $DCNN_k$; (d) Softmax*; (e) MDLO4W; (f) MDLO4W/C; (g) OpenMax; (h) SSLOSC; (i) legend. CSC = closed set classification; IP = Indiana Pines.

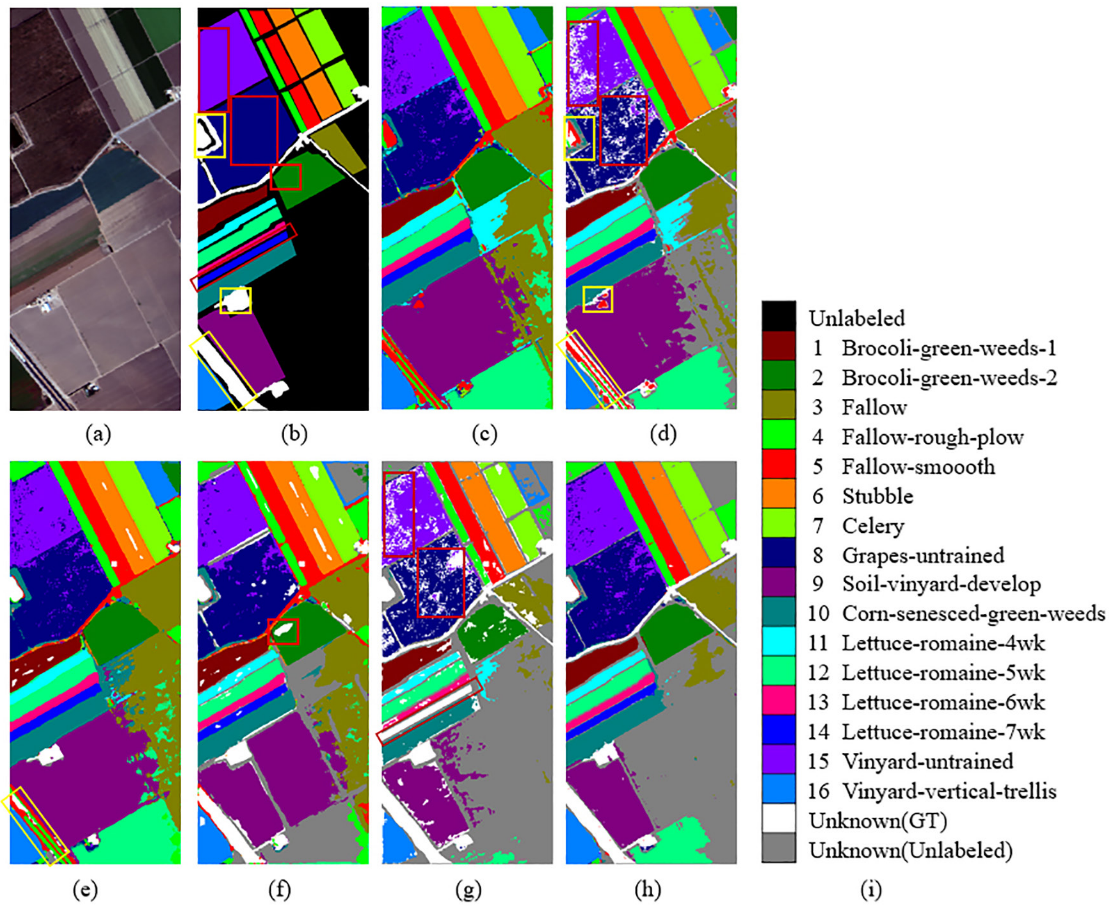

Figure 6. Classification map on the SV data set. (a) False-color map; (b) reference map; (c) CSC-based DCNN$_k$; (d) Softmax*; (e) MDLO4W; (f) MDLO4W/C; (g) OpenMax; (h) SSLOSC; (i) legend. CSC = closed set classification; SV = Salinas Valley.

The visualization of OSC results for this data set is shown in Figure 8. We can see that the proposed SSLOSC provides better spatially consistent classification outputs and fewer classification interferers than OpenMax, although the two methods achieved almost identical scores in terms of OA_{open}, macro-F1, and $F1_{unknown}$.

Sensitivity Analysis of Semi-Supervised Iterative Learning

The overall performance of our method depends on the pseudo-labeled unknown-class samples developed using semi-supervised iterative learning, so the classification performance of OpenMax in intermediate iterative steps is vital. In this section, taking the IP data set as our example, we removed four classes from the original data set and trained OpenMax iteratively based on the training samples from the remaining 12 known classes (penultimate column in Table 1) and the unlabeled data (last row in Table 1) using our semi-supervised learning algorithm, displayed in Figure 3. We then tested the intermediate OpenMax on the test samples (the last column in Table 1). The classification performance of OpenMax and the update rate of the unknown class as defined in Equation 15 in the iterative learning process are displayed in Figure 9. We can notice that the classification performance of OpenMax increases and the update rate of the unknown class decreases with more iterative rounds, especially in the first few rounds. This means that augmenting the known-class training set using the prediction result of the unlabeled data can improve the classification performance of OpenMax. In turn, the improved OpenMax will predict the unlabeled data more precisely and make the augmented known-class training set more reliable. After several rounds, the pseudo-labels of unlabeled data will tend to stabilize and can be used to augment

Table 8. Classification accuracy on SV data set. The bold face is the 1st result, and the italic is the 2nd result.

Class	Closed	SoftMax*	MDL4OW	MDL4OW/C	OpenMax	SSLOSC
1	0.99	1.00	0.96	0.97	0.97	1.00
2	1.00	1.00	1.00	0.97	0.96	1.00
3	0.87	0.90	0.88	0.93	0.91	0.99
4	0.74	0.78	0.66	0.90	0.96	0.99
5	0.57	0.60	0.66	0.76	0.95	0.86
6	0.96	0.99	0.95	0.94	0.99	0.99
7	0.97	0.98	1.00	0.97	0.95	1.00
8	0.86	0.88	0.93	0.93	0.86	0.84
9	0.81	0.84	0.97	0.98	0.95	0.98
10	0.88	0.94	0.94	0.93	0.96	0.97
11	0.88	0.94	1.00	0.97	0.93	1.00
12	1.00	1.00	1.00	0.98	0.97	1.00
13	1.00	1.00	1.00	0.99	0.86	0.99
14	0.99	1.00	1.00	0.98	0.00	0.99
15	0.92	0.92	0.92	0.91	0.86	0.90
16	0.98	1.00	1.00	0.98	0.95	0.99
Unknown (novel)	0.00	0.37	0.39	0.68	*0.78*	**0.93**
Macro-F1	0.85	0.89	0.90	*0.93*	0.87	**0.97**
OA_{open}	0.78	0.83	0.89	*0.91*	0.88	**0.96**
OA_{known}	**0.99**	*0.98*	0.97	0.94	0.86	*0.98*
Stop round	—	—	—	—	—	6

SV = Salinas Valley.

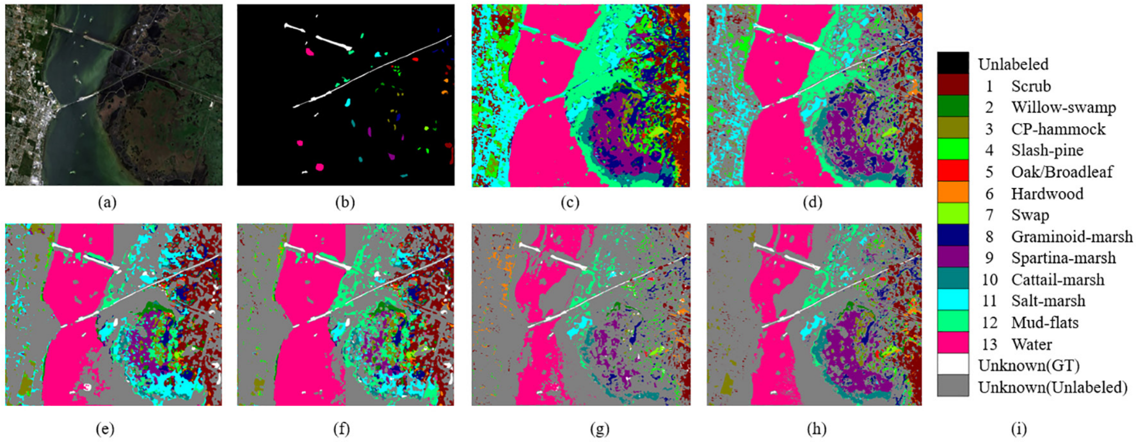

Figure 7. Classification map on the KSC data set. (a) False-color map; (b) reference map; (c) CSC-based DCNN_k; (d) Softmax*; (e) MDLO4W; (f) MDLO4W/C; (g) OpenMax; (h) SSLOSC; (i) legend. CSC = closed set classification; KSC = Kennedy Space Center.

the training set and train a standard $(K + 1)$-class DCNN model for open set classification of HSI.

It is worth pointing out that although OpenMax in the last round had higher scores ($F1_{unknown} = 0.90$, macro-F1= 0.86, $OA_{open} = 0.92$, and $OA_{known} = 0.86$) than in the first round ($F1_{unknown} = 0.84$, macro-F1= 0.82, $OA_{open} = 0.86$, and $OA_{known} = 0.80$), it was still inferior to our final DCNN_{K+1} model ($F1_{unknown} = 0.98$, macro-F1= 0.94, $OA_{open} = 0.98$, and $OA_{known} = 0.97$). This proves that the unlabeled data are useful if we exploit them wisely. OpenMax in the iterative process (except the first round) use the pseudo-labeled known classes in its training and therefore achieved higher performance. Our final DCNN_{K+1} model was trained based on the augmented training set, which included both the K-class samples with true labels and the refined pseudo-labeled unknown-class samples, and therefore achieved even higher performance.

Discussion

Existing HSI open set classification methods convert open set classification into a posterior probability calibration task based on extreme value theory and completely ignore the unlabeled data inherent in the HSI data set during model design. In this work, we aimed to design an open set classifier based on labeled and unlabeled data by using a semi-supervised learning method. The proposed method, called SSLOSC, was compared with the existing open set classification methods and a DCNN-based closed set classification method.

According to the experimental results presented in Figure 10, we can see that proposed open set deep model SSLOSC can automatically reject most unknown ($F1_{unknown} > 0.9$ under four open set scenarios) while maintaining high recognition accuracy on known classes ($OA_{known} > 0.9$). On the contrary, OpenMax tends toward inferior recognition accuracy on known classes (Figure 10d) and the Multitask Deep Learning methods (MDL4OW and MDL4OW/C) have inferior ability to reject the unknown class (Figure 10a). As a result, the proposed method got the highest scores in term of OA_{open} and macro-F1 under all open set scenarios, as shown in Figure 10b–c. This is because using semi-supervised learning, we make the unlabeled data join in the data preparation and model training. In the semi-supervised learning procedure, unknown samples with high confidence are selected from the inherent unlabeled data and mixed into the original labeled known samples, and therefore lead to a simple and effective OSC model. The corresponding cost is that the training procedure of our model is time-consuming, because training-set augmentation based on semi-supervised learning requires multi-round iteration. Luckily, our final OSC model used for testing and predicting is simple and

Table 9. Classification accuracy on KSC data set. The bold face is the 1st result, and the italic is the 2nd result.

Class	Closed	SoftMax*	MDL4OW	MDL4OW/C	OpenMax	SSLOSC
1	0.78	0.84	0.78	0.75	0.84	0.92
2	0.88	0.96	0.91	0.95	0.88	0.93
3	0.90	0.90	0.97	0.95	0.66	0.88
4	0.52	0.71	0.69	0.69	0.72	0.73
5	0.81	0.82	0.76	0.78	0.84	0.78
6	0.92	0.94	0.91	0.80	0.86	0.90
7	0.99	1.00	0.97	0.94	0.85	0.86
8	0.87	0.94	0.95	0.89	0.93	0.96
9	1.00	1.00	0.98	0.98	0.81	1.00
10	0.97	1.00	0.97	0.94	0.96	1.00
11	0.33	0.42	0.61	0.85	0.93	0.97
12	0.42	0.50	0.74	0.77	0.91	0.96
13	0.85	0.87	0.95	0.95	0.96	0.99
Unknown (novel)	0.00	0.50	0.76	0.82	*0.88*	**0.96**
Macro-F1	0.73	0.81	0.85	*0.86*	*0.86*	**0.92**
OA_{open}	0.53	0.68	0.81	0.84	*0.88*	**0.95**
OA_{known}	**0.98**	*0.97*	0.96	0.93	0.82	0.94
Stop round	—	—	—	—	—	3

KSC = Kennedy Space Center.

Table 10. Classification accuracy on PU data set. The bold face is the 1st result, and the italic is the 2nd result.

Class	Closed	SoftMax*	MDL4OW	MDL4OW/C	OpenMax	SSLOSC
1	0.90	0.91	0.97	0.97	0.98	0.98
2	1.00	1.00	1.00	0.98	0.99	1.00
3	0.99	0.99	0.98	0.96	0.98	0.99
4	0.96	0.97	0.98	0.98	0.99	0.99
5	0.85	0.87	0.90	0.85	0.99	1.00
6	0.62	0.63	0.69	0.68	0.83	0.82
7	0.92	0.95	0.99	0.99	0.99	0.99
8	0.96	0.96	0.90	0.97	0.99	0.98
9	0.97	0.98	0.94	0.94	0.98	0.99
Unknown (novel)	0.00	0.13	0.13	0.30	*0.61*	**0.62**
Macro-F1	0.82	0.84	0.85	0.86	**0.93**	**0.93**
OA_{open}	0.78	0.79	0.89	0.88	**0.94**	**0.94**
OA_{known}	**0.99**	**0.99**	**0.99**	0.96	0.94	*0.98*
Stop round	—	—	—	—	—	3

PU = Pavia University.

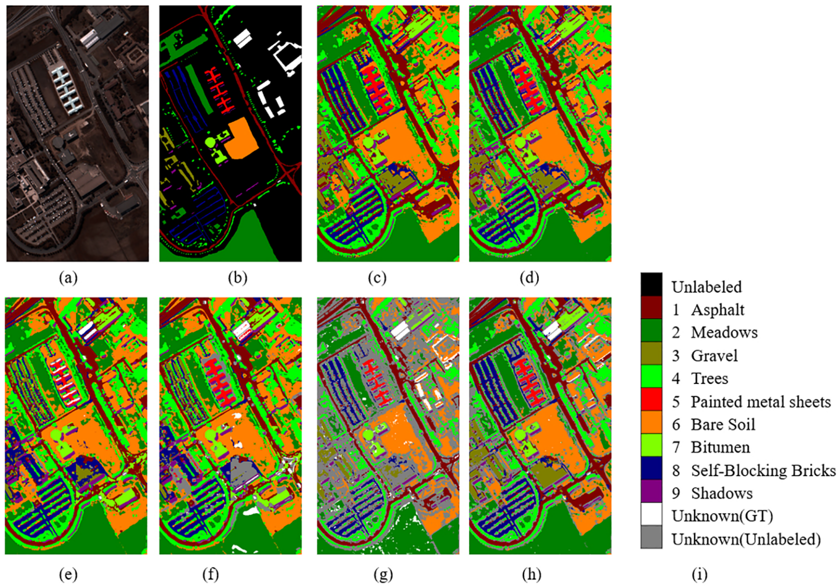

Figure 8. Classification map on the PU data set. (a) False-color map; (b) reference map; (c) CSC-based DCNN_k; (d) Softmax*; (e) MDLO4W; (f) MDLO4W/C; (g) OpenMax; (h) SSLOSC; (i) legend. CSC = closed set classification; PU = Pavia University.

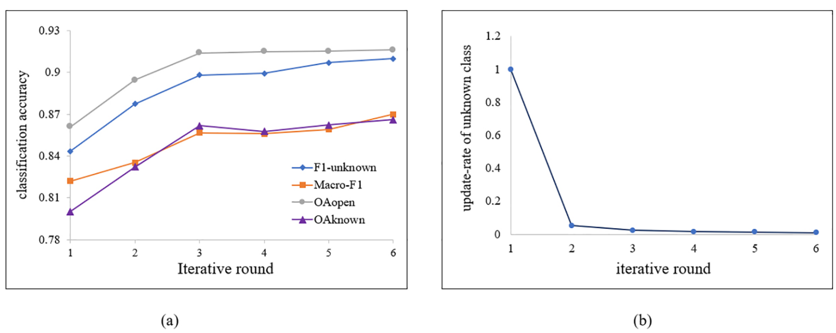

Figure 9. The intermediate result of semi-supervised iterative learning. (a) Classification accuracy of OpenMax; (b) update rate of the unknown class in the unlabeled data.

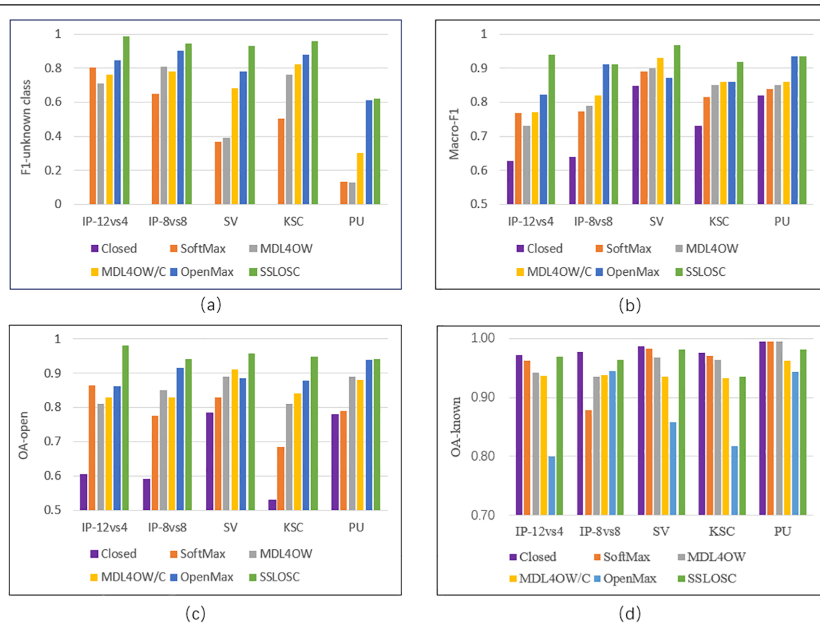

Figure 10. Bar graphs of evaluation indexes of different methods under five open set scenarios. (a) $F1_{unknown}$; (b) macro-F1; (c) overall accuracy of K known classes and unknown class; (d) overall accuracy of K known classes.

effective. This is meaningful and valuable, since we can predict HSIs using the model over and over once it is trained.

We also found that the performance of our proposed OSC method depends on the open set scenario, especially the $F1_{unknown}$ score, as shown in Figure 10a. For scenarios where the interclass spectral-spatial differences are significant, such as in the IP, SV, and KSC data sets, the proposed method can reject nearly all unknown classes (>90%) and classify known classes accurately (>95%). However, as the spectral-spatial similarity among different classes increases, the performance of the proposed method degrades to a certain degree—for example, the rejection ratio of unknown classes is only 0.62 on the PU data set. Therefore, there still remain some questions to be addressed, such as how the complexity of HSI data sets affects the OSC performance and how to better solve the OSC issues in complicated real-world applications where high interclass similarity, spectral mixing, and scattered distribution of samples occur frequently.

Conclusion

In this study, a semi-supervised learning method for HSI open set classification is devised by tapping the potential of unlabeled data. The proposed method uses a modified OpenMax and a semi-supervised iterative learning algorithm to find the pseudo-labeled unknown-class samples from the inherent unlabeled data. Then, based on the augmented training set—which consists of the original known-class samples and the pseudo-labeled unknown-class samples—a standard deep classification network, which can classify known classes while simultaneously rejecting the unknown class, is trained for HSI open set classification. The results reveal that the proposed method can achieve an approximately optimal trade-off between known-class classification accuracy and unknown-class rejection. It achieved the highest OA_{open} and macro-F1 scores among all methods studied. It also achieved the highest rejection ratio of unknown class and reasonable OA_{known} scores compared with a DCNN-based closed set method.

References

Bazi, Y. and F. Melgani. 2006. Toward an optimal SVM classification system for hyperspectral remote sensing images. *IEEE Transactions on Geoscience and Remote Sensing* 44(11):3374–3385.

Bendale, A. and T. E. Boult. 2016. Towards open set deep networks. Pages 1563–1572 in *Proceedings of the IEEE Conference on Computer Vision and Pattern Recognition (CVPR)*, held in Las Vegas, Nev., 26 June–1 July 2016. New York: IEEE.

Benediktsson, J. A., J. A. Palmason and J. R. Sveinsson. 2005. Classification of hyperspectral data from urban areas based on extended morphological profiles. *IEEE Transactions on Geoscience and Remote Sensing* 43(3):480–491.

Bovolo, F. 2009. A multilevel parcel-based approach to change detection in very high resolution multitemporal images. *IEEE Geoscience and Remote Sensing Letters* 6(1):33–37.

Camps-Valls, G., L. Gomez-Chova, J. Munoz-Mari, J. Vila-Frances and J. Calpe-Maravilla. 2006. Composite kernels for hyperspectral image classification. *IEEE Geoscience and Remote Sensing Letters* 3(1):93–97.

Chen, H., X. Li, J. Zhou and Y. Wang. 2022. TPPI: A novel network framework and model for efficient hyperspectral image classification. *Photogrammetric Engineering and Remote Sensing* 88(8):535-546.

Chen, Y., H. Jiang, C. Li, X. Jia and P. Ghamisi. 2016. Deep feature extraction and classification of hyperspectral images based on convolutional neural networks. *IEEE Transactions on Geoscience and Remote Sensing* 54(10):6232–6251.

Fauvel, M., J. A. Benediktsson, J. Chanussot and J. R. Sveinsson. 2008. Spectral and spatial classification of hyperspectral data using SVMs and morphological profiles. *IEEE Transactions on Geoscience and Remote Sensing* 46(11):3804–3814.

Ge, Z. Y., S. Demyanov, Z. Chen and R. Garnavi. 2017. Generative OpenMax for multi-class open set classification, in *British Machine Vision Conference*, held in London, UK, 4–7 September 2017. Edited by J. Editor. London: BMVA Press.

Guerra, R., L. Santos, S. López and R. Sarmiento. 2015. A new fast algorithm for linearly unmixing hyperspectral images. *IEEE Transactions on Geoscience and Remote Sensing* 53(12):6752–6765.

He, L., J. Li, C. Liu and S. Li. 2018. Recent advances on spectral-spatial hyperspectral image classification: An overview and new guidelines. *IEEE Transactions on Geoscience and Remote Sensing* 56(3):1579–1597.

Jain, L. P., W. J. Scheirer and T. E. Boult. 2014. Multi-class open set recognition using probability of inclusion. Pages 393–409 in *Computer Vision—ECCV 2014*, held in Zurich, Switzerland, 6–12 September 2014. Edited by J. Editor. Lecture Notes in Computer Science vol. 8691. Cham, Switzerland: Springer.

Jia, X. and J. A. Richards. 1994. Efficient maximum likelihood classification for imaging spectrometer data sets. *IEEE Transactions on Geoscience and Remote Sensing* 32(2):274–281.

Lanthier, Y., A. Bannari, D. Haboudane, J. R. Miller and N. Tremblay. 2008. Hyperspectral data segmentation and classification in precision agriculture: A multi-scale analysis. Pages 585–588 in *IGARSS 2008—2008 IEEE International Geoscience and Remote Sensing Symposium*, held in Boston, Mass., 7–11 July 2008. Edited by J. Editor. New York: IEEE.

Li, J., J. M. Bioucas-Dias and A. Plaza. 2010. Semisupervised hyperspectral image segmentation using multinomial logistic regression with active learning. *IEEE Transactions on Geoscience and Remote Sensing* 48(11):4085–4098.

Li, S., W. Song, L. Fang, Y. Chen, P. Ghamisi and J. A. Benediktsson. 2019. Deep learning for hyperspectral image classification: An overview. *IEEE Transactions on Geoscience and Remote Sensing* 57(9):6690–6709.

Li, W., G. Wu, F. Zhang and Q. Du. 2017. Hyperspectral image classification using deep pixel-pair features. *IEEE Transactions on Geoscience and Remote Sensing* 55(2):844–853.

Liu, S., Q. Shi and L. Zhang. 2021. Few-shot hyperspectral image classification with unknown classes using multitask deep learning. *IEEE Transactions on Geoscience and Remote Sensing* 59(6):5085–5102.

Liu, Y., Y. Tang, L. Zhang, L. Liu, M. Song, K. Gong, Y. Peng, J. Hou and T. Jiang. 2020. Hyperspectral open set classification with unknown classes rejection towards deep networks. *International Journal of Remote Sensing* 41(16):6355–6383.

Mercier, G. and F. Girard-Ardhuin. 2006. Partially supervised oil-slick detection by SAR imagery using kernel expansion. *IEEE Transactions on Geoscience and Remote Sensing* 44(10):2839–2846.

Murat Dundar, M. and D. Landgrebe. 2002. A model-based mixture-supervised classification approach in hyperspectral data analysis. *IEEE Transactions on Geoscience and Remote Sensing* 40(12):2692–2699.

Paoletti, M. E., J. M. Haut, R. Fernandez-Beltran, J. Plaza, A. J. Plaza and F. Pla. 2019. Deep pyramidal residual networks for spectral-spatial hyperspectral image classification. *IEEE Transactions on Geoscience and Remote Sensing* 57(2):740–754.

Scheirer, W. J., L. P. Jain and T. E. Boult. 2014. Probability models for open set recognition. *IEEE Transactions on Pattern Analysis and Machine Intelligence* 36(11):2317–2324.

Scheirer, W. J., A. Rocha, R. J. Micheals and T. E. Boult. 2011. Meta-recognition: The theory and practice of recognition score analysis. *IEEE Transactions on Pattern Analysis and Machine Intelligence* 33(8):1689–1695.

Scheirer, W. J., A. R. Rocha, A. Sapkota and T. E. Boult. 2013. Toward open set recognition. *IEEE Transactions on Pattern Analysis and Machine Intelligence* 35(7):1757–1772.

Song, W., S. Li, L. Fang and T. Lu. 2018. Hyperspectral image classification with deep feature fusion network. *IEEE Transactions on Geoscience and Remote Sensing* 56(6):3173–3184.

Yoshihashi, R., W. Shao, R. Kawakami, S. You, M. Iida and T. Naemura. 2019. Classification-reconstruction learning for open-set recognition. Pages 4016–4025 in *Proceedings of the IEEE/CVF Conference on Computer Vision and Pattern Recognition (CVPR)*, held in Long Beach, Calif., 15–20 June 2019. Edited by J. Editor. New York: IEEE.

Zhong, Z., J. Li, Z. Luo and M. Chapman. 2018. Spectral-spatial residual network for hyperspectral image classification: A 3-D deep learning framework. *IEEE Transactions on Geoscience and Remote Sensing* 56(2):847–858.

The Fractional Vegetation Cover (FVC) and Associated Driving Factors of Modeling in Mining Areas

Jun Li, Tianyu Guo, Chengye Zhang, Fei Yang, and Xiao Sang

Abstract

To determine the fractional vegetation cover (FVC) and associated driving factors of modeling in mining areas, six types of data were used as driving factors and three methods—multi-linear regression (MLR), geographically weighted regression (GWR), and geographically weighted artificial neural network (GWANN)—were adopted in the modeling. The experiments, conducted in Shengli mining areas located in Xilinhot city, China, show that the MLR model without consideration of spatial heterogeneity and spatial non-stationarity performs the worst and that the GWR model presents obvious location differences, since it predefines a linear relationship which is unable to describe FVC for some locations. The GWANN model, improving on these defects, is the most suitable model for the FVC driving process in mining areas; it outperforms the other two models, with root-mean-square error (RMSE) and mean absolute percentage error (MAPE) reaching 0.16 and 0.20. It has improvements of approximately 24% in RMSE and 33% in MAPE compared to the MLR model, and those values grow to 59% and 71% when compared with the GWR model.

Introduction

Vegetation is the comprehensive result of the long-term interaction of hydrology, soil, landforms, climate variability, and human activities, and its composition, distribution, and development are closely related with multiple driving factors (Yang *et al.* 2011; Zhu *et al.* 2012; Y. Li *et al.* 2015). It plays a pivotal role in energy exchange processes, climate change, and hydrological and biogeochemical cycles on Earth's surface. Fractional vegetation cover (FVC) refers to the ratio of the vertical projection of vegetation (stems, branches, and leaves) in the statistical area of land surface (Purevdorj *et al.* 1998; Gitelson *et al.* 2002), which is a critical parameter measuring the vegetation coverage status and reflecting the degree of horizontal coverage of vegetation on land surface (Zhang *et al.* 2018). As quantitative information, FVC is not only used as a sensitive indicator to evaluate land degradation and desertification (C. Zhao *et al.* 2005) but also regarded as a controlling factor for universal soil loss equation, revised universal soil loss equation, and numerical climate and hydro-ecological models (Sellers *et al.* 1996; Qi *et al.* 2000; G. Wang *et al.* 2002; Wu *et al.* 2012).

With the continuous development of remote sensing technology, monitoring spatiotemporal and phenological variations of vegetation in a certain area, as well as estimating vegetation productivity based on remote sensing, has now become the main trend in the FVC research field (Okin *et al.* 2013; J. Li *et al.* 2019a; J. Li *et al.* 2020). Remote sensing has the advantages of wide coverage, high continuity, and comprehensiveness, which can provide measurement of FVC with a new direction (Xing *et al.* 2009; J. Peng *et al.* 2012; H. Liu *et al.* 2021). Among the remote sensing FVC estimation methods, the use of a vegetation index (VI)—which includes the enhanced vegetation index, the difference vegetation index, the ratio vegetation index, and the normalized difference vegetation index (NDVI)—is the most common method (Barati *et al.* 2011). Research has illustrated that the NDVI is very sensitive to the spatial distribution characteristics and growth state of vegetation (Tucker 1979); can to a great extent eliminate interference from topography, instruments, atmosphere, and so on; and has a significant linear correlation with FVC (Yuan *et al.* 2013; Zhang *et al.* 2018)—which all makes the NDVI currently the most widely used VI (Chen *et al.* 2014; Imukova *et al.* 2015). Specifically, the dimidiate pixel model based on the NDVI is a practical method to effectively estimate FVC, because of its simple calculations, easy interpretation, insensitivity to the effects of image radiometric correction, and independence from actual FVC data modeling (Mu *et al.* 2012; W. Peng *et al.* 2016; Z. Li *et al.* 2017).

In mining areas, the exploitation and use of mineral resources have changed the material cycle and energy flow of ecosystems, always resulting in serious vegetation degradation and environmental pollution (Fu *et al.* 2017). Therefore, there has been increasing attention given to environmental protection and ecological restoration in mining areas. Research has shown that study of the temporospatial characteristics and variations of vegetation coverage based on remote sensing technology is an effective way to reveal changes of the ecological environment in mining areas. Erener (2011) applied remote sensing-based vegetation cover monitoring to a case study of the Seyitömer Lignite Enterprise in Kütahya, Tukey, and successfully assessed the reclamation practices. G. Wang and Qiu (2018) extracted the FVC in the Huainan mining area from MODIS NDVI time-series products, analyzed the evolution of vegetation cover in the research area during the period of 2005–2014, and provided scientific references for the ecological restoration of the mining area. Fang *et al.* (2020) analyzed the spatiotemporal variation of vegetation coverage in a large-scale mining area in eastern Inner Mongolia, China, using the NDVI time series from 1982 to 2015, and explored the influencing factors before and after mining. J. Li *et al.* (2019b) unitized the long-term FVC based on NDVI data from 1985 to 2015 to evaluate the impact of coal mining and other human activities on land ecology at the Baorixile coal mining area in the heart of Hulunbeier in China.

The FVC in mining areas is affected by multiple driving factors, including topography, climate, and human activity. The influence of topography, especially altitude, can cause regional differences in the level of FVC as well as in its variation trend and fluctuation range (T. Zhao *et al.* 2019; H. Liu *et al.* 2021; Pang *et al.* 2021). Changes in temperature and precipitation directly affect vegetative photosynthesis, respiration, and soil organic carbon decomposition, among others, and then affect the growth distribution and evolution patterns of vegetation, which makes climate factors the dominant ones affecting FVC (J.

Jun Li, Tianyu Guo, Chengye Zhang, Fei Yang, and Xiao Sang are with the State Key Laboratory of Coal Resources and Safe Mining, China University of Mining and Technology-Beijing, Beijing, China; and the College of Geoscience and Surveying Engineering, China University of Mining and Technology-Beijing, Beijing, China (yangfei@cumtb.edu.cn).

Contributed by Ribana Roscher, September 22, 2021 (sent for review December 1, 2021; reviewed by Barry N. Haack, Yuki Hamada, Xiaofang Wei, Lukas Drees).

Photogrammetric Engineering & Remote Sensing
Vol. 88, No. 10, October 2022, pp. 665–671.
0099-1112/22/665–671

doi: 10.14358/PERS.21-00070R3

Liu and Gao 2008; Jing *et al.* 2011; Guo *et al.* 2014; H. Wang *et al.* 2020). For example, Zhao *et al.* (2015) found that vegetation growth showed an insignificant increasing trend over the entire plateau during 1982–2011, and climate factors (i.e., precipitation and air temperature) were the two most important variables affecting vegetation growth. Q. Zhou *et al.* (2019) analyzed the effect of climate factors on FVC in the Beijing—Tianjin—Hebei region from 2001 to 2011 and showed that precipitation had the greatest effect on FVC in the core area. H. Liu *et al.* (2021) conducted research on the spatiotemporal evolution of FVC and its response to climate change based on MODIS data in the subtropical region in China, and concluded that the average annual minimum temperature was the main factor affecting dynamic variations of FVC. Human activities are another important factor affecting vegetation growth (Xin *et al.* 2008; Y. Liu *et al.* 2015). Y. Liu *et al.* (2015) explored the relationship between vegetation cover trends and the human footprint from 1982 to 2012 globally, and showed a positive correlation between human activity and the NDVI trend in Asia, Africa, and Europe. X. Zhou *et al.* (2018) distinguished the vegetation dynamics induced by anthropogenic factors from the effects of climate variability on the Mongolian Plateau during 1993–2012 based on the RESTREND method, and identified the divergent drivers of human-induced vegetation dynamics within different agricultural zones and socio-institutional periods. Meng *et al.* (2019) investigated the potential effects of human activities on vegetation changes over the Mongolian Plateau during the time of 1982–2015, and implied that anthropogenic factors may lead to cropland abandonment in favor of grassland restoration.

Based on the understanding of the correlation between vegetation cover and its associated driving factors in mining areas, Meng *et al.* (2019) and Fang *et al.* (2020) used a linear model containing temperature and precipitation to predict the NDVI from 1982 to 2015. Fu *et al.* (2017) established a linear model for the driving factors of interannual variation of NDVI using parameters including relative humidity, precipitation, and population engaged in secondary industry. However, there is a rather limited literature on FVC and associated driving factors for modeling in mining areas using different types of models, and there is also a lack of discussion on the availability of different models applied to the FVC driving process in mining areas. Therefore, we used modeling with FVC and associated driving factors in the Shengli mining area with three different methods: multiple linear regression, geographically weighted regression, and geographically weighted artificial neural network. Temperature, precipitation, topography, grazing, city, and mining were considered the driving factors. The most suitable model for the FVC driving process in the mining area was explored, and the characteristics of the influence of driving factors on FVC in different models were also analyzed. This type of model can provide large-scale FVC data for a mining area in the absence of field measurement and satellite observation, and dynamically predict FVC in a mining area based on existing data, providing important reference data for ecological restoration.

Materials and Methods

The Study Area

The Shengli mining area, located in Xilinhot city, Inner Mongolia Autonomous Region, China, was selected as the study area for this article, as shown in Figure 1. The study area lies at the north of the city and is approximately 5 km from the city center. It covers the zones between longitude 115.7°E and 116.3°E and latitude 43.8°N and 44.2°N, which is typical plateau hilly terrain from northeast to southwest (J. Li *et al.* 2021a), and has a total area of 342 km^2. It has a semi-arid continental monsoon climate with an average annual rainfall of 309 mm and average annual temperature of 1.5°C. The extreme maximum and minimum temperatures recorded in this area are 38.3°C, on 23 July 1955, and −42.4°C, on 15 January 1953. Rainfall is mainly concentrated in summer, with more than 71% of it between June and August. In addition, a variety of human activities exist around the study area, such as mining, grazing, and the development of cities and towns. Note that ecological restoration has been implemented since 2016 in the mining area.

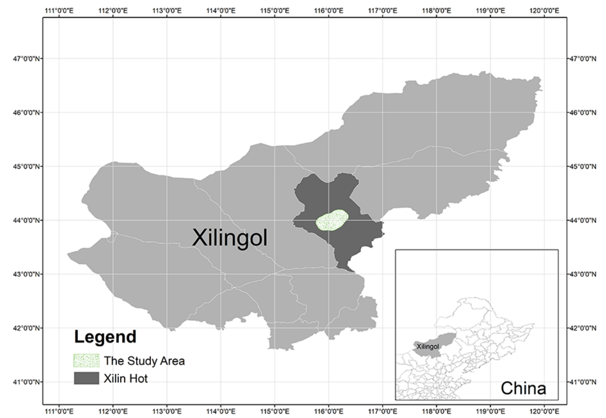

Figure 1. Map of the study area.

The Materials

Google Earth Engine was used to load the remote sensing data of the Landsat series satellites, including Landsat 5 TM, Landsat 7 ETM+, and Landsat 8 OLI. After atmospheric correction based on the Landsat Ecosystem Disturbance Adaptive Processing System algorithm (Schmidt *et al.* 2013), the NDVI of the study area from June to August was calculated from 1990 to 2020 using the following formula:

$$\mathrm{NDVI} = \frac{\rho_{\mathrm{NIR}} - \rho_{\mathrm{Red}}}{\rho_{\mathrm{NIR}} + \rho_{\mathrm{Red}}} \tag{1}$$

Where ρ_{NIR} and ρ_{Red} refer to the surface reflectance in the near-infrared and the red band, respectively. Then the dimidiate pixel model was applied to compute the FVC as follows (H. Liu *et al.* 2021):

$$\mathrm{FVC} = \frac{\mathrm{NDVI} - \mathrm{NDVI}_{\mathrm{soil}}}{\mathrm{NDVI}_{\mathrm{veg}} - \mathrm{NDVI}_{\mathrm{soil}}} \tag{2}$$

where NDVI denotes the NDVI value of the grid to be calculated, $\mathrm{NDVI}_{\mathrm{soil}}$ represents the NDVI value of the grid in the study area which is completely bare soil, and $\mathrm{NDVI}_{\mathrm{veg}}$ refers to the NDVI value of the grid with pure vegetation in the study area. Due to the influence of many factors, $\mathrm{NDVI}_{\mathrm{veg}}$ and $\mathrm{NDVI}_{\mathrm{soil}}$ are not theoretical fixed values of 0 and 1. To ensure the stability of these two values, the upper and lower thresholds of NDVI were calculated with 95% confidence intervals to approximate the values of $\mathrm{NDVI}_{\mathrm{veg}}$ and $\mathrm{NDVI}_{\mathrm{soil}}$ in the study area, respectively. Thus, the actual values of $\mathrm{NDVI}_{\mathrm{veg}}$ and $\mathrm{NDVI}_{\mathrm{soil}}$ are 0.7 and 0.08, respectively. This process for calculating FVC is consistent with the relevant literature to ensure the reliability of our data (J. Li *et al.* 2021b; Y. Liu *et al.* 2021).

The climate data were obtained from ERA5, which is the latest climate reanalysis produced by the European Centre for Medium-Range Weather Forecasts. It is available in the Climate Data Store covering the period from 1950 to the present. The monthly temperature and precipitation data on regular latitude/longitude grids at 0.1°×0.1° resolution from 1990 to 2020 were downloaded for this study. Afterward, the spatial distribution of temperature and precipitation each year was resampled by Kriging interpolation in ArcGIS software to be compatible with the NDVI data sets. The topography data were obtained from the Terra Advanced Spaceborne Thermal Emission and Reflection Radiometer Global Digital Elevation Model, which provides a global digital elevation model of land areas on Earth at a spatial resolution of 1 arcsec.

The grazing data comes from the statistical yearbook of Xilinhot city and its summer census of agriculture and animal husbandry, including data on the number of cattle, sheep, horses, and other livestock each year, with village and branch farms as statistical units. According to the grass-livestock balance policy of Xilinhot city, the number of cattle and horse is converted into the number of sheep. The total grazing intensity of a village is obtained by dividing the total number of sheep by the total area of the village, and then the total intensity value is averaged to each grid, and finally the grazing data of grids are achieved. For the city and mining data, the distance from each grid to the center of the city and the mining area are counted, respectively, and then used as the city data and mining data for the subsequent modeling.

The Different Models

Multi-linear regression is a statistical technique that is used to predict the outcome of a variable based on the values of two or more variables. The variable that we want to predict is known as the response variable, which corresponds to FVC in this article; the variables we use to predict the value of the response variable are known as explanatory variables, which are the temperature, precipitation, topography, grazing, city, and mining factors in this article. The goal of MLR is to model the linear relationship between the explanatory variables and response variable. The MLR formula used in this article is

$$\mathrm{FVC} = \beta_0 + \beta_1 T + \beta_2 P + \beta_3 \mathrm{Top} + \beta_4 G + \beta_5 M + \beta_6 C + \varepsilon \tag{3}$$

where FVC refers to the response variable; β_0 is a constant term denoting the y-intercept; T, P, Top, G, M, and C are the six explanatory variables of temperature, precipitation, topography, grazing, mining, and city factors; β_1, β_2, β_3, β_4, β_5, and β_6 are the regression coefficients of the model; and ε is the model's error term.

Geographically weighted regression was introduced to the geography community by Brunsdon *et al.* (1996) to study the potential for relationships in a regression model to vary in geographical space. It accounts for spatial autocorrelation of variables and adds a level of modeling sophistication by allowing the relationships between the response and explanatory variables to vary by locality. The innovation with GWR is using a subset of data proximate to the model calibration location in geographical space instead of variable space (Páez and Wheeler 2009). In GWR, a separate formula is constructed for every model calibration location in the data set, which incorporates the response and explanatory variables of locations falling within the bandwidth of each target location. The GWR formula for each calibration location is expressed as follows:

$$\mathrm{FVC}_i = \beta_0(u_i, v_i) + \beta_1(u_i, v_i)T_i + \beta_2(u_i, v_i)P_i + \beta_3(u_i, v_i)\mathrm{Top}_i + \beta_4(u_i, v_i)G_i + \beta_5(u_i, v_i)M_i + \beta_6(u_i, v_i)C_i + \varepsilon_i \tag{4}$$

where (u_i, v_i) denotes the coordinates of the ith location in the model. The other parameters are consistent with those in Equation 3. In this model, the Gaussian kernel function is selected to produce weights that monotonically decrease with distance, expressed as follows:

$$w_{ij} = \exp\left(-\frac{1}{2}\left(\frac{d_{ij}}{3}\right)^2\right) \tag{5}$$

where w_{ij} refers to the weight for observation j relative to observation i, which changes as a function of the distance d_{ij} and a kernel bandwidth parameter γ that controls the range and decay of spatial correlation.

To better describe the nonlinear relationship between variables, Hagenauer and Helbich (2022) proposed the geographically weighted artificial neural network (GWANN), which is a variant of an artificial neural network (ANN) that incorporates geographical weighting of connection weights. The architecture of the GWANN is identical to that of a basic ANN, except that each output neuron of the GWANN is assigned to a location in geographic space, as shown in Figure 2. Another difference between the GWANN and a basic ANN is that a geographic weighted error function is used instead of the basic quadratic error function to calculate an error signal. In this model, the geographically weighted error function is defined as follows:

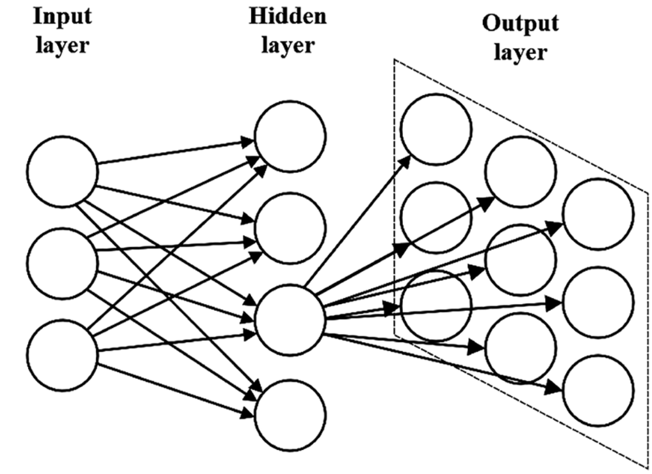

Figure 2. Geographically weighted artificial neural network with three layers.

$$E = \frac{1}{2}\sum_{i=1}^{n} v_i \left(t_i - o_i\right)^2 \tag{6}$$

where t_i is the target value, o_i is the output of output neuron i, v_i is the geographically weighted distance between the observation and the location of output neuron i, and n denotes the number of output neurons. Following the definition of the geographically weighted error function, the calculation of the error signal of back propagation is modified as follows:

$$\delta_j = \begin{cases} \phi'\left(\mathrm{net}_j\right) v_j \left(o_j - t_j\right) & \text{if } j \text{ is an output neuron} \\ \phi'\left(\mathrm{net}_j\right) \sum_k \delta_k w_{jk} & \text{otherwise} \end{cases} \tag{7}$$

where o_j is the output of neuron j, t_j is the target value of neuron j, w_{jk} is the connection weight between neurons j and k, δ_k is the error signal for neuron k, net_j is the network input to neuron j, ϕ' is the derivative of the activation function, and v_j is the geographically weighted distance between the observation and the location of output neuron j.

Discussion of the Model Performance

In this experiment, the FVC data and the multiple driving data from 1990 to 2015 were used to construct the three models (MLR, GWR, and GWANN). To assess their performance, the FVC values estimated by these three models were compared and discussed using the reference FVC values of 2016–2020 derived from Landsat. That is, the data from 1990 to 2015 were used for training the models and the data from 2016 to 2020 were selected for model testing. The two statistical quantities of root-mean-square error (RMSE) and mean absolute percentage error (MAPE) were chosen as criteria to perform the assessment, which can be described in the following equations:

$$\mathrm{RMSE} = \sqrt{\frac{1}{N}\sum_{i=1}^{N}\left(\mathrm{FVC}_i - \mathrm{FVC}_i^R\right)^2} \tag{8}$$

$$\mathrm{MAPE} = \frac{1}{N}\sum_{i=1}^{N}\left|\frac{\mathrm{FVC}_i^R - \mathrm{FVC}_i}{\mathrm{FVC}_i^R}\right| \times 100\% \tag{9}$$

where FVC_i and FVC_i^R are the FVC values from different models and the reference, respectively, and N refers to the number of the samples.

After the FVC estimates of each grid in the study area from 2016 to 2020 were achieved using the three models, the comparison was conducted with the reference FVC and scatter diagrams were drawn, as shown in Figure 3. The black dashed line is a 1:1 straight line, and the red straight line represents a linear-fitting straight line between the estimated and reference FVCs. It can be seen that the FVC estimated by the MLR model has significant difference from the reference FVC, with a slope of linear fitting of 0.06, showing that the MLR model performs worst in estimating FVC. The performance of the GWR model is clearly better than that of the MLR model, with a slope of 0.42 and more scatter points distributed near the 1:1 line. For the GWANN model, the distribution of scatter points and the fitting straight line show the best linear regression relationship among the three models. Specifically, the slope reaches 0.67 and the density of the scatter points distributed near the fitting line is higher than for the other two models. Note that the phenomenon of FVC estimates greater than 1 has occurred in the first two models, especially the MLR model, which is inconsistent with the actual situation, where the FVC value is less than 1. The GWANN model effectively improves this phenomenon.

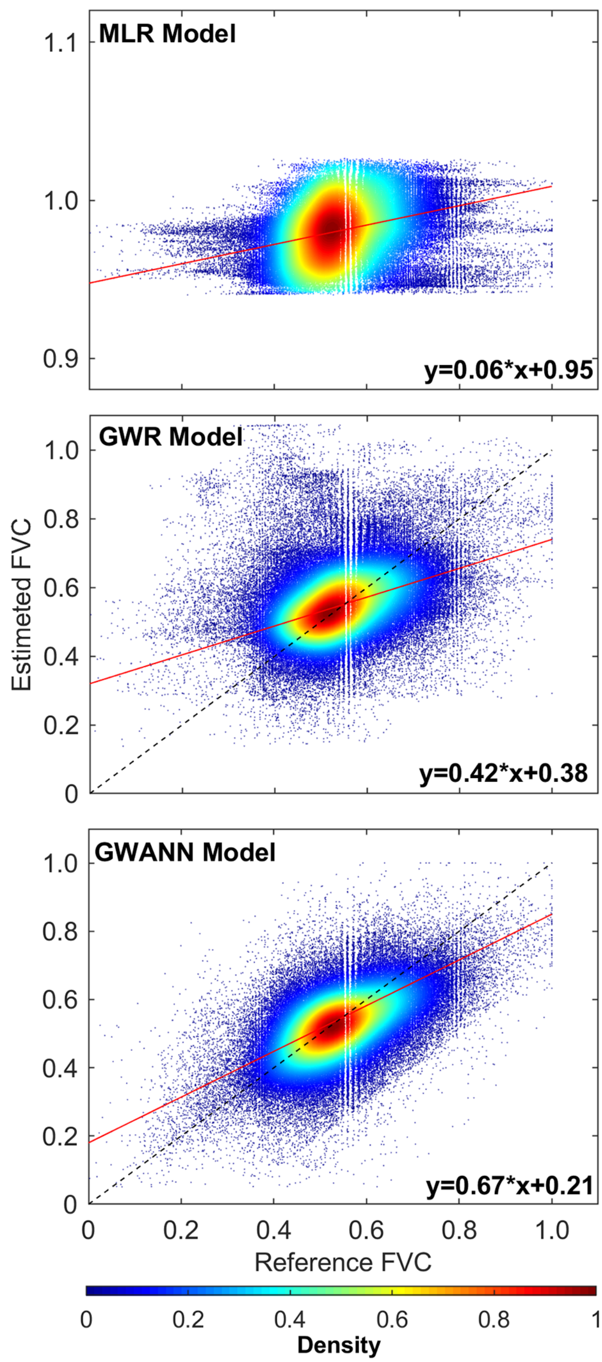

Figure 3. Scatterplots of the estimated fractional vegetation cover (FVC) against the reference FVC for the three models

Further, the histograms of FVC residuals—namely the values that result from subtracting the reference FVC from the model-estimated FVC—for each grid in the study area from 2016 to 2020 are shown in Figure 4. The residual histograms of the three models are all normally distributed; the GWR and GWANN models especially appear close to a standard normal distribution, with an approximate expectation of 0. The MLR model performs poorly, since the residuals are almost all positive and nearly half are greater than 0.5. The GWANN model performs better than the GWR model, with more residuals concentrated around zero, and the maximum and minimum values are around 0.5 and −0.5, whereas the GWR model has more residuals less than −0.5 or greater than 0.5. As for the absolute residuals less than 0.1, the GWANN model has a relatively larger percentage that the GWR model: 45.5% compared with 43.3%. When the absolute value is set to less than 0.3, these percentages reach 88.7% and 86.1%, respectively. In addition, the statistics of FVC residuals, including RMSE and MAPE, are counted for the three models (Table 1). This illustrates again that the MLR model has the worst statistical values, with RMSE and MAPE reaching 0.39 and 0.70. The two statistics for the GWR and GWANN models are, respectively, 0.21/0.30 and 0.16/0.20, achieving improvements over the MLR model of 46%/57% and 59%/71%.

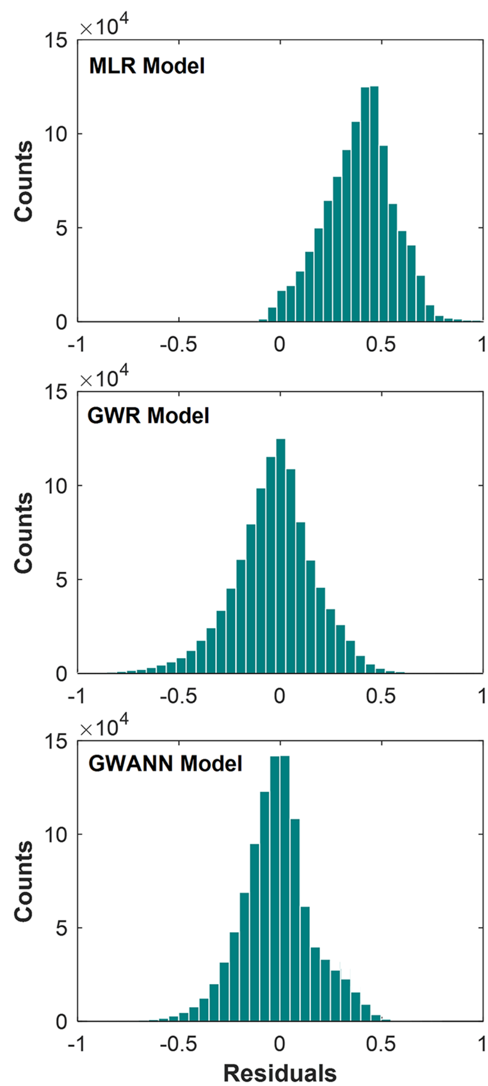

Figure 4. Histograms of the fractional vegetation cover residuals for the three models.

To analyze the performance of the three FVC models in different years, their RMSE and MAPE from 2016 to 2020 are plotted in Figure 5, in which different colors refer to different models and the dotted lines represent the average values of the five-year statistics. The GWANN model (red) performs best in every year in terms of RMSE and MAPE, followed by the GWR and MLR models. The MLR model shows great differences in different years. The largest and smallest RMSE and MAPE for the MLR model appear in 2020 and 2018, respectively, and their differences reach 0.16 and 40%. For the GWR and GWANN models, the difference between the five-year statistical value and the average is small, and the maximum differences are 0.07/11% and 0.07/8%. This illustrates that the GWANN model has the best stability in estimating FVC.

Table 1. Statistics of the fractional vegetation cover residuals for the three models.

Model	RMSE	MAPE
MLR	0.39	0.70
GWR	0.21	0.30
GWANN	0.16	0.20

GWANN = geographically weighted artificial neural network; GWR = geographically weighted regression; MAPE = mean absolute percentage error; MLR = multi-linear regression; RMSE = root-mean-square error.

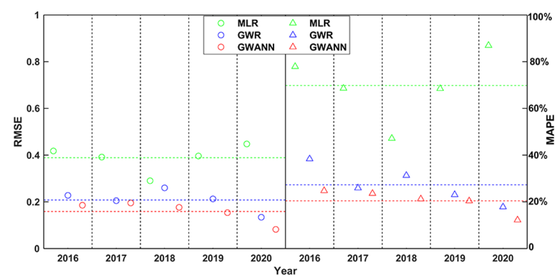

Figure 5. RMSE and MAPE from 2016 to 2020 for the three models. Green = MLR model; blue = GWR model; red = GWANN model. Circles = RMSE; triangles = MAPE; dotted lines = five-year average values. GWANN = geographically weighted artificial neural network; GWR = geographically weighted regression; MAPE = mean absolute percentage error; MLR = multi-linear regression; RMSE = root-mean-square error.

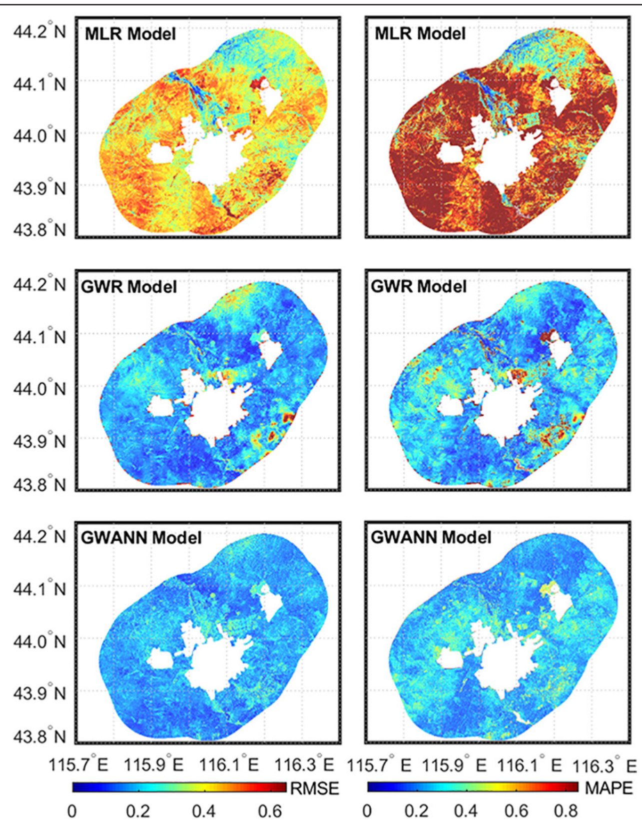

Figure 6. Distributions of root-mean-square error (RMSE) and mean absolute percentage error (MAPE) from 2016 to 2020 for the three models.

To analyze the accuracy of the three models at different locations in the study area, the FVC residuals from 2016 to 2020 in each grid were counted. Figure 6 illustrates the distributions of RMSE and MAPE for the differences between the reference FVC and model-derived FVCs. From the top panel, we can see the poor performance of the MLR model in almost all locations, with the RMSE and MAPE showing large diversity in different grids. It illustrates that the MLR model can hardly describe accurate FVC in a certain area. Compared with the MLR model, the FVC estimated by the GWR model is much closer to the reference FVC in most grids, as shown by the smaller RMSE and MAPE in the middle panel. However, large RMSE and MAPE still appear in some grids, indicating differences in model accuracy by location. These grids with high errors are often around mining areas and towns, where there are more types of human activities and the driving factors become more complex. This makes it difficult for the GWR model with linear modeling to accurately describe FVC at those locations, which are exactly the ones we care about most. The GWANN model achieves the best accuracy within the study area, and the location differences in model accuracy, including RMSE and MAPE, are effectively improved.

To further show the distribution of RMSE, the empirical distribution functions of RMSE in the three models are depicted in Figure 7, indicating the percentage of each range of the FVC RMSE. Compared with the results of the MLR model (represented by the green curve), the blue and red curves are obviously closer to the position of 0 and cover a relatively smaller range of the horizontal axis, showing a better distribution of results for the GWR and GWANN models. The percentage of RMSE smaller than 0.2 is 2% for GWR model; this becomes 68% and 73% for the GWR and GWANN models, respectively. When the range is set to less than 0.3, the percentages increase to, respectively, 10%, 92%, and 96%. These results show the advantages of the GWANN model compared to the other two models.

Conclusions

In mining areas, the FVC is related to multiple driving factors, including meteorological, topographic, and human activity parameters. For

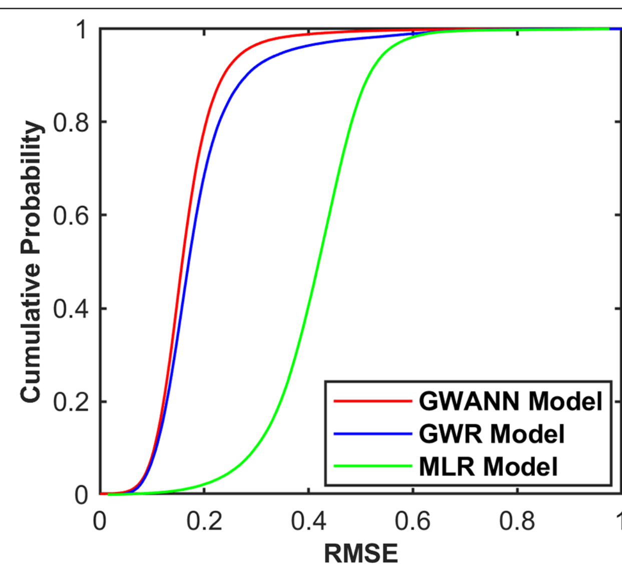

Figure 7. The empirical distribution function of the root-mean-square error in different models.

modeling FVC and associated driving factors, we selected temperature data, precipitation, topography, grazing, mining, and city data as the driving factors, and used three methods in the modeling: MLR, GWR, and GWANN.

In this experiment, we developed the three models for the Shengli mining area in Xilinhot city, China. Numerical results—namely, RMSE and MAPE—showed that the GWANN model had better performance in FVC estimation than the MLR and GWR models. Specifically, the GWANN model achieved an RMSE of 0.16 for all FVC residuals, which is 0.23 and 0.05 smaller than the MLR and GWR models, respectively—improvements of approximately 59% and 24%. The FVC scatter diagrams showed that the GWANN model has the best slope, of 0.67, and the density of the scatter points distributed near the fitting line is higher than for the other two models. In the analysis of the performance of the three models in different years, the MLR model showed great differences in different years, and the phenomenon can be effectively improved by the GWR and GWANN models. In the analysis of the performance for the three models in different locations, the GWANN model outperformed the other two model, with the percentages of RMSE smaller than 0.2 and 0.3 reaching to 73% and 96%, respectively, and no obvious differences appear in different grids.

The experiment illustrates that the MLR model, which does not consider spatial heterogeneity or the characteristics of the driving factors changing with geographic distance, can hardly estimate accurate FVC values. The GWR model improves on these problems and achieved more accurate FVC estimates. But location differences in model accuracy still appear, since the linear relationship between FVC and the driving factors is still predefined. The GWANN model used an artificial neural network that incorporates geographical weighting of connection weights, which effectively solved the defects and improved the accuracy compared to the other two models. The GWANN model is regarded as the most suitable model for the FVC driving process in the mining area. Therefore, we think this type of model, especially the GWANN model, can provide large-scale FVC data for mining areas in the absence of field measurement and satellite observations, and can dynamically estimate and predict FVC in mining areas based on existing data, providing important reference data for ecological restoration in mining areas. In follow-up research, the driving factors should be further explored to improve their accuracy.

Acknowledgments

This study was supported by the Open Fund of State Key Laboratory of Coal Resources and Safe Mining (SKLCRSM21KFA08), the China Postdoctoral Science Foundation (2021M703510), the Fundamental Research Funds for the Central Universities (2021XJDC01, 2022JCCXDC04), the Open Fund of State Key Laboratory of Water Resource Protection and Utilization in Coal Mining (GJNY-21-41-18), the National Natural Science Foundation of China (41901291), and the Yueqi Young Scholars Program of China University of Mining and Technology at Beijing. We thank all the anonymous reviewers for their valuable, constructive, and prompt comments.

The data sets generated and analyzed during the current study are available from the corresponding author on reasonable request.

References

Barati, S., B. Rayegani, M. Saati, A. Sharifi and M. Nasri. 2011. Comparison the accuracies of different spectral indices for estimation of vegetation cover fraction in sparse vegetated areas. *The Egyptian Journal of Remote Sensing and Space Science* 14:49–56.

Brunsdon, C., A. S. Fotheringham and M. E. Charlton. 1996. Geographically weighted regression: A method for exploring spatial nonstationarity. *Geographical Analysis* 28(4):281–298.

Chen, Y., Y. Luo, W. Mo, J. Mo, Y. Huang and M. Ding. 2014. Differences between MODIS NDVI and MODIS EVI in response to climatic factors. *Journal of Natural Resources* 29:1802–1812.

Erener, A. 2011. Remote sensing of vegetation health for reclaimed areas of Seyitömer open cast coal mine. *International Journal of Coal Geology* 86(1):20–26.

Fang, A., J. Dong, Z. Cao, F. Zhang and Y. Li. 2020. Tempo-spatial variation of vegetation coverage and influencing factors of large-scale mining areas in eastern Inner Mongolia, China. *International Journal of Environmental Research and Public Health* 17:47.

Fu, X., M. Ma, P. Jiang and Y. Quan. 2017. Spatiotemporal vegetation dynamics and their influence factors at a large coal-fired power plant in Xilinhot, Inner Mongolia. *International Journal of Sustainable Development & World Ecology* 24:433–438. https://doi.org/10.1080/13504509.2016.1273265.

Gitelson, A. A., Y. J. Kaufman, R. Stark and D. Rundquist. 2002. Novel algorithms for remote estimation of vegetation fraction. *Remote Sensing of Environment* 80(1):76–87.

Guo, L., S. Wu, D. Zhao, Y. Yin, G. Leng and Q. Zhang. 2014. NDVI-based vegetation change in Inner Mongolia from 1982 to 2006 and its relationship to climate at the biome scale. *Advances in Meteorology* 2014:692068.

Hagenauer, J. and M. Helbich. 2022. A geographically weighted artificial neural network. *International Journal of Geographical Information Science* 36:215–235.

Imukova, K., J. Ingwersen and T. Streck. 2015. Determining the spatial and temporal dynamics of the green vegetation fraction of croplands using high-resolution RapidEye satellite images. *Agricultural and Forest Meteorology* 206:113–123.

Jing, X., W.-Q. Yao, J.-H. Wang and X.-Y. Song. 2011. A study on the relationship between dynamic change of vegetation coverage and precipitation in Beijing's mountainous areas during the last 20 years. *Mathematical and Computer Modelling* 54:1079–1085.

Li, J., L. Cui, X. Yan, Z. Yang, J. Dong and X. Deng. 2019b. Comparative analysis of long-term trends on fraction of vegetation coverage in grassland mining area. *Bulletin of Surveying and Mapping* 0(8):130–134.

Li, J., Y. Pei, S. Zhao, R. Xiao, X. Sang and C. Zhang. 2020. A review of remote sensing for environmental monitoring in China. *Remote Sensing* 12(7):1130.

Li, J., X. Sang, C. Zhang, W. Zhao, X. Liu, H. Wang, J. Wang, J. Li and Y. Yang. 2021a. Analysis of soil moisture content changes in resource-based cities over a long time series: A case study of Xilinhot city. *Bulleting of Surveying and Mapping* 0(7):17–22, 38.

Li, J., X. Yan, X. Yan, W. Guo, K. Wang and J. Qiao. 2021b. Temporal and spatial variation characteristic of vegetation coverage in the Yellow River Basin based on GEE cloud platform. *Journal of the China Coal Society* 46(5):1439–1450.

Li, J., J. Zhang, C. Liu and X. Yang. 2019a. Spatiotemporal variation of vegetation coverage in recent 16 years in the border region of China, Laos, and Myanmar based on MODIS-NDVI. *Scientia Silvae Sinica* 55:9–18.

Li, Y., H. Wang and X. B. Li. 2015. Fractional vegetation cover estimation based on an improved selective endmember spectral mixture model. *PLoS One* 10(4):e0124608. https://doi.org/10.1371/journal.pone.0124608.

Li, Z., R. Sun, J. Zhang and C. Zhang. 2017. Temporal-spatial analysis of vegetation coverage dynamics in Beijing-Tianjin-Hebei metropolitan regions. *Acta Ecologica Sinica* 37:7418–7426.

Liu, H., X. Li, F. Mao, M. Zhang, D. Zhu, S. He, Z. Huang and H. Du. 2021. Spatiotemporal evolution of fractional vegetation cover and its response to climate change based on MODIS data in the subtropical region of China. *Remote Sensing* 13:913.

Liu, J. and J. Gao. 2008. Effects of climate and land use change on the changes of vegetation coverage in farming-pastoral ecotone of Northern China. *Chinese Journal of Applied Ecology* 19:2016–2022.

Liu, Y., Y. Li, S. Li and S. Motesharrei. 2015. Spatial and temporal patterns of global NDVI trends: Correlations with climate and human factors. *Remote Sensing* 7:13233–13250.

Liu, Y., P. Zeng, R. Zhang, F. Sun and Y. Che. 2021. Vegetation coverage change of the demonstration area of ecologically friendly development in the Yangtze River Delta, China based on GEE and BRT during 1984-2019. *The Journal of Applied Ecology* 32:1033–1044.

Meng, M., N. Huang, M. Wu, J. Pei, J. Wang and Z. Niu. 2019. Vegetation change in response to climate factors and human activities on the Mongolian Plateau. *PeerJ* 7:e7735.

Mu, S., J. Li, Y. Chen, C. Gang, W. Zhou and W. Ju. 2012. Spatial differences of variations of vegetation coverage in Inner Mongolia during 2001–2010. *Acta Geographica Sinica* 67:1255–1268.

Okin, G. S., K. D. Clarke and M. M. Lewis. 2013. Comparison of methods for estimation of absolute vegetation and soil fractional cover using MODIS normalized BRDF-adjusted reflectance data. *Remote Sensing of Environment* 130:266–279.

Páez, A., D. Wheeler. 2009. Geographically Weighted Regression. International Encyclopedia of Human Geography. Oxford: Elsevier, 407-414.

Pang, G., L. Shan, Q. Yang and X. Tu. 2021. Spatial and temporal variation characteristics of vegetation coverage and its influencing factor in different landforms of Shaanxi province. *Journal of Yangtze River Science Research Institute* 38: 51-58.

Peng, J., Y. Liu, H. Shen, Y. Han and Y. Pan. 2012. Vegetation coverage change and associated driving forces in mountain areas of Northwestern Yunnan, China using RS and GIS. *Environmental Monitoring and Assessment* 184(8):4787–4798.

Peng, W., G. Wang, J. Zhou, X. Xu, H. Luo, J. Zhao and C. Yang. 2016. Dynamic monitoring of fractional vegetation cover along Minjiang River from Wenchuan County to Dujiangyan City using multi-temporal Landsat 5 and 8 images. *Acta Ecologica Sinica* 36:1975–1988.

Purevdorj, T. S., R. Tateishi, T. Ishiyama and Y. Honda. 1998. Relationships between percent vegetation cover and vegetation indices. *International Journal of Remote Sensing* 19(18):3519–3535.

Qi, J., R. C. Marsett, M. S. Moran, D. C. Goodrich, P. Heilman, Y. H. Kerr, G. Dedieu, A. Chehbouni and X. X. Zhang. 2000. Spatial and temporal dynamics of vegetation in the San Pedro River basin area. *Agricultural and Forest Meteorology* 105(1–3):55–68.

Schmidt, G., C. Jenkerson, J. Masek, E. Vermote and F. Gao. 2013. *Landsat Ecosystem Disturbance Adaptive Processing System (LEDAPS) Algorithm Description*. Open-File Report 2013–1057. Reston, Va.: US Geological Survey.

Sellers, P. J., C. J. Tucker, G. J. Collatz, S. O. Los, C. O. Justice, D. A. Dazlich and D. A. Randall. 1996. A revised land surface parameterization (SiB2) for atmospheric GCMs. Part II: The generation of global fields of terrestrial biophysical parameters from satellite data. *Journal of Climate* 9(4):706–737.

Tucker, C. J. 1979. Red and photographic infrared linear combinations for monitoring vegetation. *Remote Sensing of Environment* 8:127–150.

Wang, G. and K. Qiu. 2018. Dynamic monitoring of vegetation coverage in Huainan mining area based on MODIS NDVI. *Bulletin of Surveying and Mapping* 0(6):34–40.

Wang, G., S. Wente, G. Z. Gertner and A. Anderson. 2002. Improvement in mapping vegetation cover factor for the universal soil loss equation by geostatistical methods with Landsat Thematic Mapper images. *International Journal of Remote Sensing* 23(18):3649–3667.

Wang, H., F. Yao, H. Zhu and Y. Zhao. 2020. Spatiotemporal variation of vegetation coverage and its response to climate factors and human activities in arid and semi-arid areas: Case study of the Otindag Sandy Land in China. *Sustainability* 12:5214.

Wu, C.-G., S. Li, H.-D Ren, X.-H. Yao and Z.-J. Huang. 2012. Quantitative estimation of vegetation cover and management factor in USLE and RUSLE models by using remote sensing data: A review. *Chinese Journal of Applied Ecology* 23(6):1728–1732.

Zhao, X., H. Hu, H. Shen, D. Zhou, L. Zhou, R. B. Myneni and J. Fang. 2015. Satellite-indicated long-term vegetation changes and their drivers on the Mongolian Plateau. *Landscape Ecology* 30:1599–1611.

Xin, Z. B., J. X. Xu and W. Zheng. 2008. Spatiotemporal variations of vegetation cover on the Chinese Loess Plateau (1981–2006): Impacts of climate changes and human activities. *Science in China Series D: Earth Sciences* 51:67–78.

Xing, Z.-R., Y.-G. Feng, G.-J. Yang, P. Wang and W.-J. Huang. 2009. Method of estimating vegetation coverage based on remote sensing. *Remote Sensing Technology and Application* 24(6):849–854.

Yang, Z., J. Gao, C. Zhou, P. Shi, L. Zhao, W. Shen and H. Ouyang. 2011. Spatio-temporal changes of NDVI and its relation with climatic variables in the source regions of the Yangtze and Yellow rivers. *Journal of Geographical Sciences* 21(6):979–993.

Yuan, L., W. Jiang, W. Shen, Y. Liu, W. Wang, L. Tao, H. Zheng and X. Liu. 2013. The spatio-temporal variations of vegetation cover in the Yellow River Basin from 2000 to 2010. *Acta Ecologica Sinica* 33:7798–7806.

Zhang, X., Y. Zhang, D. Niu, W. Zhang, Z. Li, Z. Li and X. Guo. 2018. Spatial-temporal dynamics of upland meadow coverage on Wugong Mountain based on TM NDVI. *Acta Ecologica Sinica* 38:2414–2424.

Zhao, C.-X., D.-W. Zheng and W.-Q. He. 2005. Vegetation cover changes over time and its effects on resistance to wind erosion. *Acta Phytoecologica Sinica* 29(1):68–73.

Zhao, T., H. Bai, C. Deng, Q. Meng, S. Guo and G. Qi. 2019. Topographic differentiation effect on vegetation cover in the Qinling Mountains from 2000 to 2016. *Acta Ecologica Sinica* 39:4499–4509.

Zhou, Q., X. Zhao, D. Wu, R. Tang, X. Du, H. Wang, J. Zhao, P. Xu and Y. Peng. 2019. Impact of urbanization and climate on vegetation coverage in the Beijing–Tianjin–Hebei region of China. *Remote Sensing* 11:2452.

Zhou, X., Y. Yamaguchi and S. Arjasakusuma. 2018. Distinguishing the vegetation dynamics induced by anthropogenic factors using vegetation optical depth and AVHRR NDVI: A cross-border study on the Mongolian Plateau. *Science of the Total Environment* 616–617:730–743.

Zhu, W., S. Jia, A. Lü and T. Yan. 2012. Analyzing and modeling the coverage of vegetation in the Qaidam Basin of China: The role of spatial autocorrelation. *Journal of Geographical Sciences* 22(2):346–358.

SUSTAININGMEMBERS

ACI USA Inc.
Weston, Florida
https://acicorporation.com/
Member Since: 2/2018

Aerial Services, Inc.
Cedar Falls, Iowa
www.AerialServicesInc.com
Member Since: 5/2001

Airworks Solutions Inc.
Boston, Massachusetts
Member Since: 3/2022

Applanix
Richmond Hill, Ontario, Canada
http://www.applanix.com
Member Since: 7/1997

Ayres Associates
Madison, Wisconsin
www.AyresAssociates.com
Member Since: 1/1953

CT Consultants
Mentor, Ohio
Member Since: 3/2022

Dewberry
Fairfax, Virginia
www.dewberry.com
Member Since: 1/1985

Esri
Redlands, California
www.esri.com
Member Since: 1/1987

GeoCue Group
Madison, Alabama
http://www.geocue.com
Member Since: 10/2003

Geographic Imperatives LLC
Centennial, Colorado
Member Since: 12/2020

GeoWing Mapping, Inc.
Richmond, California
www.geowingmapping.com
Member Since: 12/2016

Halff Associates, Inc.
Richardson, Texas
www.halff.com
Member Since: 8/2021

Keystone Aerial Surveys, Inc.
Philadelphia, Pennsylvania
www.kasurveys.com
Member Since: 1/1985

Kucera International
Willoughby, Ohio
www.kucerainternational.com
Member Since: 1/1992

L3Harris Technologies
Broomfield, Colorado
www.l3harris.com
Member Since: 6/2008

Merrick & Company
Greenwood Village, Colorado
www.merrick.com/gis
Member Since: 4/1995

Nearmap
South Jordan, Utah
www.nearmap.com
Member Since: 6/2023

NV5 Geospatial
Sheboygan Falls, Wisconsin
www.quantumspatial.com
Member Since: 1/1974

Pickett and Associates, Inc.
Bartow, Florida
www.pickettusa.com
Member Since: 4/2007

Riegl USA, Inc.
Orlando, Florida
www.rieglusa.com
Member Since: 11/2004

Robinson Aerial Surveys, Inc.(RAS)
Hackettstown, New Jersey
www.robinsonaerial.com
Member Since: 1/1954

Sanborn Map Company
Colorado Springs, Colorado
www.sanborn.com
Member Since: 10/1984

Surdex Corporation
Chesterfield, Missouri
www.surdex.com
Member Since: 12/2011

Surveying And Mapping, LLC (SAM)
Austin, Texas
www.sam.biz
Member Since: 12/2005

T3 Global Strategies, Inc.
Bridgeville, Pennsylvania
https://t3gs.com/
Member Since: 6/2020

Terra Remote Sensing (USA) Inc.
Bellevue, Washington
www.terraremote.com
Member Since: 11/2016

Towill, Inc.
San Francisco, California
www.towill.com
Member Since: 1/1952

Woolpert LLP
Dayton, Ohio
www.woolpert.com
Member Since: 1/1985

SUSTAININGMEMBER**BENEFITS**

Membership

- ✓ Provides a means for dissemination of new information
- ✓ Encourages an exchange of ideas and communication
- ✓ Offers prime exposure for companies

Benefits of an ASPRS Membership

- Complimentary and discounted Employee Membership*
- E-mail blast to full ASPRS membership*
- Professional Certification Application fee discount for any employee
- Member price for ASPRS publications
- Discount on group registration to ASPRS virtual conferences
- Sustaining Member company listing in ASPRS directory/website
- Hot link to company website from Sustaining Member company listing page on ASPRS website
- Press Release Priority Listing in *PE&RS* Industry News
- Priority publishing of Highlight Articles in *PE&RS* plus, 20% discount off cover fee
- Discount on *PE&RS* advertising
- Exhibit discounts at ASPRS sponsored conferences (exception ASPRS/ILMF)
- Free training webinar registrations per year*
- Discount on additional training webinar registrations for employees
- Discount for each new SMC member brought on board (Discount for first year only)

*quantity depends on membership level